To the Graduate Council:

I am submitting herewith a thesis written by Nikhilesh Chawla entitled "Effect of Fiber Fabric Orientation on the Mechanical Behavior of Continuous Fiber Ceramic Composites." I have examined the final copy of this thesis for form and content and recommend that it be accepted in partial fulfillment of the requirements for the degree of Master of Science, with a major in Metallurgical Engineering.

Peter K. Liaw 10-17-94

Prof. Peter K. Liaw, Major Professor

We have read this thesis
and recommend its acceptance:

Thomas T. Meek

Accepted for the Council:

Associate Vice Chancellor
and Dean of The Graduate School

STATEMENT OF PERMISSION TO USE

In presenting this thesis in partial fulfillment of the requirements for a Master's degree at the University of Tennessee, Knoxville, I agree that the Library shall make it available to borrowers under the rules of the Library. Brief quotations from this thesis are allowable without special permission, provided that accurate acknowledgment of the source is made.

Permission for extensive quotation from or reproduction of this thesis may be granted by my major professor, or in his absence, by the Head of Interlibrary Services when, in the opinion of either, the proposed use of the material is for scholarly purposes. Any copying or use of the material in this thesis for financial gain shall not be allowed without my written permission.

Signature [signature]

Date 10/31/94

Effect of Fiber Fabric Orientation on the Mechanical Behavior of Continuous Fiber Ceramic Composites

A Thesis
Presented for the
Master of Science
Degree
The University of Tennessee, Knoxville

Nikhilesh Chawla

December 1994

ACKNOWLEDGMENTS

I am grateful to my advisor at the University of Tennessee-Knoxville (UTK), Prof. P.K. Liaw, for his guidance and for giving me the opportunity to work in the area of ceramic composites. Thanks are due to Dr. E. Lara-Curzio of the Mechanical Properties User Center at the High Temperature Materials Laboratory (HTML) at Oak Ridge National Lab, for stimulating discussions and continued guidance. His insistence on perfection substantially enhanced the quality of this work. This work could not have been completed without the help of Prof. K.K. Chawla of New Mexico Tech who, in addition to his role as my father, was always available for guidance, comfort, and always a refreshing point of view on a variety of subject matters. Comments from members of my thesis committee, Dr. T.T. Meek and Dr. N. Yu, were invaluable.

I would also acknowledge the help of numerous people at HTML: R.A. Lowden, Dr. M.K. Ferber, Dr. H.T. Lin, D.W. Coffey, W.M. Matlin, S. Shanmugham, F. Rebillat, S. Wong, and Dr. P.F. Becher. At UTK, my friends and colleagues were very supportive: T. Newport, N. Miriyala, J.A. Cook, and S.M. Joslin. S. Jain, of Structural Research and Analysis Corporation (SRAC), was very helpful in answering finite element modeling related questions.

The support and love of my parents and sister carried me through this work. Other friends who kept me sane through this work, primarily through e-mail were: P.Wei, C.L. Tremper, J. Ambriz, A. Lucero, J. Tang, and M. Hagen.

This research was sponsored jointly by the U.S. Department of Energy, Assistant Secretary for Energy Efficiency and Renewable Energy, Office of Transportation Technologies, as part of the HTML User Program, Office of Industrial Technologies, Industrial Energy Efficiency Division and Continuous

Fiber Ceramic Composites Program, under contract DE-AC05-84OR21400 with Martin Marietta Energy Systems, Inc.

ABSTRACT

Continuous fiber ceramic composites (CFCCs) are candidate materials for high temperature and structural applications. CFCCs are quite advantageous because they are lightweight structural materials that exhibit a much higher resistance to high temperatures and aggressive environments than metals and other conventional engineering materials. Cyclic fatigue is always an important issue in the mechanical behavior of structural materials. It is important to note that the damage mechanisms of CFCCs in fatigue are quite different from those experienced under monotonic mechanical loading.

The objective of this work was to provide some understanding into the monotonic and fatigue behavior of Nextel 312 and Nicalon plain-weave fiber fabric reinforced SiC matrix composites. Specifically, this was accomplished by examining the effect of fabric orientation with respect to the loading axis on the monotonic and fatigue behavior of the composite. Two geometries were investigated: transverse, where the fiber fabric was perpendicular to the loading direction; and edge-on where the fabric was parallel to the loading axis.

The edge-on geometry showed higher monotonic strengths than the transverse orientation. The different failure mechanisms in edge-on and transverse were due to, strong in-plane shearing of the fiber fabric and weak interlaminar shear of the plies, respectively. In cyclic fatigue, stress versus cycles (S-N) curves showed high fatigue endurance limits in both orientations, with the edge-on orientation having higher fatigue resistance.

In-plane shear strengths were higher than interlaminar shear strengths in both composite systems, which also explains the behavior of the two orientations in bending. Finite element analysis was successfully used in modeling stress

distributions in the two orientations. In the transverse orientation a compliant layer between two composite layers was used to simulate porosity and gap elements were used to simulate the extent of friction during bending. Friction and sliding effects were not present in the edge-on orientation.

Finite element results served to show that sliding and enhanced stresses caused premature failure in the transverse orientation, and the absence of friction effects accounted for higher strengths in the edge-on orientation .

TABLE OF CONTENTS

LIST OF FIGURES

CHAPTER I

INTRODUCTION

Continuous fiber ceramic composites (CFCCs) are being targeted as candidate materials for high temperature and structural applications (1-5). CFCCs are quite advantageous because they are lightweight structural materials that exhibit a much higher resistance to high temperatures and aggressive environments than metals and other conventional engineering materials. Potential applications include gas turbines, heat exchangers, and structural components in aerospace applications.

Most of these applications require engineering parts with high reliability (2). Monolithic ceramics, for example, are very brittle due to their high sensitivity to process and service-related flaws. Due to their low toughness, these materials fail catastrophically. One of the major advantages of continuous fiber ceramic composites (CFCCs) or whisker reinforced ceramic matrix composites (CMCs) is that these materials fail in a noncatastrophic manner (2,4).

The objective of this work was to obtain some insight to the monotonic and fatigue behavior of plain-weave fiber reinforced SiC matrix laminated composites, processed by chemical vapor infiltration (CVI). Specifically, this was accomplished by examining the effect of fiber fabric orientation, with respect to the loading axis, on the monotonic and fatigue properties of the composite.

This orientation effect has been investigated under impact conditions in a metallic laminated system (6). The study used notched specimens tested by the Charpy test. The authors chose to designate the geometry where the plies were perpendicular to the loading direction as crack arrester, and the geometry where the plies were parallel to the load as crack divider. In CFCCs however, due to the subcritical damage mechanisms, described in detail below, we cannot make the assumption that a single crack is propagating through the composite in a self-similar manner (i.e., only one principal crack is propagating through the material). Therefore, we designated the geometries, where loadings are perpendicular and parallel to the laminate layers, as transverse and edge-on, respectively, Fig. 1.

Two composite systems were studied: Nextel 312 (3M Corp.) reinforced SiC and Nicalon (Nippon Carbon Corp.) reinforced SiC, both fabricated by Forced Chemical Vapor Infiltration (FCVI). The behavior of both materials was investigated under monotonic and fatigue loadings. Finite Element Method (FEM) was used to model stress distributions in the two geometries to correlate with experimentally obtained results in monotonic loading. Stress versus cycles (S-N) curves were obtained from fatigue tests. The underlying mechanisms, in monotonic and fatigue loadings, were investigated primarily through post-fracture examination using scanning electron microscopy (SEM) to observe the extent of damage. Interlaminar and in-plane shear tests were conducted to further correlate shear properties with the effect of fabric orientation, with respect to the loading axis, on the mechanical behavior of the composites.

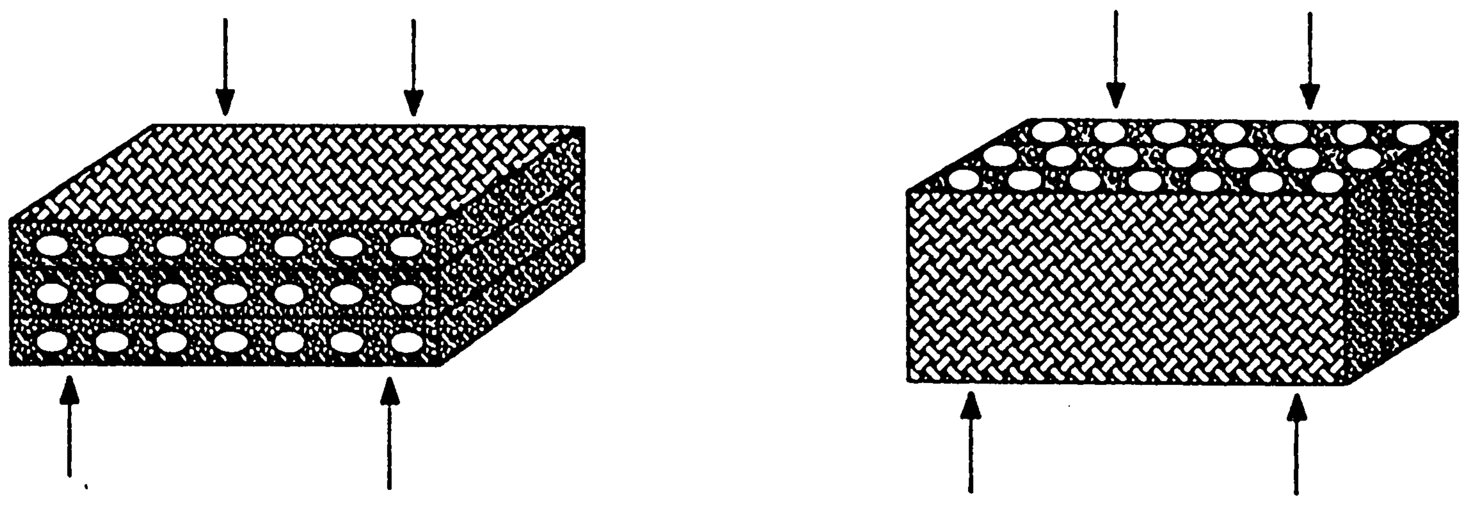

(a) (b)

Figure 1. Geometries for testing plain-weave fiber reinforced SiC matrix composites: (a) transverse and (b) edge-on.

CHAPTER II

LITERATURE SURVEY

DAMAGE MECHANISMS IN CONTINUOUS FIBER CERAMIC COMPOSITES (CFCCS)

The mechanical properties of CFCCs are very much dependent on the nature of the interface between fiber and matrix (1, 7). If the fiber is strongly bonded to the matrix, the energy at the crack tip at the interface will be high enough to fracture the fiber. In this case, the crack propagates straight through the interface and the fiber and the composite fails in a catastrophic manner. The stress-strain curve of such a composite will be similar to that of a monolithic ceramic and the composite will fail at the ultimate strength of the matrix. If the fiber/matrix interface is tailored (e.g., by an appropriate fiber coating, such as pyrolitic carbon), such that bonding between fiber (or whisker) and matrix is weak, a propagating crack will be deflected at the interface, causing it to lose energy. In this manner, debonding and sliding of the fiber with respect to the matrix acts as an energy-absorbing mechanism.

Fiber debonding is the first energy absorbing mechanism that occurs during failure of a weakly bonded CFCC, as shown in Fig. 2. It is followed by crack deflection at the interface, and finally, fiber pullout from the matrix which also serves to dissipate energy from the incoming crack. The stress-strain curve of a unidirectional ceramic composite, shown in Fig. 3, is linear until the matrix cracking point is reached. From the linear portion of the curve, the elastic modulus of the composite may be determined. After matrix cracking, the composite becomes more compliant until the ultimate strength of the composite

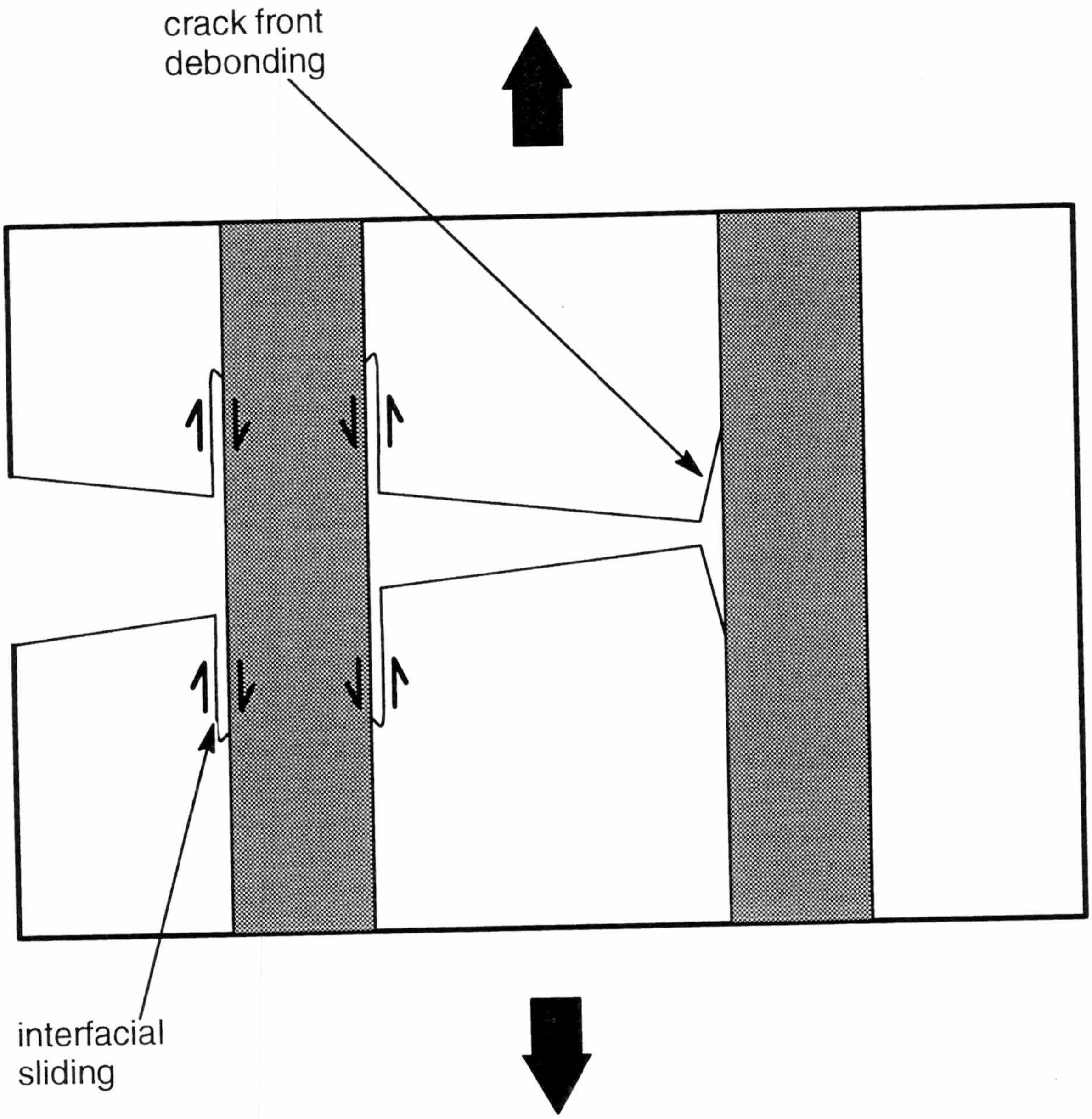

Figure 2. Debonding, crack deflection, and fiber pullout in a CFCC due to interface tailoring of the composite, such that bonding between fiber and matrix is weak.

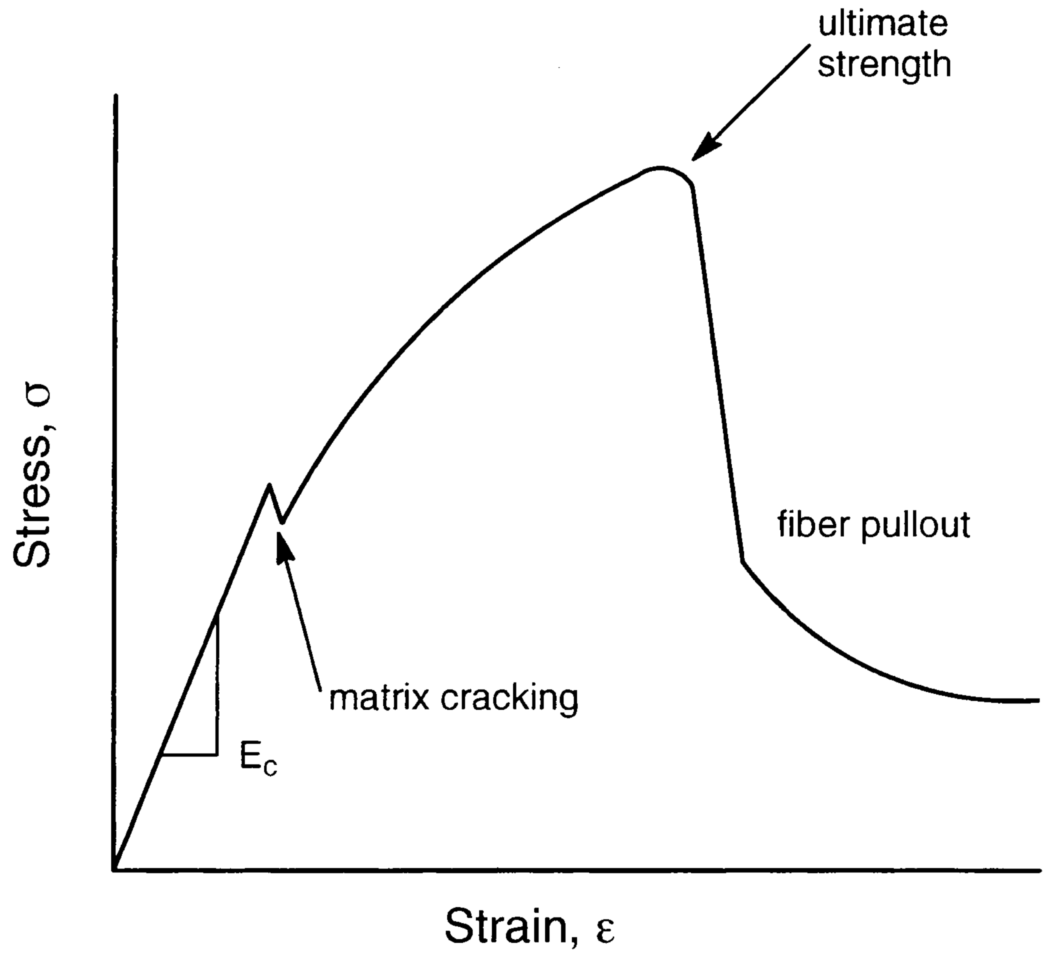

Figure 3. Stress-strain curve of a CFCC. With a strong interface, the composite fails at the matrix cracking stress, while with a weak interface, higher strength and toughness are obtained.

is reached. At this point, the fibers start fracturing and the stress-strain curve shows a relatively slow decline. In this tail portion, the fibers undergo pullout. Thus, in a fiber reinforced ceramic composite, we see a slow decrease in the stress rather than catastrophic failure, i.e., damage-tolerant behavior is achieved.

In isotropic monolithic materials subjected to mode I loading, a crack propagates perpendicular to the loading axis, that is, the crack propagates in a self-similar manner. On the other hand, CFCCs exhibit a highly diffuse damage zone because of the many subcritical damage mechanisms. In the area of CFCCs or whisker reinforced CMCs, the major problem in the applicability of linear elastic fracture mechanics (LEFM) to data obtained from fracture toughness and fatigue crack propagation tests is the lack of self-similar crack propagation (1).

In cyclic fatigue, subcritical damage mechanisms include fiber breakage and debonding, matrix cracking, and deflection of cracks at the weak fiber/matrix interface, see Fig. 4. These mechanisms, although similar to those in monotonic loading, may not occur in any particular order so the mechanisms in cyclic fatigue are inherently more complex.

EXPERIMENTAL RESULTS ON FATIGUE OF CFCCs

Until recently, it was thought that cyclic fatigue was not important in the case of ceramics or CFCCs (1). Only in the 1970s did researchers realize the importance of fatigue in CFCCs. For example, one of the potential applications of CFCCs is in automobile engines. A typical automobile gas turbine may be required, by design, to withstand 30,000 cycles of fatigue (8).

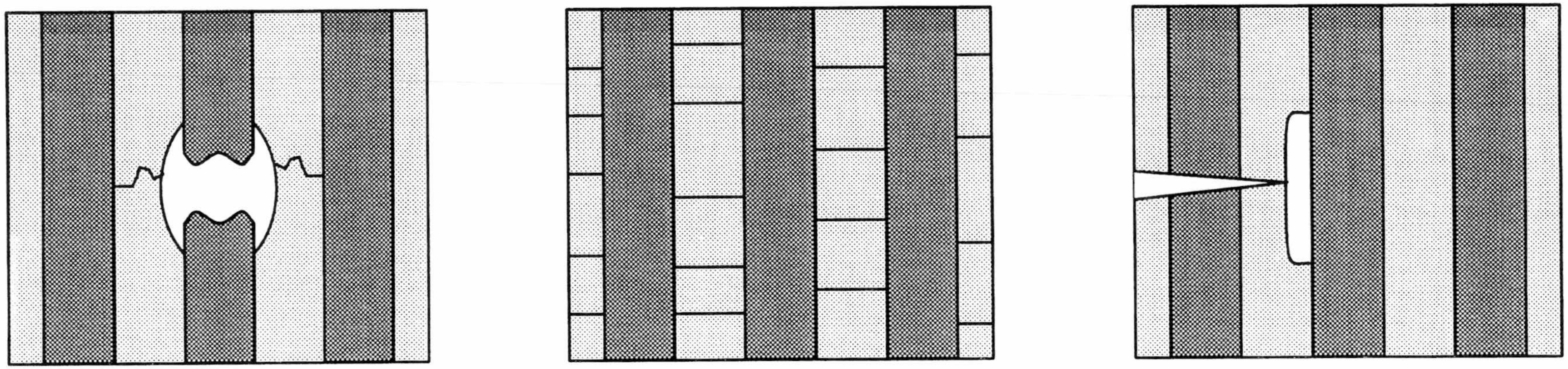

(a) localized debonding (b) matrix cracking (c) Deflection of principal crack

Figure 4. Schematic of damage accumulation mechanisms associated with cyclic fatigue in CFCCs: (a) localized interfacial debonding and fiber breakage, (b) matrix cracking, and (c) deflection of the principal crack. CFCCs exhibit a highly diffuse damage zone because of these subcritical damage mechanisms.

An important factor to consider in the fatigue behavior of CFCCs, in tension, is the stress under monotonic loading at which the stress-strain curve of the composite deviates from linearity (1, 9). This point, at which inelastic behavior begins, is termed the proportional limit stress, σ_{pl}. In unidirectional composites, only one proportional limit is observed, but in cross-plied composites, due to two or more different orientations of the fibers, two or more significant changes in the slope of the stress-strain curve may be observed. Some composite systems, such as carbon fiber reinforced SiC, however, have preexisting processing-induced defects so they do not exhibit a distinct proportional limit (9).

A comparison of damage evolution in CFCC laminates and metals is shown schematically in Fig. 5. In metals, little damage occurs during the first few cycles until a crack is nucleated. The crack, at first, propagates slowly and then increases rapidly. In CFCCs, on the other hand, damage is inherently present from processing effects. The rate of damage accumulation is much more gradual with increasing cycles, as compared to metals.

With fabrication techniques such as chemical vapor infiltration (CVI), woven laminated CFCCs have become very popular due to their quasi-isotropic properties and ease of processing (3). In these fiber reinforced composites, damage is quite significant in the early part of fatigue life due to first cracking in the 90° plies (1). The load is then taken up by the 0° plies so the damage is slowed considerably until final failure occurs.

During high temperature testing of CFCCs, it is important that a sufficiently high rate of loading (about 100 MPa/s) be applied so that creep deformation does not contribute to failure (9, 10). The proportional limit or nonlinearity in the stress-strain curve is usually taken to indicate the onset of matrix microcracking. The sensitivity of the instrument used to measure matrix cracking, however, may

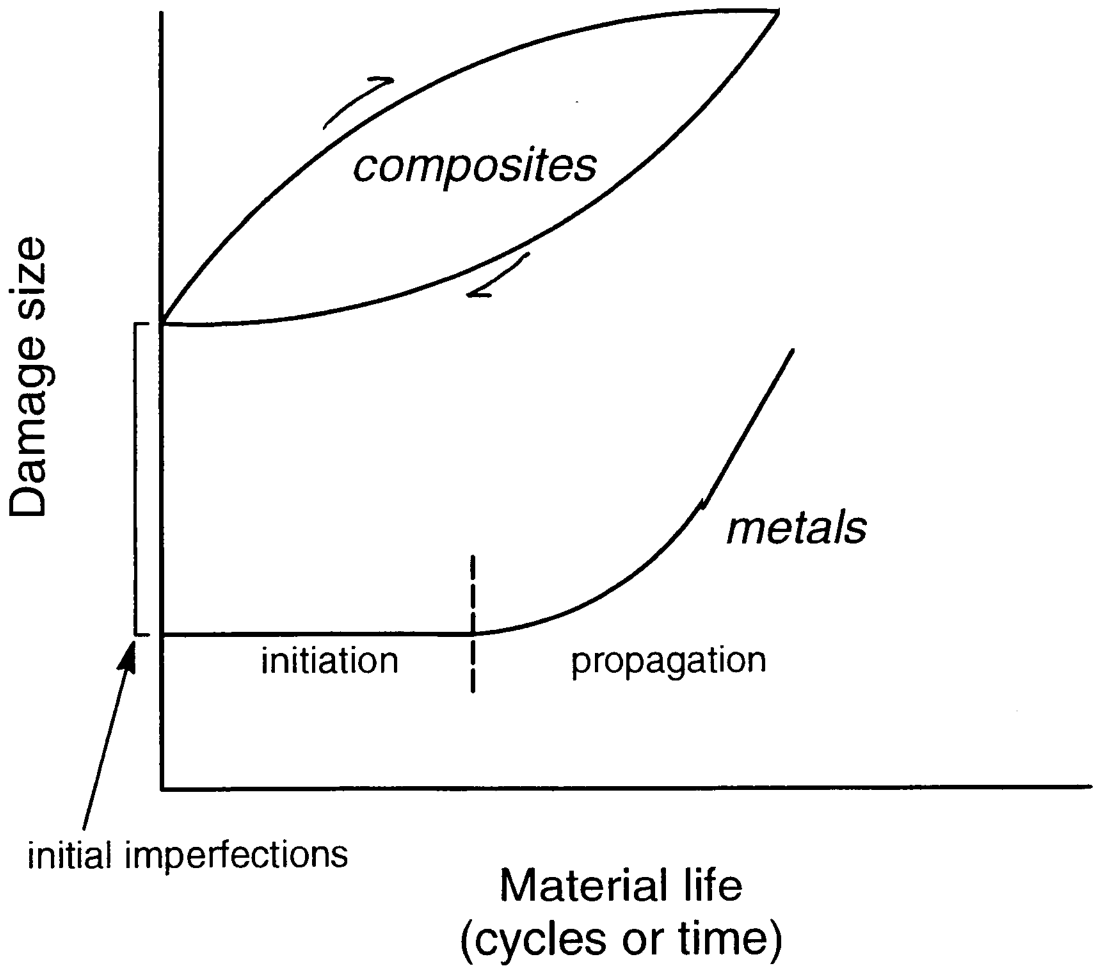

Figure 5. Comparison of damage evolution in CFCC laminates and metals.

not be sufficient to detect a measurable nonlinearity on a stress-strain curve. Other techniques such as on-line video systems, acoustic emission, surface replication, and atomic force microscopy (AFM) may be used to detect the start of matrix cracking in the composite.

Three major approaches have been used to study the fatigue behavior in CFCCs: stress versus cycles (S-N) approach, fatigue crack growth measurement (Paris relationship) approach, and elastic modulus reduction versus cycles approach.

Stress versus cycles (S-N) approach

In this approach, specimens are tested at a given R ratio (ratio of minimum stress, σ_{min}, to maximum stress, σ_{max}, applied to the test specimen) until failure occurs. A stress versus cycles curve is obtained which may be important in design considerations for the material.

The importance of the proportional limit in glass-ceramic matrix composites can be illustrated in work done on two different Nicalon/LAS (Lithium aluminosilicate) composites (11, 12). The difference between LAS I and LAS II was in processing, where two different nucleating agents were used to prepare the glass-ceramic matrix. This slight difference in processing resulted in a strong interface between fibers and matrix in LAS I, while LAS II had a weak interface. Due to the strong interface, under monotonic loading, LAS I showed linear tensile behavior to failure. LAS II, due to the weak interface, underwent extensive matrix cracking and its tensile behavior was nonlinear. After cyclic loading below the proportional limit, however, LAS I exhibited the same monotonic tensile strength as the virgin specimen. The same occurred when

LAS II was cycled below its proportional limit. When the LAS II composite was cycled at stresses higher than σ_{pl}, extensive microcracking of the matrix occurred resulting in a composite with lower modulus. The LAS I composite failed much more quickly when stressed above σ_{pl}, because of the strong fiber/matrix interface. The proportional limit, thus, is a key parameter that determines the fatigue life of glass-ceramic matrix composites.

In a study conducted on a Nicalon/borosilicate glass-ceramic composite, a power law relationship between cyclic stress and fatigue life was observed (13):

$$\sigma_{app} = \sigma_{uts}(2N_f)^b$$

where σ_{app} is the maximum applied stress, N_f is the number of cycles to failure, $2N_f$ is the number of reversals to failure (i.e., one cycle is equal to two reversals), σ_{uts} is the monotonic tensile strength, and b is a fatigue strength exponent. These researchers also used elastic modulus reduction to monitor the evolution of damage as a function of cycles. This aspect of their work will be discussed in a later section.

A significant problem in most composites, including CFCCs, is the mismatch between the coefficient of thermal expansion (CTE) of the matrix and fiber (1,7). This CTE mismatch can result in detrimental residual stresses after processing. For example, if the matrix shrinks more than the fiber then a compressive clamping stress is applied on the fiber, and an opposite tensile stress acts on the matrix. Therefore, when a cyclic load is applied to the composite, the fibers are subjected to tension-tension loading while the matrix is under tension-compression or compression-compression. A composite system that may be able to overcome these shortcomings is Nicalon fiber reinforced SiC. Nicalon fiber, although not stoichiometrically SiC, has a CTE of 3.1 x 10^{-6} K^{-1}, while CVI SiC has a CTE of 5.5 x 10^{-6} K^{-1} (14, 15). Since the CTE mismatch is rather low, this problem may be less severe. This composite is typically fabricated by chemical vapor infiltration of a preform made up of two dimensional woven fiber fabric (3). In the present study, similar types of CVI composites were examined under monotonic and fatigue loadings.

In a tensile test of a Nicalon reinforced SiC composite, it was determined that the matrix cracking stress was 54 MPa, and due to the two dimensional nature of the fiber architecture, another change in linearity was observed at 125 MPa (9). It was shown that fatigue run-out of this composite (i.e., the point at which no further loss in strength was observed as a function of cycles, taken here as being 1 x 10^6 cycles) occurred at 215 MPa, which was about 90% of the monotonic tensile strength of the composite. Another interesting result is that, unlike Nicalon/LAS composites, when the composite was stressed below the fatigue limit, a plateau in modulus was reached only after 10 cycles, indicating that the majority of damage in the material occurred in the initial stages of cyclic loading.

Considerable fatigue work has also been done at high temperatures on hot-pressed SiC fiber reinforced Si_3N_4 (16-18). In tests where the applied stress was above the proportional limit, there was a profound decrease in fatigue life. This was attributed to two factors: the cyclic propagation of cracks that formed during initial loading above the proportional limit and degradation of the fiber/matrix interface. The influence of stress ratio, R, was significantly different from that of metals (17). In metals, the fatigue life (number of cycles it takes to fracture a material at a given stress amplitude) usually decreases with increasing R. In this particular composite, however, as the stress ratio was decreased from 0.5 to 0.1

a decrease in fatigue life was observed. This indicated that the R ratio did not control the fatigue life of this system, above the proportional limit. Instead, crack propagation in the composite controlled the fatigue life. This was attributed to the high creep strength of SiC_f/Si_3N_4, so the behavior observed may not hold true for all CFCCs.

A very important point that may be true in other systems at high temperatures is that, in testing above the proportional limit, environmental degradation of the fibers and fiber/matrix interface may occur after matrix cracking, adding yet another variable to the fatigue mechanisms in CFCCs. The SiC_f/Si_3N_4 system, however, being processed by hot-pressing does not suffer from cracks initiating and propagating from pores, such as those inherently present in CVI composites.

Fatigue crack growth measurement (Paris relationship) approach

Fatigue crack growth may be analyzed by using the Paris power law relationship that relates the crack velocity, da/dN, and the cyclic stress intensity, ΔK (18):

$$\frac{da}{dN} = C\Delta K^m$$

where a is the crack length, N is the number of fatigue cycles, and C and m are constants.

Introducing a crack and controlling the velocity at which a crack propagates in a ceramic specimen is quite problematic, due to unstable crack growth that results in catastrophic failure. In order to produce stable fatigue crack growth, a technique has been developed to study the fatigue crack growth behavior of monolithic ceramics such as alumina and composites such as SiC whisker reinforced Al_2O_3, by means of compressive loading of notched specimens (20). In this method, notched specimens were pre-cracked under compressive cyclic loading until a small crack (on the order of 100 μm) was nucleated. Crack propagation occurred during the compressive cyclic preload until the final crack was arrested. This technique works well because when the compressive load is removed, a tensile residual stress is created at the crack tip.

After the compressive cyclic preload, fatigue studies in four-point bending were carried out by using a higher ΔK value than that applied during the preload, in order to induce crack propagation for crack growth rate measurements. In further studies of these composites, it was found that SiC_w/Al_2O_3 exhibited higher crack growth resistance than monolithic Al_2O_3 (21, 22). This was attributed to the formation of a zone ahead of the crack tip where microcracks were diffused and crack branching occurred. To account for this diffuse microcrack zone and still use the Paris law, several crack bifurcation equations were used to calculate the "true" crack length with respect to the number of cycles.

A comparison was also made between damage mechanisms in elevated temperature cyclic and static loading of SiC_w/Al_2O_3 (20). The mechanisms described above were observed in static as well as cyclic loading. Whisker bridging was more pronounced in cyclic loading which contributed to lower overall crack velocities.

It is important to note that due to crack branching and debonding at the whisker/matrix interface, the stress intensity at the crack tip, K_{tip}, is substantially less than the far-field stress intensity, K_I. To account for this, the authors obtained a relationship between the two stress intensities and microcrack shielding.

Interesting results have been obtained in tests dealing with the Nicalon/LAS system, using cyclic crack growth rate measurements (22). Crack propagation under fully reversible tension-compression loading was observed to be quite rapid at the beginning of the test but after about 200 μm of crack growth, a decrease in the crack growth rate was observed until final arrest occurred at 300 μm. This phenomenon was attributed to crack-tip shielding due to crack bridging by the fibers, which decreased the local stress intensity in the crack tip region. Mathematically, the stress intensity at the crack tip, K_{tip}, can be equated to the far-field stress intensity K_{in} less the crack shielding stress intensity (provided by reinforcing fibers) K_s such that (23):

$$K_{tip} = K_{in} - K_s$$

This shielding stress intensity, K_s, may be calculated from the influence of crack closure for a bridging zone of length a_o behind the crack tip through a frictional-slip model (24).

Elastic modulus reduction versus cycles approach

A good indicator of the amount of subcritical damage present in a composite under fatigue is the reduction in Young's modulus with respect to cycles. Such measurements have been conducted in polymer matrix composites (PMCs) (25) and metal matrix composites (MMCs) (26), and some CFCCs (13, 27, 28).

In a Nicalon/calcium aluminosilicate (CAS) glass-ceramic composite, a linear correlation between matrix crack density and modulus reduction in the composite was obtained (27, 28). Specimens were loaded in tension-tension fatigue and the Young's modulus and major Poisson's ratios were calculated from the slope of the unloading stress-strain curve after a given number of cycles. The crack density was measured as the number of cracks per unit length of the specimen in the gage area.

S-N type experiments on Nicalon reinforced borosilicate glass were used to obtain a relationship between modulus reduction versus number of cycles (13). The modulus reduction was plotted as a stiffness ratio of E, modulus at a particular stage of the test, and E_c, modulus of the composite before damage.

A fatigue damage model was developed, for simple unidirectional and [0/90°] cross-plied composites, correlating modulus reduction with number of fatigue cycles (13). The ratio E/E_c, was correlated to any number of cycles (i.e., from N = 0 to N = N_f - 1, where N_f is the number of cycles needed for composite failure) as well as the coefficient of friction between the matrix and the fiber, obtained from a simple fiber pushout test.

BENDING STRESS ENHANCEMENT DUE TO SHEAR IN WEAKLY BONDED LAMINATES

Flexure or pure bending tests are commonly used to determine mechanical properties of CFCCs, because of the relative ease and inexpensiveness of testing compared to tensile tests (29,30). Moreover, although tensile testing is very important, it suffers from problems of grip failures, misalignment of specimens, and comparatively higher machining costs (1,10,29,30).

We can derive the equations that govern pure bending by using two basic equations (1,31):

$$\frac{M}{I} = \frac{E}{R} \text{ and } \frac{M}{I} = \frac{\sigma}{y}$$

where M is the applied bending moment, I is the moment of inertia of the beam, E is the elastic modulus of the material being tested, and R is the radius of curvature of the beam at an applied axial stress, σ, at a distance y from the neutral axis.

If we consider a beam of rectangular cross-section, the moment of inertia is given by (31):

$$I = \frac{bh^2}{12}$$

where b and h are the width and height of the beam, respectively. Figure 6 shows the normal stress distribution as a function of the thickness in an elastic beam. At the neutral axis the stress is zero, and the stress and strain vary linearly through the thickness. Below the neutral axis the material is in tension while above it the material is in compression.

To calculate the maximum tensile stresses in the beam, then, for a symmetrical rectangular section, as described above, y can be substituted for h/2. The axial stress on the beam, can be written as (1,31):

$$\sigma = \frac{My}{I} = \frac{M\frac{h}{2}}{\frac{bh^3}{12}} = \frac{6M}{bh^2}$$

For a beam in three-point bending:

$$M = \frac{P}{2} \cdot \frac{S}{2} = \frac{PS}{4}$$

We can then write,

$$\sigma = \frac{6PS}{4bh^2} = \frac{3PS}{2bh^2}$$

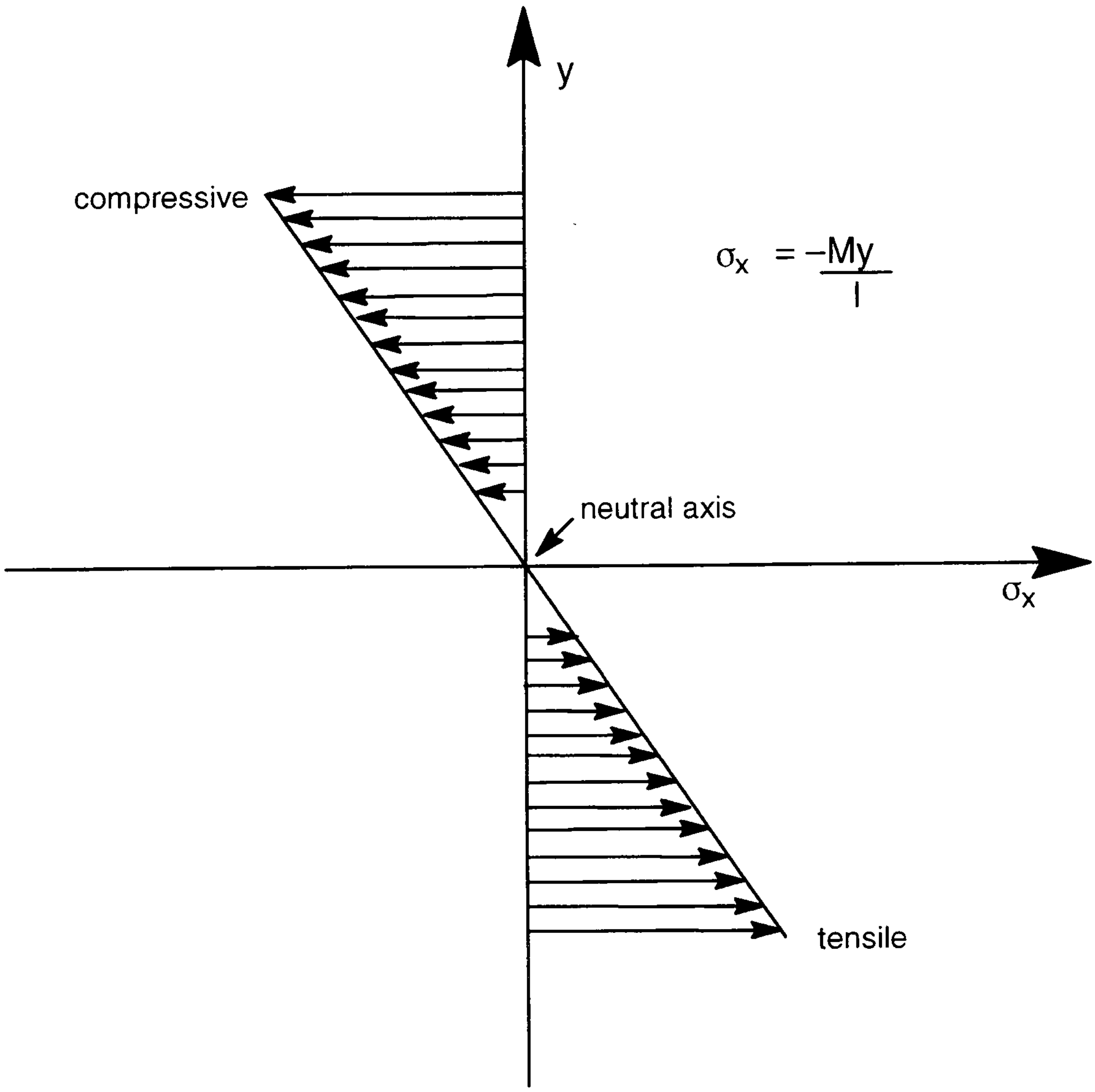

Figure 6. Normal stress distribution as a function of thickness in a purely elastic beam. At the neutral axis the stress is zero, and the stress and strain vary linearly throughout the thickness.

where P is the applied load and S is the span of the beam. Similarly, for four-point bending, we have,

$$M = \frac{P}{2} \cdot \frac{S}{4} = \frac{PS}{8}$$

$$\sigma = \frac{6PS}{8bh^2} = \frac{3PS}{4bh^2}$$

Normal stress and bending moment diagrams for three- and four-point bending are shown in Fig. 7, respectively. Notice that in four-point bending, a larger portion of the beam is subjected to the maximum stress and bending moment.

Using simple beam theory, we can observe the effect of beam aspect ratio (half span length/height) on the degree to which the tensile axial stresses exceed the shear stresses in the beam. For three-point bending:

$$\tau = \frac{3P}{4bh} \text{ and } \sigma = \frac{3PS}{2bh^2}$$

Thus,

$$\frac{\tau}{\sigma} = \frac{h}{2S}$$

Therefore, if S/h is very large (i.e., large span-to-height ratio) then the normal stress is much larger than the shear stress present in the beam, so failure is more likely to occur in tension rather than in shear.

In brittle materials, such as monolithic ceramics, strength values obtained in a bend test are generally higher than those obtained from a tensile test (32-34). This is particularly true of CFCCs. There is, however, no simple proportional relationship between bending and tensile strengths for different CFCC material systems.

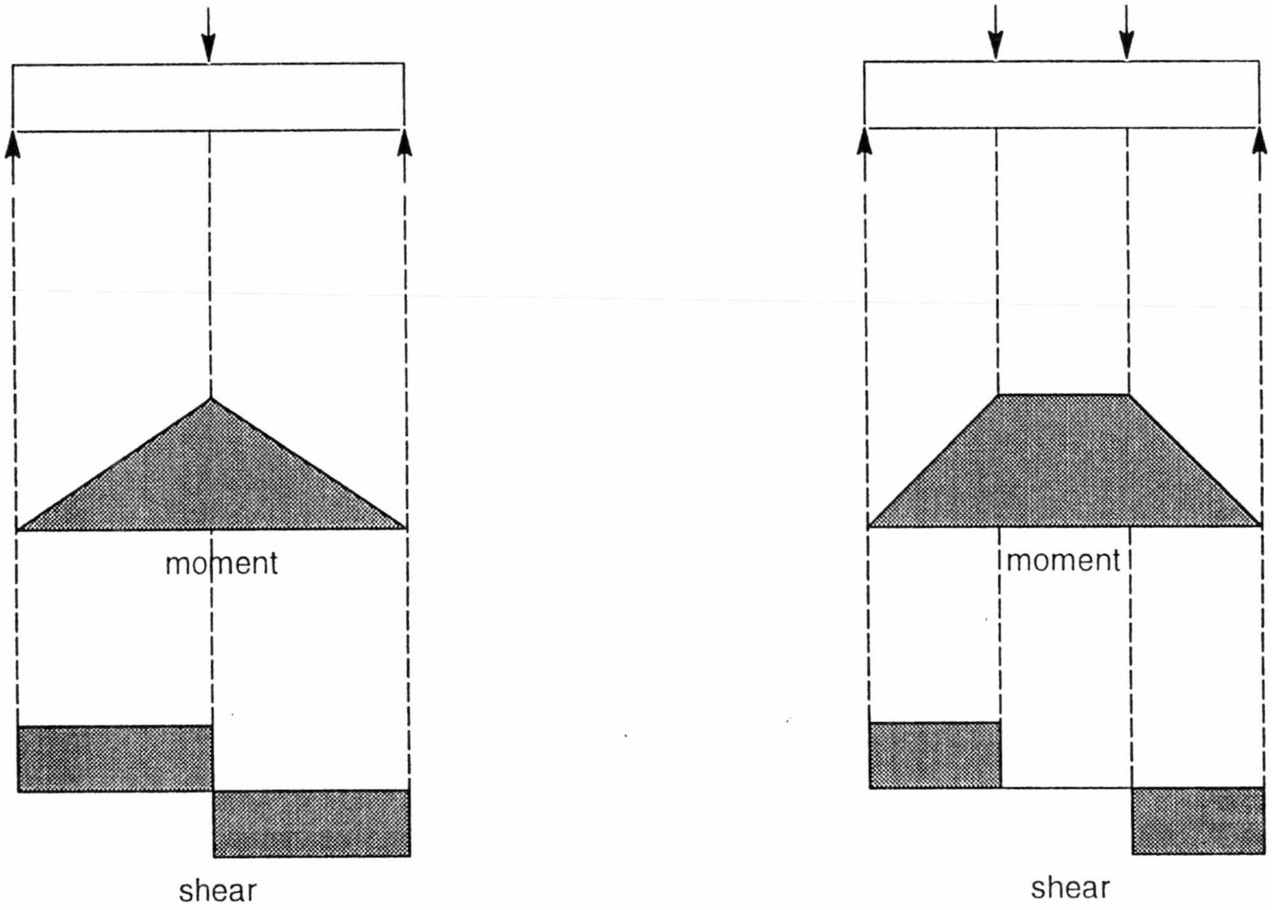

(a) (b)

Figure 7. Normal stress and bending moment diagrams for a beams in (a) three-point bend and (b) four-point bend.

Several reasons are cited for the discrepancy between bending and tensile strengths in CFCCs, such as non-uniform stress distribution in a flexure bar, anisotropy of fiber architecture, especially in the case of woven laminates, where the fiber fabric can be oriented at different angles in a given ply, different tensile and compressive behavior of CFCCs, and low interlaminar shear strength in laminated CFCCs (30). The latter effect is very important and will be discussed in detail later in this section.

The ASTM standard in preparation, while acknowledging these shortcoming of the flexure test, still proceeds to describe computations of stresses in the beam using linearly elastic beam theory along with assumptions that the beam is homogeneous and isotropic. This flexure strength value, while not the *actual* strength value, is proposed to be used for comparative type testing that would be useful in quality control and component development (30).

In monolithic ceramics, strength in flexure is inversely proportional to density of flaws. The higher the number the flaws in the portion of the bar subjected to stress, the higher the probability that one of those flaws will be the strength limiting flaw (1,30). CFCCs also suffer from test volume dependence on strength, due to porosity (which acts like flaws), and the probabilistic strength distribution of ceramic fibers and matrices. Therefore, the four-point bend geometry provides a more conservative estimate of strength than three-point bend because more of volume of the test specimen is subjected to the maximum bending stress (30).

It should be noted that due to the variety of subcritical damage mechanisms present in CFCCs, flexure test results of these materials are dependent on a variety of test conditions such as testing fixture (three- or four-point bend), loading rate, surface finish of the specimen, and testing environment (30).

A comparison between a solid beam and a composite beam will illustrate the difference between bending and tensile behavior. The first assumption in pure bending is a geometrical assumption that elongations (and therefore strains) in a beam vary linearly with distance from the neutral axis, which, for a rectangular or square cross-section occurs at the center of the beam (31). The second assumption is that Hooke's law applies to each individual part of the beam such that the stress is proportional to strain and the elastic modulus, E, is the same in tension and compression. Poisson effect (i.e., contraction of the beam on the tensile side and expansion on the compressive side) between different layers of the beam is ignored, so the normal stresses that result from bending also vary linearly with respect to the neutral axis.

In CFCCs, however, as described above, a proportional limit is observed in a typical stress-strain curve. It has been pointed out by several authors in CFCCs as well as the polymer matrix composites (PMCs) area, that when the proportional limit is exceeded in a bend test, the neutral axis is shifted toward the compressive side from its position at the center of the beam (32-34). In CFCCs this is because a decrease in modulus occurs in tension at a lower strain than in compression, i.e., the moduli in tension and in compression are not the same. Such a discrepancy in moduli of a CFCC comes about because flaws collapse in compression and have little detrimental effect on strength, while in tension these flaws easily propagate and coalesce with each other to cause premature failure. Because of shifting of the neutral axis, the third assumption of pure bending is violated, and simple beam theory equations are no longer useful in calculating stresses in the beam.

Another explanation for the discrepancy between tensile and bending strengths in CFCCs is that in a simple beam, the *entire* beam fails once the

applied moment reaches some critical value, M_{uts}, when the stress on the tensile side of the beam exceeds the ultimate tensile strength (32-34). In a CFCC beam, however, when M_{uts} is exceeded, the beam does not fail but it continues to sustain load, while the stress distribution beyond this point is still linear. In order for the net applied axial load to be in equilibrium, tensile forces must be counteracted by compressive forces, and since the compressive strength is very high, balance of the forces occurs by a shifting of the neutral axis by some distance y_c, Fig. 8. This shift will occur until final failure of the bar, but the important point is that a significant
amount of load is still being applied after initial failure of the tensile face of the specimen, which corresponds to the ultimate tensile strength. Therefore the bending strength is substantially enhanced over the tensile strength of the material.

EFFECT OF LOW INTERLAMINAR SHEAR STRENGTH

Several analytical solutions have been derived for interlayer slip between layers in bending. Murakami (35) developed an analytical solution for interlayer slip to examine stiffness degradation in laminate beam structures. This theory, however, requires the implementation of a characteristic "slip law" for a given system. In this work, the term slip refers more to an interlayer adhesively bonded to constituent layers, instead of actual friction between layers.

Krzys and Trojnacki (36,37) examined the buckling of thin circular rings bonded by friction. They found that when the shear stresses exceeded a critical point defined by the coefficient of friction, slippage began to occur.

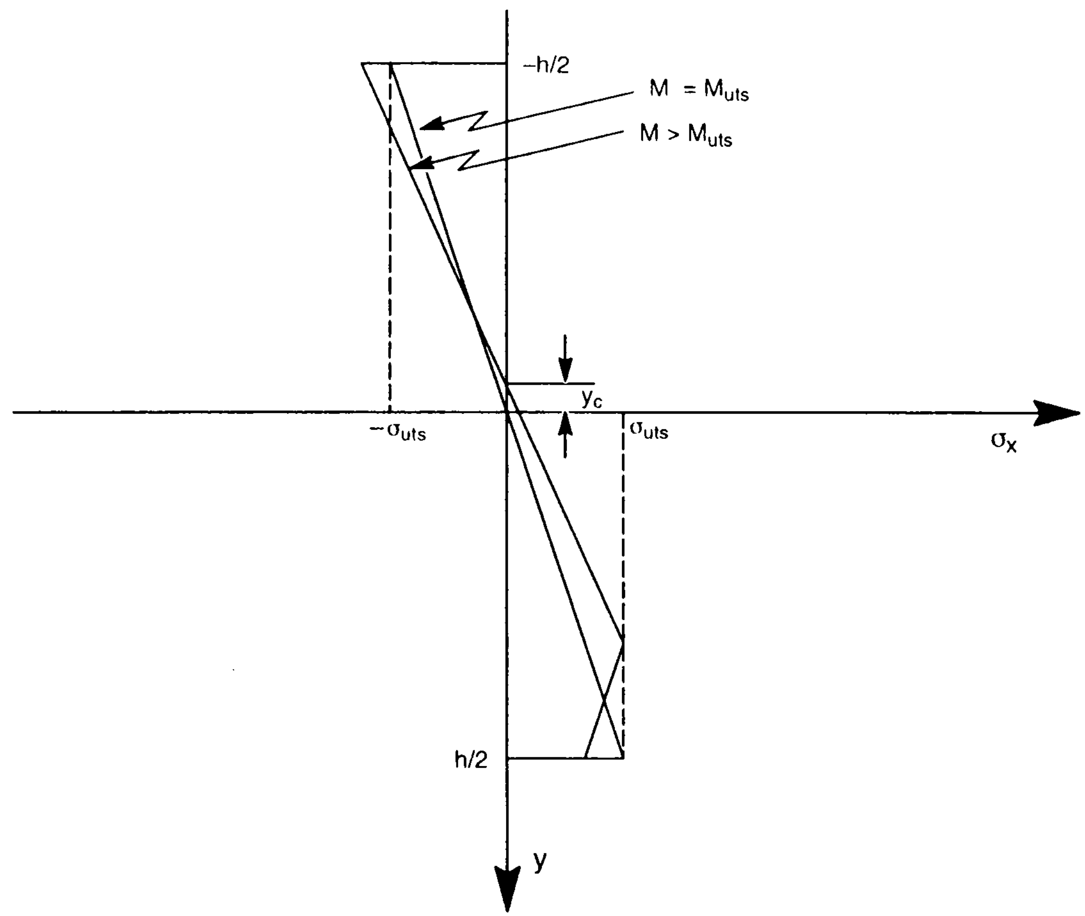

Figure 8. Shifting of neutral axis in a CFCC beam subjected to bending.

Finite difference methods have been used in the analysis of stresses and deflections of multilayered diaphragm composite structures (38). Finite element methods were used to examine the effect of interlayer slip, different material properties, and gaps between pieces of sheathing in layered wood composite systems (39). Systems with no gaps sustained higher loads and had lower deflections at the midspan of the beam.

In the all the works described above, however, the enhancement of bending stresses due to shear between layers, the effect of friction between layers, and the effect of span on the bending stresses was not investigated.

An approach that proposes to relate the bending strength of a CFCC beam with its interlaminar shear strength is given by Steif and Trojnacki (32-34). They assume that the plies in a composite are bonded with an interlaminar shear strength τ_p. Axial stresses in the beam are linearly related to axial strains (i.e., no non-linearity in the stress-strain curve is considered at this point), but a "plastic zone" is defined where only shear stresses are present. If a part of the beam is subjected to a shear force V and bending moment M, the authors arrive at the plastic zone thickness:

$$h_p = \left(3\frac{V}{V_{\max}} - 2\right)h$$

where V_{max} is the maximum shear force given by $bh\tau_p$, and V is some value between $2V_{max}/3$ and V_{max}. The maximum axial stress on the tensile side of the beam is then given by:

$$\sigma_{\max} = \frac{Mh}{9I}\left[\left(1 - \frac{V}{V_{\max}}\right)\left(\frac{V}{V_{\max}}\right)\right]^{-1}$$

For the case of three-point bending, a span length 2L and under a load, P, the bending moment, M, is given by PL and the shear force V is equal to P so we can rewrite the last equation as:

$$\sigma_{max} = \frac{4Lb\tau_p^2}{3(bh\tau_p - P)}$$

Steif and Trojnacki, then define the strength ratio, P/P_{bend}, where P_{bend} is the load required for failure of a beam of span long enough such that no shear effects are present. P is the load at a given aspect ratio and τ_p. The strength ratio is equated to the aspect ratio and τ_p as follows:

$$\frac{P}{P_{bend}} = \begin{cases} \left[3 - 2\frac{2L}{h}\left(\frac{\sigma_{bend}}{\tau_p}\right)^{-1}\right]\frac{2L}{h}\left(\frac{\sigma_{bend}}{\tau_p}\right)^{-1} & \left(\text{for } 0 \le \frac{2L}{h} \le \left(\frac{2L}{h}\right)^*\right) \\ 1 & \left(\text{for } \frac{2L}{h} > \left(\frac{2L}{h}\right)^*\right) \end{cases}$$

where 2L/h is the aspect ratio or span-to-height ratio of the beam and (2L/h)* is the critical aspect ratio above which shear effects are not present. This inverse relationship between aspect ratio and bend strength has also been observed in PMCs and MMCs (40, 41).

The composite systems investigated in our work typically suffer from very low interlaminar shear strength. The interlaminar shear strength was measured using a double notched fixture, which is described in detail later. In flexure, such shear effects can substantially increase the bending loads, causing failure at much lower stresses than would otherwise be predicted from simple beam theory (32-34). Comparisons by Steif and Trojnacki, with several glass matrix composites, show good correlation. Parametric plots, using the equations described above, of P/P_{max} versus 2L/h are given as a function of σ_{max}/τ_p in Fig. 9.

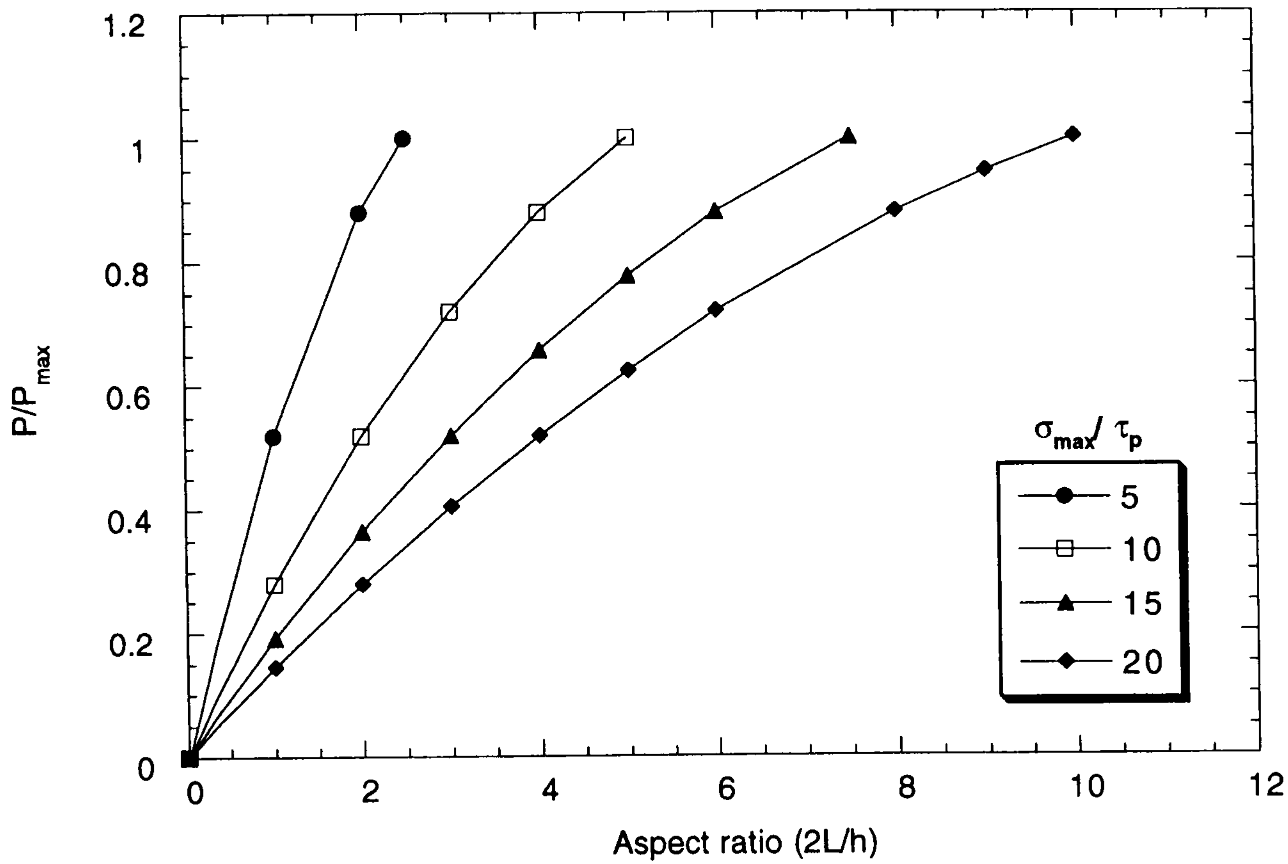

Figure 9. Parametric plots of σ_{bend} versus 2L/h, derived from equations by Steif and Trojnacki (32-34).

Note that as the σ_{max}/τ_p ratio increases, the effect of aspect ratio on P/P_{max} decreases. In the present work, FEM analysis was used to further provide a quantitative understanding of shearing in weakly bonded laminated CVI composites.

It is interesting to note that in work conducted on three dimensionally (3-D) reinforced Nicalon/SiC, proportional limits and ultimate strengths obtained in flexure were about the same as those in tension (42). This behavior can be attributed to the absence of low interlaminar shear strength in these composites. The authors also indicated that "graceful" failure observed in the stress-strain curve was only obtained in flexure because of shifting of the neutral axis, as described above. Furthermore, because of shifting of the neutral axis in flexure, the authors mention that the tensile test is a better test to characterize the failure process of these 3-D composites.

EXPERIMENTAL RESULTS ON INTERLAMINAR AND IN-PLANE SHEAR OF COMPOSITES

Interlaminar shear of composites

Three major tests are used to determine interlaminar shear strengths in fiber reinforced composites: Short beam in three-point bending, double notched shear test, and modified Iosipescu shear test (43-53). Since very little shear testing has been done in the area of CFCCs, the review presented here consists primarily of work done in the polymer matrix composite (PMC) area.

In a short beam test, a beam with very short span-to-width ratio (typically less than five) is tested in three-point bending (45). In principle, failure should occur by shear at the neutral axis of the beam. However, failure by flexure as well as non-uniform stress distributions along the beam cause variations in strength from specimen to specimen (44,45). Nevertheless, this technique is simple and machining of CFCCs is minimal for this test.

The short beam test has been examined for unidirectional polymeric composites and deemed appropriate for carbon and glass fiber reinforced epoxy, with as narrow a span as possible (46). It was observed that short beam tests were not suitable for angle-ply composites because of complex ply interactions that occur at the beam edges, and that can substantially change the distribution of stresses.

The double notched test involves a specimen notched on opposite sides, and loaded in compression, such that the longitudinal plane between the notches is subjected to pure shear (44, 47). The interlaminar shear strength is computed by dividing the applied load by the area of the plane in shear. A jig is sometimes fixed to the specimen in order to prevent failure by buckling, but it may affect the measured shear strength due to friction between the jig and the specimen. It has also been shown that uniformity of shear stresses is not always present in this test (47). This test is also quite inexpensive and simple to conduct and specimen machining is also minimal. In addition, it has been reported that in double notched experiments of CFCCs, shear failure occurred consistently (44). Finally, it has been shown for polymeric matrix composites that the difference between nominal shear stress and localized shear stresses decreases as the ratio of length to thickness decreases, so truer strength results may be obtained for small values of the length to thickness ratio (48).

In terms of design purposes, work done on carbon/carbon composites has shown that interlaminar shear strength values obtained by double notched methods are lower than those from other methods, therefore providing a conservative estimate of the failure strength in shear (49).

In-plane shear of composites

Iosipescu (50), using Moire fringe analyses, showed that a variety of shear testing procedures have non-uniform shear stress distributions in isotropic materials, namely metals such as steel and aluminum. A schematic of the test fixture used by Iosipescu for in-plane shear tests is contrasted with the double notch fixture used in interlaminar shear tests, Fig. 10.

The test fixture for in-plane shear testing, called the modified Wyoming shear-test fixture, can also be modified for interlaminar shear testing. It consists of a double V-notched specimen (one on each side), that is subjected to an asymmetric moment, such that only pure shear forces are present and bending moments are absent in the test. Iosipescu in-plane shear tests of composites are very costly and machining of the notches is very tedious and time consuming. A modified version of the Iosipescu in-plane shear test can be applied to interlaminar tests by simply bonding the laminate to aluminum tabs and applying the force such that the plane under stress is in shear (48). Thick laminated polymer matrix composites have also been tested using this method (51).

The effect of interaction between specimen and the modified Wyoming shear-test fixture, used for in-plane and interlaminar shear testing, has been examined (52). Strain gauges were used to determine fixture induced strains. It was observed that although an asymmetric moment is assumed across the load, nonasymmetric strains are observed due to differing compliance between the

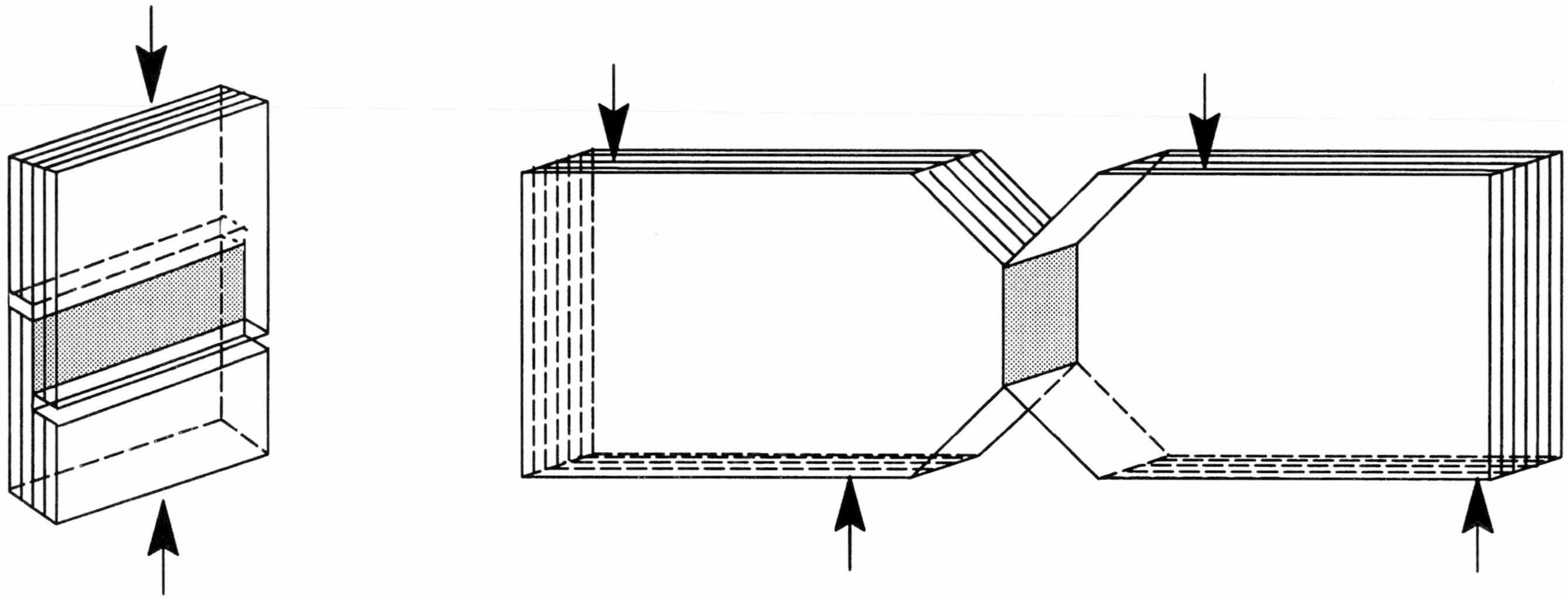

Figure 10. Schematic of the difference between interlaminar and in-plane shear in laminated composites.

two halves of the fixture. Out of plane moments were also observed, but these were not significant compared to the applied moment on the specimen. In tests with carbon fiber reinforced epoxy laminates, the degree of misalignment was found to substantially increase the error in observed shear modulus.

Work on in-plane shear testing of several graphite fiber fabric reinforced epoxy composites, using the Iosipescu shear test, showed that fabric yarn thickness influenced the shear stress fields in the gauge section of the specimen, but that observed shear moduli were consistently obtained with this test (53).

BACKGROUND ON THE FINITE ELEMENT METHOD (FEM)

A number of numerical analysis methods have been used to solve a variety of engineering problems (54, 55). Finite element method (FEM) solves a given problem by building a geometry with an array of small subregions, called elements (54). The governing equations are approximated in a piecewise fashion. FEM approximates the unknown variables of differential equations based on a model created to simulate a real structure. The mathematical model involves the subdivision of a structure into elements that are connected by nodes, and equations are generated and solved for each of the elements.

In general, the type of analysis may be categorized as linear or non-linear. In a linear analysis, the solution is computed by solving the following general equation (55):

$$[A]\{x\} = \{F\}$$

where [A] is the stiffness matrix of the structure, {x} is a vector quantity which prescribes the numbers of degrees of freedom to the system, and {F} is a vector of known quantities (such as applied loads and displacement constraints).

In a nonlinear problem, an iterative procedure is used such that a solution may converge or diverge (55). If the solution diverges, the model, i.e., the applied loads or displacements, or mesh size, need to be changed until a converging solution is obtained. The general equation used for solution of a nonlinear problem is:

$$[A(x)]\{x\} = \{F\}$$

where [A] is now a function of an unknown degrees of freedom as well. Therefore, this equation cannot be solved explicitly, and an iterative solution is necessary.

CHAPTER III

MATERIALS AND EXPERIMENTAL PROCEDURE

PROCESSING BY FORCED CHEMICAL VAPOR INFILTRATION (FCVI)

The composites used in this study were processed by forced chemical vapor infiltration (FCVI). In principle, FCVI takes advantage of a thermal gradient that allows reactant gases to effectively deposit the matrix on a fibrous preform and densify the composite, Fig. 11. Details of the FCVI fabrication process are given elsewhere (3). Nextel 312 and Nicalon fibers were used as reinforcements for the CVI SiC matrix. Nextel 312 is an oval polycrystalline fiber with minor and major axes lengths of 8 and 12 μm, respectively, composed of Al_2O_3, SiO_2, and B_2O_3, Fig. 12(a). Nicalon is a circular amorphous fiber, about 15-18 μm in diameter, composed of Si, C, and O, Fig. 12(b). The fibers were woven into a plain-weave fabric and before infiltration, the fabric was coated with chemically vapor deposited (CVD), 0.3 μm thick, pyrolitic carbon to provide the weak interface necessary for tough behavior in these composites. Nextel and Nicalon reinforced composites were processed at Oak Ridge National Laboratory (ORNL) and BF Goodrich, respectively.

The Nextel reinforced SiC composite was fabricated in disk form to a final diameter of 24 cm (9.5") and thickness of 1.25 cm (0.5"). The Nextel plain weave [0/90] fabric was stacked at a fabric orientation of [0/30/60]. Therefore, the orientation of the fibers was [0/90], [30/120], and [60/150], see Fig. 13. The micrograph shows the plain-weave fiber fabric that was infiltrated. The

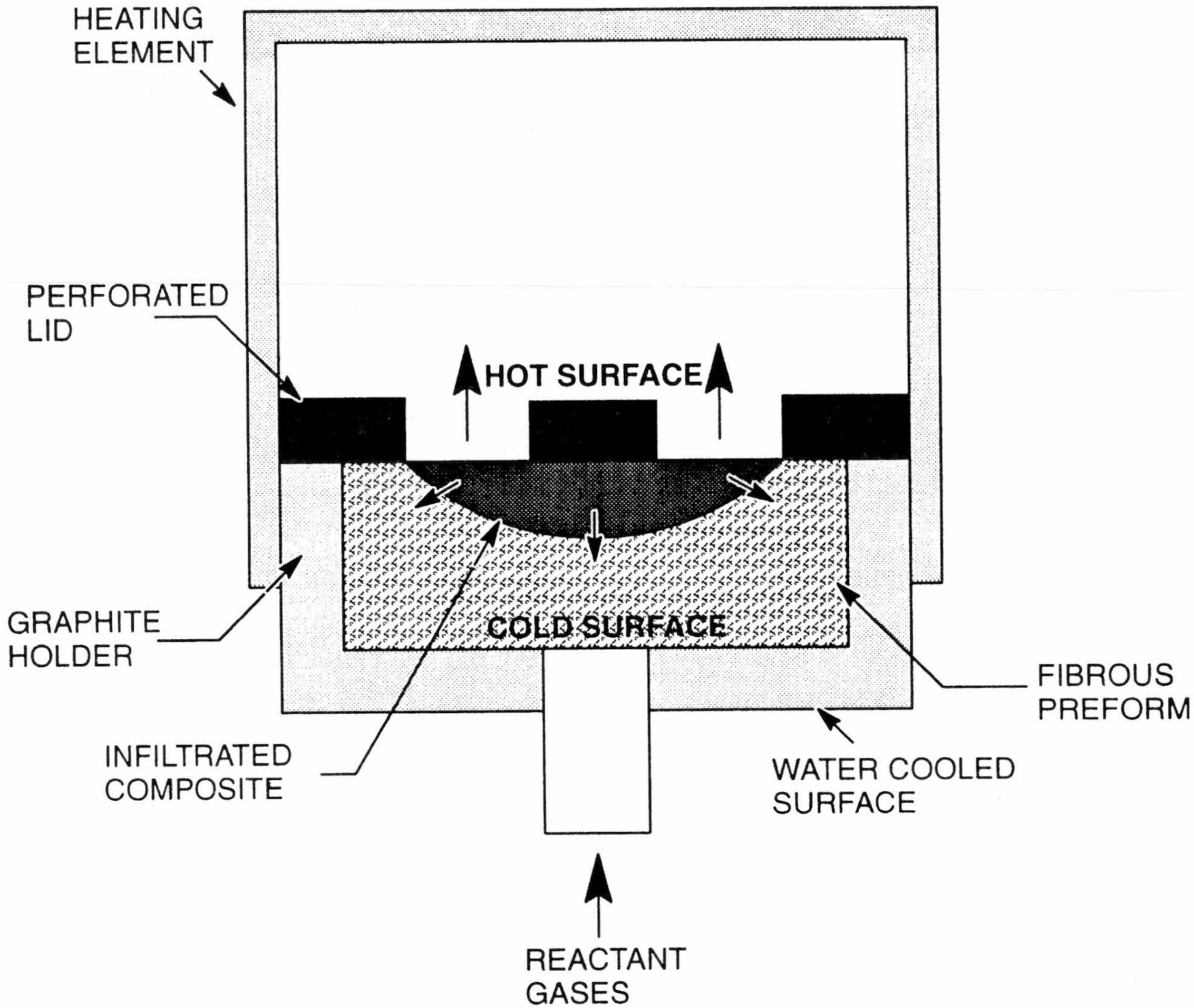

Figure 11. Schematic of the experimental set-up for Forced Chemical Vapor Infiltration (FCVI) of SiC matrix composites.

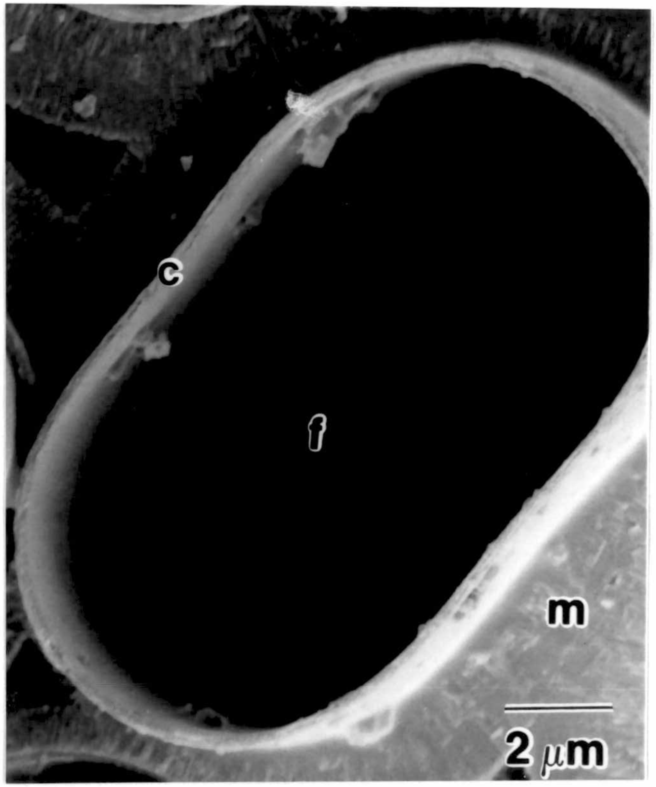

(a)

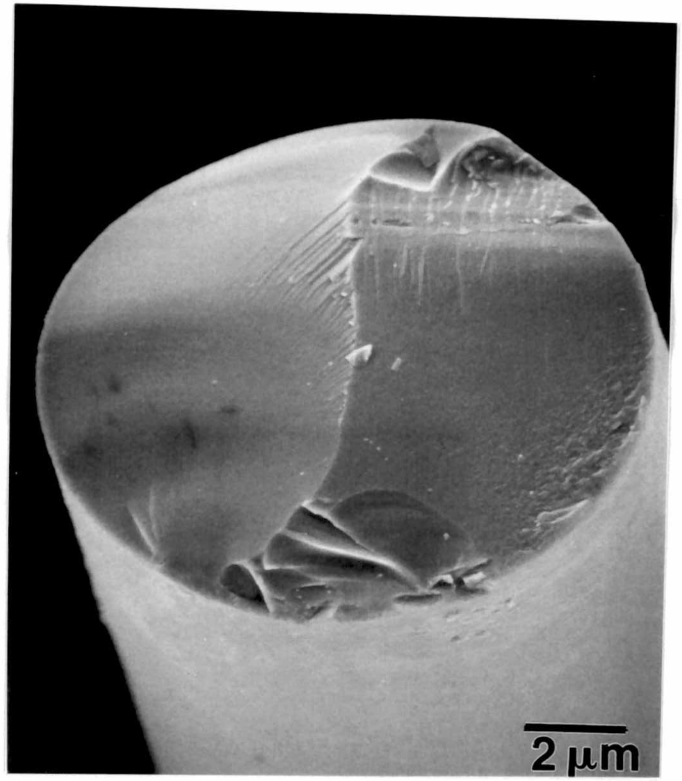

(b)

Figure 12. Fibers used to reinforce SiC matrix (a) Nextel 312, a polycrystalline fiber composed of Al_2O_3, SiO_2, and B_2O_3 and (b) Nicalon, an amorphous fiber made of Si, C, and O.

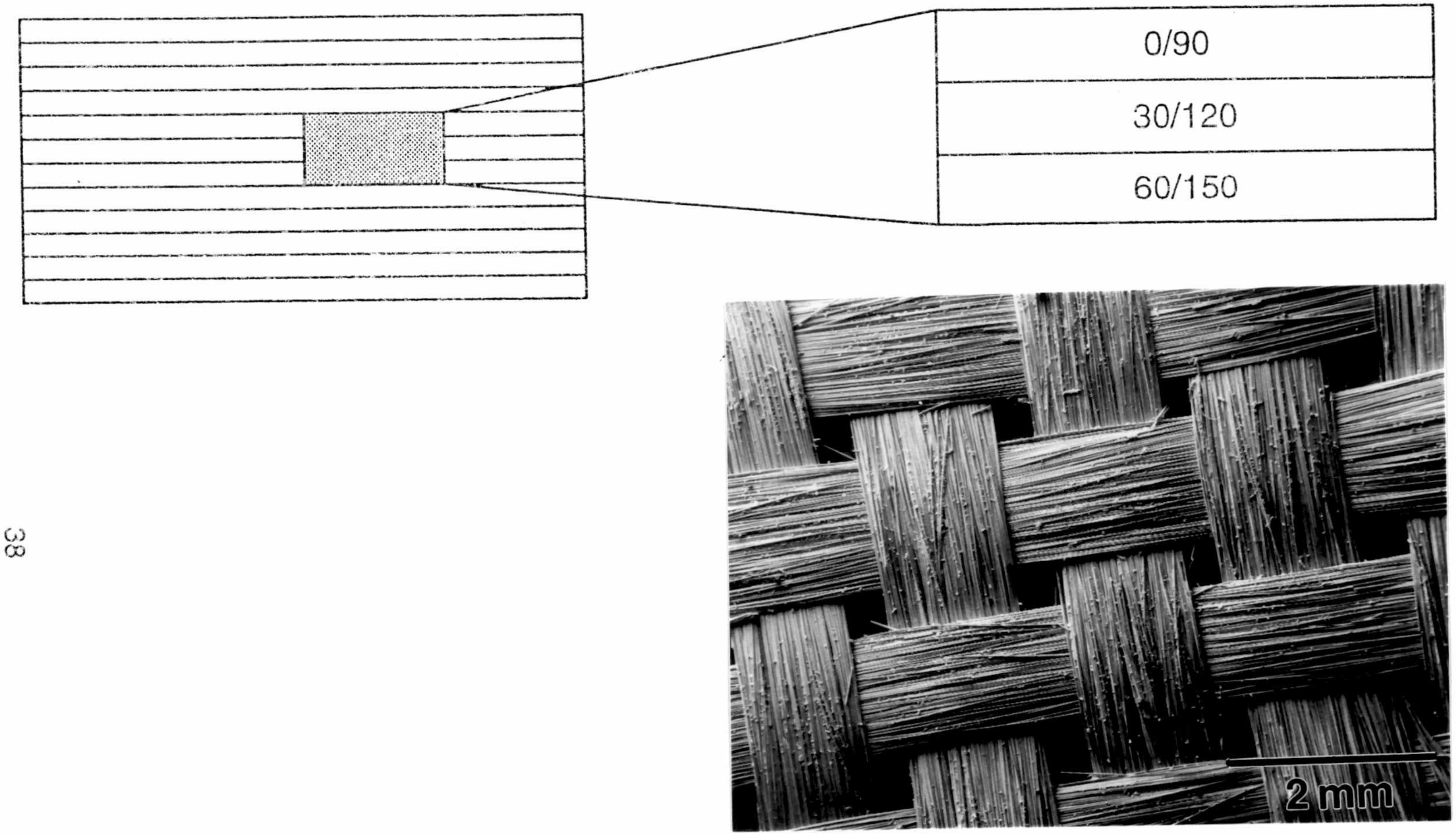

Figure 13. Schematic of plain-weave fiber fabric ply orientations in Nextel/SiC composite. The micrograph shows a plain-weave fabric made of Nicalon fibers.

composite had 10 plies per 0.25 cm (1/10") and a nominal fiber volume fraction of 40%. Density measurements were obtained using Archimede's principle.

The Nicalon reinforced composite had a simpler stacking sequence of [0/90] for all plies. The number of plies per unit thickness were the same and the coating applied to the fiber fabric was identical to that deposited on Nextel fibers. The composite was also infiltrated by FCVI method but the plate was an 21 cm x 21 cm (8"x8") plate of 0.35 cm (0.138") thickness.

Monotonic and fatigue flexure testing

Flexure bars were cut to the following dimensions: length, 50 mm; width, 3 mm; and thickness, 3 mm (~12 plies/specimen). The commonly used standard calls for a width of 4 mm, but in order to compare the two geometries in a fair manner, the width and thickness were cut to the same dimension. Monotonic tests were conducted in four-point flexure with major and minor spans of 40 mm and 20 mm respectively, at a constant cross-head displacement rate of 0.5 mm/min. Flexural fatigue tests, also in four-point flexure, were done in load control using a triangular waveform at a frequency of 0.33 Hz. A constant R ratio ($\sigma_{min}/\sigma_{max}$) of 0.02 was used. Specimens that survived 10^5 cycles were fractured under monotonic loading to obtain the post-fatigue strength. Fracture surfaces were examined in a scanning electron microscope (SEM).

Limited tensile tests were conducted on dog-bone specimens with a 25 mm gage length. Glass/epoxy tabs were glued on the specimen ends of the composite to prevent crushing in the grips. Uniaxial tension tests were conducted at a cross-head rate of 0.05 mm/min and a strain gauge was used to measure strain in the gauge length of the sample.

Interlaminar and in-plane shear testing

In order to understand the mechanisms in monotonic flexure for both geometries, interlaminar and in-plane shear strength data for both composites were obtained from Lara-Curzio and Chawla (56). Double notched specimens were used for interlaminar shear testing. Specimens were notched with a thin diamond blade. In-plane shear strengths were obtained from V-notched specimens using the modified Iosipescu geometry for shear testing (28). A schematic of the specimen dimensions and testing configurations for interlaminar and in-plane shear tests is shown in Figs. 14 and 15, respectively.

Modeling using Finite Element Method (FEM)

Finite element method (FEM), using COSMOS™ software by Structural Research and Analysis Corporation, was used to model stress and displacement distributions in the transverse and edge-on orientations. Two approaches were used to model the weak interlaminar shear strength of the laminated composites in this study. In both approaches two isotropic layers were used to simulate the composite. This was not a bad assumption since the plain weave fiber fabric gives isotropy in the 0 and 90° directions. Furthermore, failure by shear can be treated as a macroscopic mechanism between plies, ignoring the microscopicmechanisms involving fiber/matrix interaction. The two isotropic layers were bonded in two ways: (a) by gap elements, which bonded the two surfaces together and were assigned a coefficient of sliding friction, μ, to simulate the extent of sliding; and (b) by a compliant layer, which also bonded

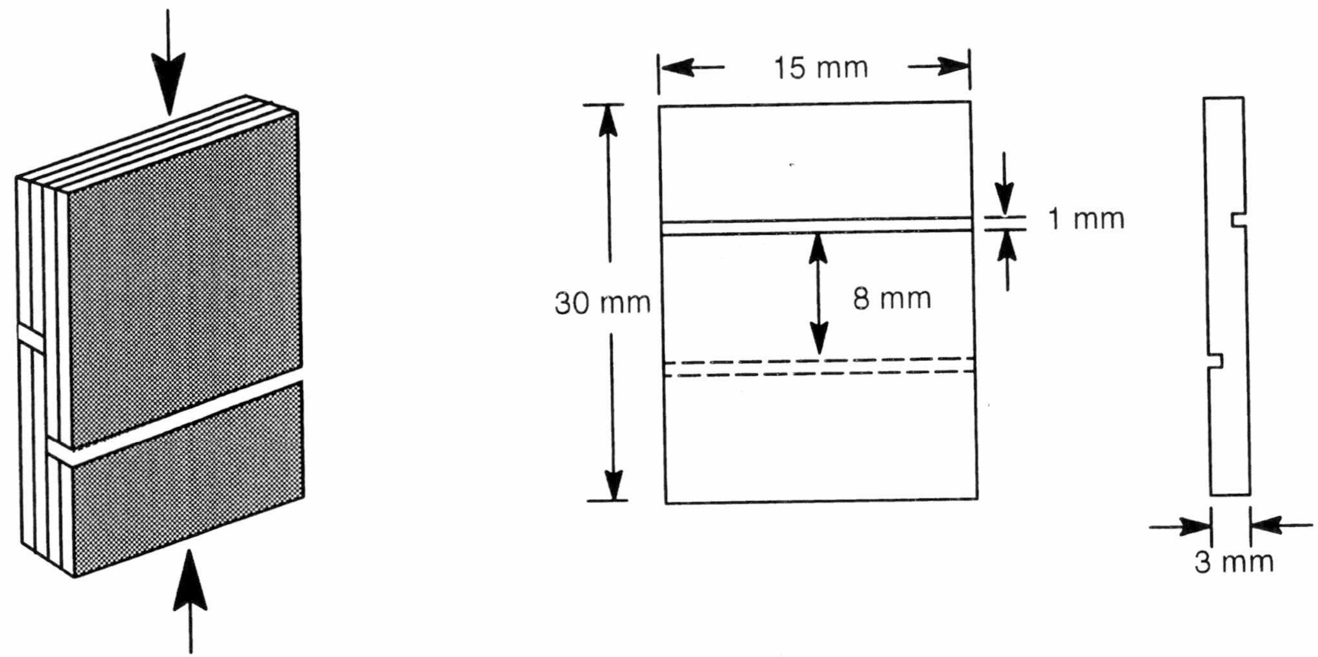

Figure 14. Schematic of specimen dimensions and testing configuration for double-notched interlaminar shear tests (49).

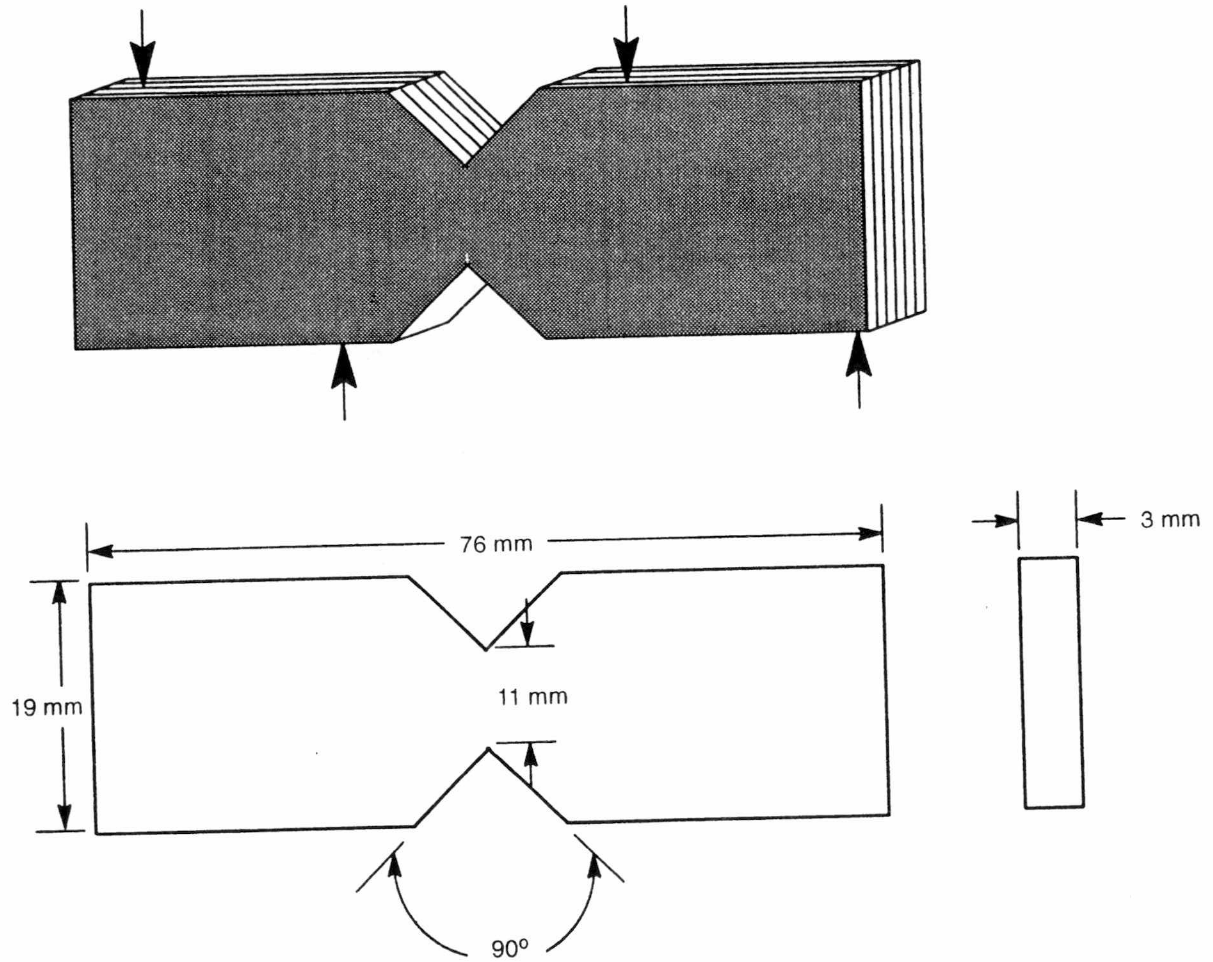

Figure 15. Schematic of specimen dimensions and testing configuration for Iosipescu in-plane shear tests (49).

the two surfaces together but was assigned different moduli values to simulate decreasing resistance to shear in the beam.

The layered material had the same dimensions of a tested flexure bar and was subjected to loading in three-point bending. Analysis in three-point bend was easier in terms of ease of calculations and analysis time. Furthermore, limited experiments in four-point bend showed little difference in results.

Since two orthogonal planes of symmetry were present, Fig. 16, only one fourth of the bar needed to be modeled. PLANE2D elements were used, giving us a two dimensional problem, although the thickness of the beam was also taken into consideration in the analysis. The displacement of the support under the bar was constrained with respect to the y-axis and at the plane of symmetry, the displacement was constrained with respect to the x-axis.

The modulus of the composite was taken as 100 GPa with a Poisson ratio of 0.3. This was a good approximation since a modulus of about 120 GPa was obtained from a tensile test of the Nextel/SiC composite, and since modulus of the composite depends on a variety of factors such as matrix volume infiltrated, fiber architecture, and ply stacking sequence. The "round" value of 100 GPa was also used to simplify and verify FEM calculations.

A 100 N load was applied at the plane of symmetry, to simulate three point bending, and results were normalized by stresses in a simple isotropic beam under the same loading conditions and displacement constraints.

In the gap element analysis a soft truss element with a stiffness of 10 Pa was placed under the beam, to provide stability to the structure. The analysis was conducted using the NONLINEAR module of COSMOS. Loading was applied in five time increments of one second each (i.e., the maximum load was achieved in five seconds and five iterations were done before reaching this point). Axial

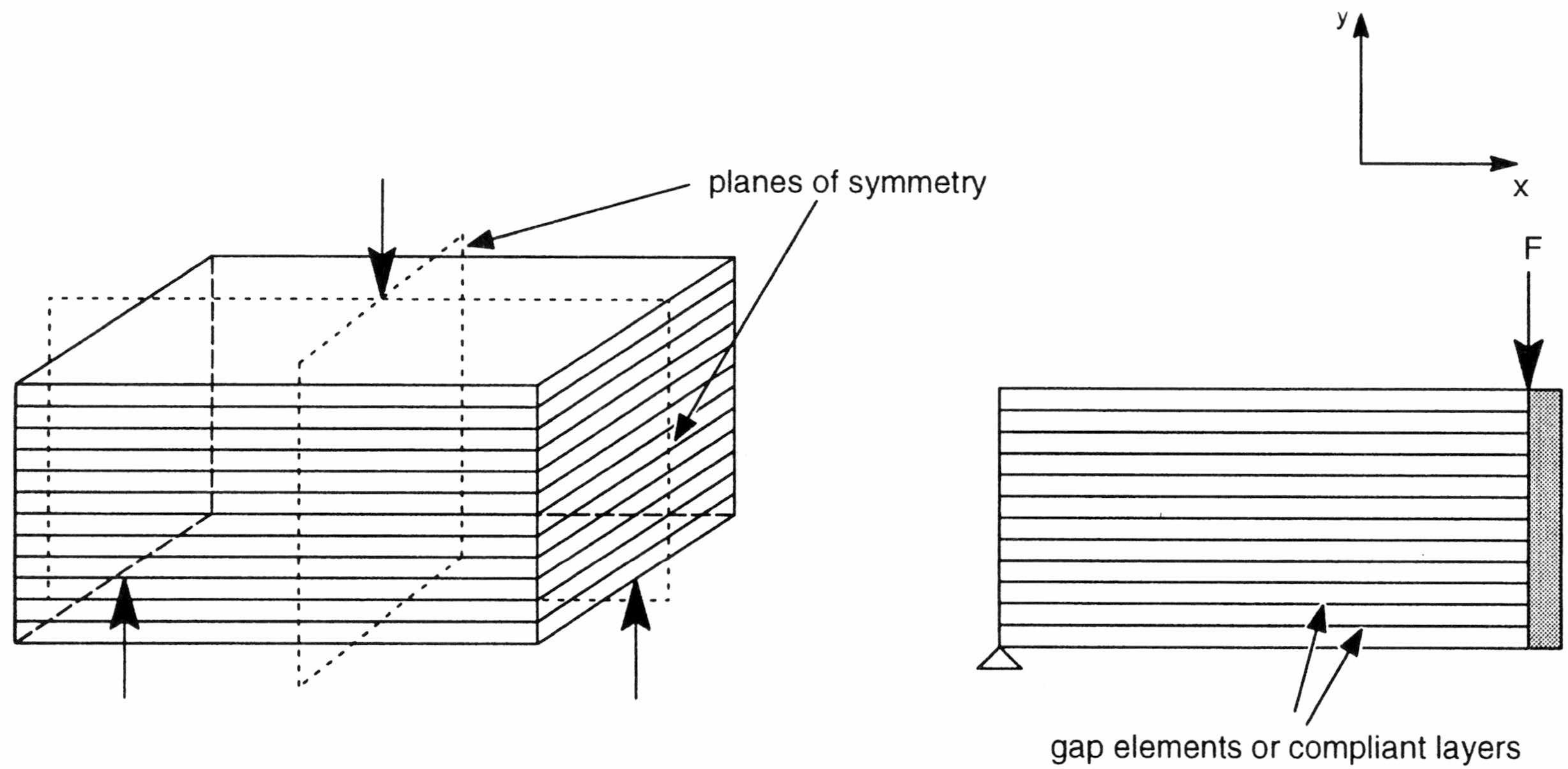

Real problem

Finite Element Model

Figure 16. Schematic of real problem and finite element model using two orthogonal planes of symmetry.

stresses and displacements (σ_x and u_x) as well as stresses in the y direction (σ_y) were plotted, and, using the output file provided by COSMOS, normalized stress and displacement profiles were obtained at coefficients of friction of 0.01, 0.1, 0.5, and 0.99. A coefficient of friction of 0 indicates no bonding between plies or complete sliding. To further substantiate the analysis by Steif (32-34), in the transverse orientation, the above analysis was conducted at four different spans, giving four aspect ratios (ratio of span to height of the beam) of 6.67, 5, 3.33, and 1.67. Since FEM is directly related to the degree of refinement of the mesh as well as other factors, the analysis was conducted at varying number of regular elements, gap elements, stiffness of soft truss, and gap thickness until the solutions converged to a single value. Convergence plots are shown in Appendix A. The analysis was conducted at the converged values shown in these plots.

The effect of friction on the edge-on orientation was also investigated. SHELL4 elements were used with a prescribed thickness and the two layers were also bonded by gap elements, but in this case loading was applied to each ply.

In the compliant layer analysis five stiffnesses, 50, 10, 5, 1, and 0.5 GPa, were assigned to the compliant layer to simulate the inherent weakness between plies in the composite. In this case, an analytical solution was also obtained from mechanics of materials, to corroborate the FEM results. In both, the analytical and FEM compliant layer analysis, it was assumed that the layers were perfectly bonded. This was not the case in the gap element analysis, since coefficients of friction were used to determine the extent of sliding.

As described above, the analytical solution for two layers with modulus E_1 and an intermediate compliant layer of modulus E_2, was obtained from mechanics of materials. It was assumed that the layers with stiffness E_1 were perfectly bonded to an intermediate layer of stiffness E_2, such that $E_1 = E_2/2$, for example. It is convenient to model the intermediate layer as the stiffer material of half thickness. Then, the stress distribution to be calculated was that of an isotropic I-beam, Fig. 17. We can now used the equations relating axial stress and moment in a beam in three-point bend to calculate the stress distribution at a given point from the neutral axis:

$$\sigma = \frac{My}{I}, \text{ and } I = \frac{1}{12bh^3}$$

where σ is the axial stress at a given moment M, y is the distance from the neutral axis, and I is the moment of inertia which was computed from b and h, the base and height of the rectangular element.

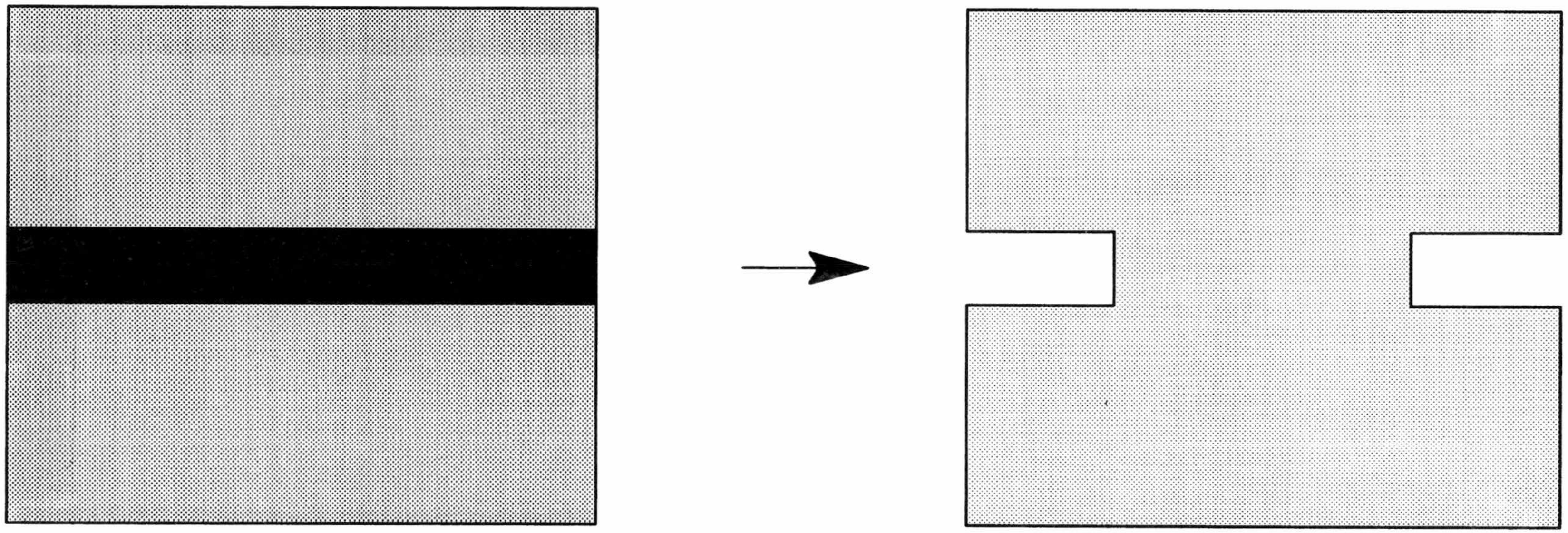

Figure 17. Analytical solution for compliant layer analysis with two layers with modulus E_1 and an intermediate layer of modulus E_2, modeled as an isotropic I-beam of modulus E_1.

CHAPTER IV

RESULTS AND DISCUSSION

DENSITY OF LAMINATES

Overall higher densities were obtained in Nextel/SiC composite compared to Nicalon/SiC. In Nextel/SiC composite, overall density was highest at the bottom of the plate, where the reactant gases entered the preform during infiltration. The top layer was slightly less dense than the bottom, but it was denser than the middle of the plate. This is in contrast with observed results of smaller, denser preforms infiltrated by FCVI, which show the densest layer at the top and the least dense layer at the bottom (57). One could speculate that the density was highest in the center of the plate because of more holes in the graphite holder which allowed a higher fraction of the reactant gases to come into contact with the fibrous preform. Gradients in density through the thickness of the plate in the Nicalon reinforced SiC composite were not observed because of the relatively small infiltration thickness. Overall densities were 85-90% in Nextel/SiC and 70-75% in Nicalon/SiC. The lower densities in Nicalon/SiC can be attributed to high reactant gas pressure, which, while reducing infiltration time, caused the matrix to infiltrate as an overcoat of the fiber bundle, instead of within the bundle.

The laminate stacking sequence of the Nextel/SiC composite was also more beneficial for infiltration. Recall that the Nextel plain-weave cloth was stacked in increasing 30° increments, so that the fibers were arranged in [0/90], [30/120], and [60/150], respectively. The Nicalon/SiC composite was stacked with continuous [0/90] layers. The advantage of the Nextel/SiC stacking sequence is that as the reactant gases pass through the holes of a given fabric ply, the gases immediately come into contact with fibers of the next ply because of the rotation scheme. In the Nicalon/SiC composite, the gases that go through the holes in a given ply do so through the thickness of the composite because of the identical stacking sequence in all plies.

MONOTONIC BEHAVIOR

Monotonic loading flexure tests showed differences in the behavior of the two geometries. In the edge-on orientation of the Nextel composite, the proportional limit stress, σ_{pl}, was around 80 MPa and the ultimate stress was about 187 MPa, Fig. 18. The transverse specimen also had a similar σ_{pl} of 80 MPa, but showed a lower ultimate stress at 171 MPa, Fig. 18. Similar results were obtained in the Nicalon composite where both orientations showed σ_{pl} of 150 MPa, but the edge-on orientation ultimate strength was 400 MPa compared to 350 for transverse, Fig. 19. Thus, we can see that the proportional limit is an intrinsic property of the material and not dependent on fabric orientation.

It is important to emphasize that in the composites used in this study, the matrix cracking point was not synonymous with the proportional limit stress. Typically, CVI composites already have small matrix cracks that have originated during processing at pores between plies or within the fiber bundle. When a saturation of matrix cracks occurs during testing, the load is primarily taken up by the fibers and mechanisms such as crack deflection and debonding at the fiber/matrix interface begin to take place. Consequently, a significant deviation in the curve, the proportional limit, is observed. It follows, then, that

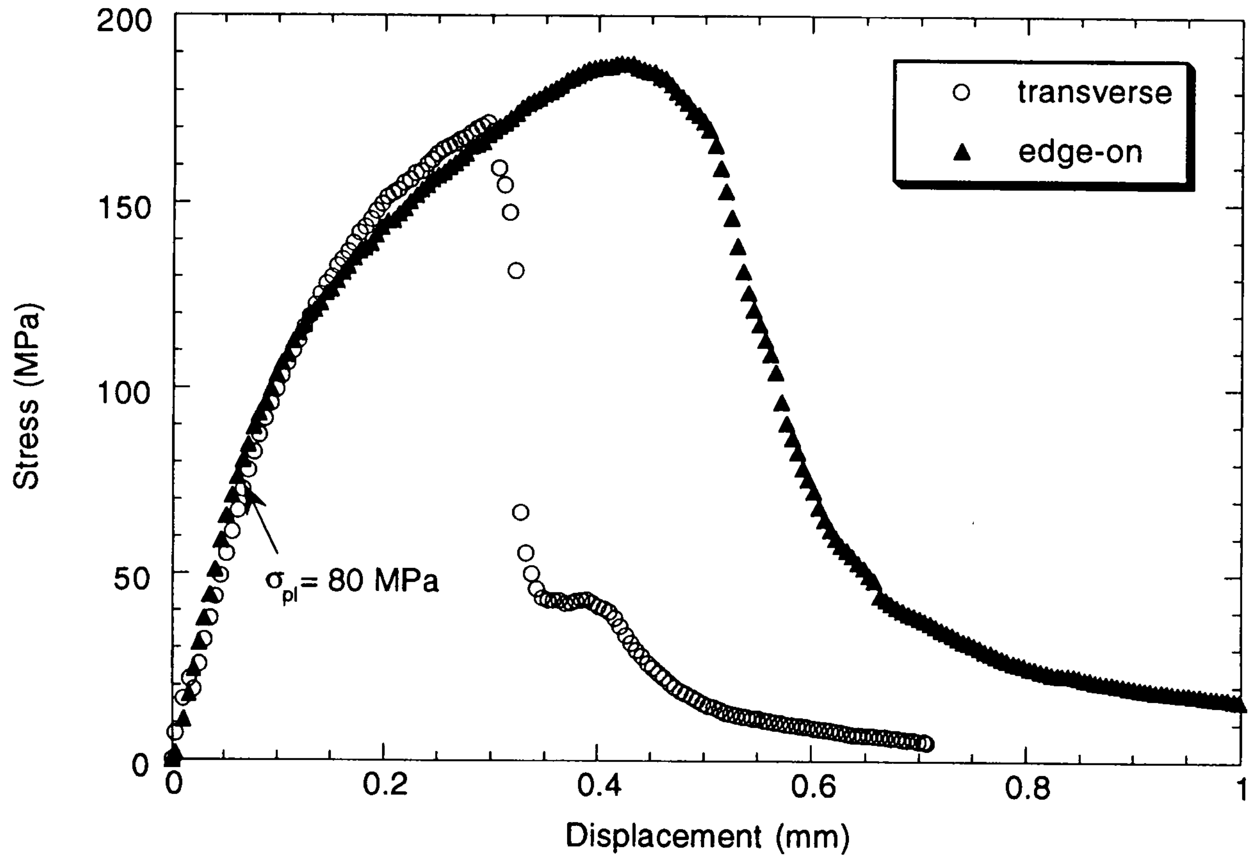

Figure 18. Comparison of stress versus displacement plots in four-point flexure of specimens in transverse and edge-on orientations of Nextel/SiC composite.

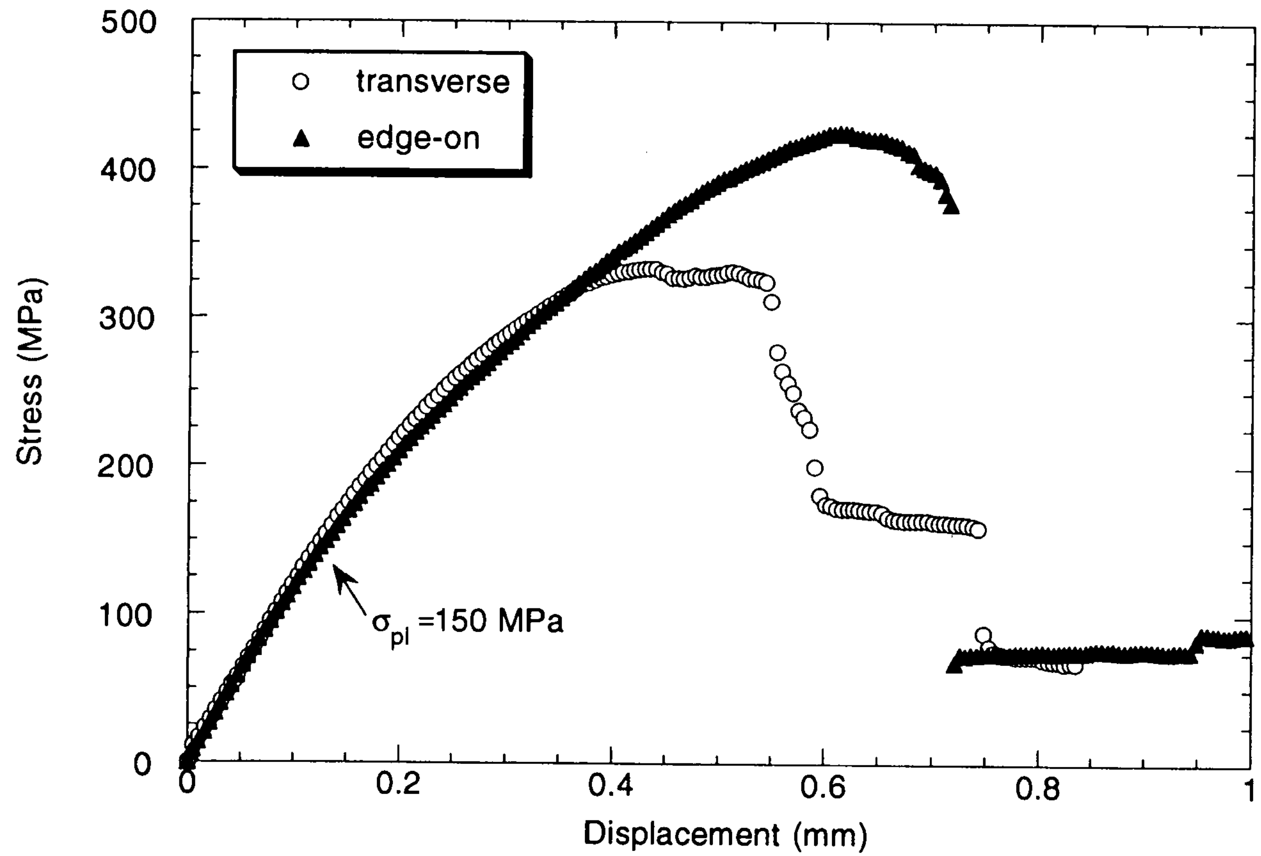

Figure 19. Comparison of stress versus displacement plots in four-point flexure of specimens in transverse and edge-on orientations of Nicalon/SiC composite.

because mechanisms responsible for the differences in strength and toughness in the two orientations occur after the proportional limit, the proportional limit should not be affected by orientation.

Average ultimate strengths in the Nextel/SiC composite were 169.8±18.04 MPa for edge-on and 153.5±17.22 MPa for transverse. In the Nicalon/SiC composite, average ultimate strengths for edge-on were 330±50 MPa and 300±18 MPa for transverse. The overall higher strengths obtained in both orientations of Nicalon/SiC over Nextel/SiC composite were due to the much higher strength of Nicalon fiber, even though the amount of matrix in the Nextel/SiC composite was higher. The nominal fiber volume fraction in both composites was identical.

The curves presented above could only be obtained in tests under displacement control. In displacement control tests, a certain displacement rate is prescribed, so the displacement of the specimen is linear with time and load is directly dependent on the response of the specimen. Therefore, if matrix cracking takes place, or at the proportional limit, a distinct change in the compliance of the specimen can be observed. Fiber debonding and crack deflection mechanisms are allowed to take place, and the tail portion that is normally associated with fiber pullout is also observed.

In load control tests a loading rate is prescribed, so the loading profile is directly linear with time. A load versus displacement curve would be linear to failure because the load is not dependent on the response of the specimen, and subcritical damage mechanisms are inhibited. Fiber pullout would still occur in load control, albeit not as much as in displacement control, but the familiar tail portion observed in the load displacement curve would not be observed.

The work of fracture (WOF), a measurement of the energy needed for failure of the composite and therefore a toughness parameter in these materials, is also dependent on testing mode. In all tests, WOF was calculated as the area under the curve up to the ultimate strength of the composite. The reason the tail portion of the test, associated with fiber pullout, was not considered in the calculation is as follows. The tail portion in displacement control is an artifact of the test, that is, if the test were to be conducted in load control, a steep drop would occur at the ultimate stress and no tail portion would be observed. Therefore, to be consistent, the work of fracture was calculated in this work would be the same in displacement or load control.

Following the above method for calculating WOF, it was determined that the edge-on specimens of both composites had much higher WOF than transverse specimens. This trend indicated that the edge-on orientation was tougher compared to the transverse orientation.

An investigation of the fractured bars showed evidence of the failure mechanisms involved in the two geometries tested, and the reason for increased toughness observed in the edge-on orientation. In the transverse specimen, the incoming crack was arrested and branched at a particular ply due to interlaminar shear between individual plies. It is believed that crack bifurcation by interlaminar shear was further enhanced by void coalescence that formed a compliant layer between plies. This behavior served as a key parameter in FEM analysis, described later.

In the edge-on orientation, failure was not by interlaminar shear, but by in-plane shearing of the fiber fabric. Since in this case the applied stress was distributed over the individual plies, in-plane shear occurred in the fabric cloth, more load was transferred to the fibers, and higher toughening was obtained. This behavior was observed in both composites.

The mechanisms of interlaminar and in-plane shear can be further illustrated by the following example. Consider a set of glass slides, that act as composite laminae, but are not bonded to each other. If the slides are stacked in the transverse orientation, during bending the layers will slide with respect to each other because there is not bonding between the slides. In the edge-on orientation, one has to induce enough energy to break each slide simultaneously. More importantly, it does not matter whether the glass slides are bonded to each other or not, in this orientation, because load is applied to each layer simultaneously and every slide has to be fractured for the entire structure to fail.

SEM of the Nextel composite provided further insight into the underlying failure mechanisms. The fracture surface of the transverse specimen showed large gaps between plies due to the interlaminar shear and void coalescence that occurred during failure, Fig. 20(a). The edge-on orientation did not show such gaps between plies although the in-plane shear could be seen in the form of protrusions of the fibers from the matrix, Fig. 20(b). In the tensile portion of the bend bar (bottom of figure), substantial fiber pullout was observed, but the degree of pullout decreased from the tensile to the compressive section of the bar (top of figure).

Both orientations exhibited tough behavior due to the weak interface provided by the carbon interlayer between fiber and matrix, which resulted in substantial fiber pullout in the composite. Figure 21 shows the carbon coating on the fiber left after pullout as well as impressions of fiber locations before failure in the Nextel/SiC composite. Overall less fiber pullout was observed in the Nicalon/SiC

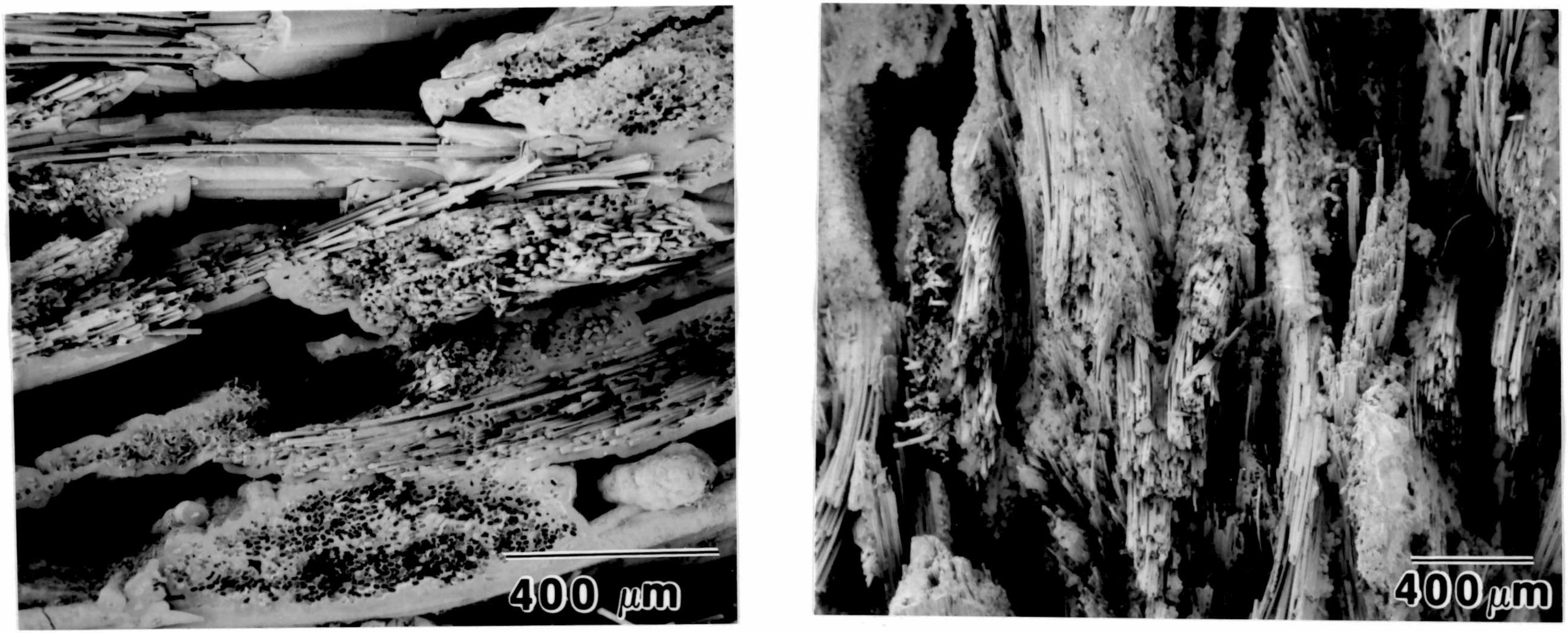

(a) (b)

Figure 20. Comparison of SEM micrographs of fracture surfaces in Nextel/SiC composite: (a) transverse - large gaps between plies due to interlaminar shear, and (b) edge-on - in-plane shear in fiber fabric by predominant pullout from tensile section to comparatively less pullout in compressive section of bar.

(a)

(b)

Figure 21. SEM micrographs of fiber pullout in Nextel 312/SiC composite: (a) carbon coating of fiber left in matrix after pullout, and (b) fiber impressions in matrix after pullout.

composite because with [0/90] orientation of each ply, only half of the fibers in the longitudinal direction (0°), or 50% of the total fibers, were taking up tensile stresses in the beam. In the Nextel composite, fibers in the [0/90], [30/120], and [60/150], took some if not all of the applied stresses. Nevertheless, the pyrolitic graphite coating in both composites provided a weak enough interface that was conducive to toughening.

As expected, tensile tests of Nextel/SiC yielded substantially lower strengths compared to bending tests. The stress-strain curve from the tensile test of the Nextel composite is plotted in Fig. 22. Final failure occurred at 87 MPa and 0.3% strain. Pore bridging by fiber bundles as well as delamination between plies were observed. Furthermore, void coalescence and void growth along the ply interface was also present. These mechanisms resulted in a fairly tough composite, although it should be pointed out that due to the high porosity in this material and the low strength of Nextel 312 fibers, a greater increase in strength above the proportional limit was not observed.

The predominant reason for fiber failure in both composite seemed to be surface or internal flaws, a result of fiber processing, see Fig. 23. The resultant fracture can be qualified as mirror-mist-hackle type. The mirror region was the shiny locus of fracture, followed by a mist-like region and the hackle region where accelerated failure occurred in the fiber. Such fracture is commonly observed in glasses and other brittle ceramics (58-60). These flaws act as stress concentrators and leave the fiber susceptible to premature failure.

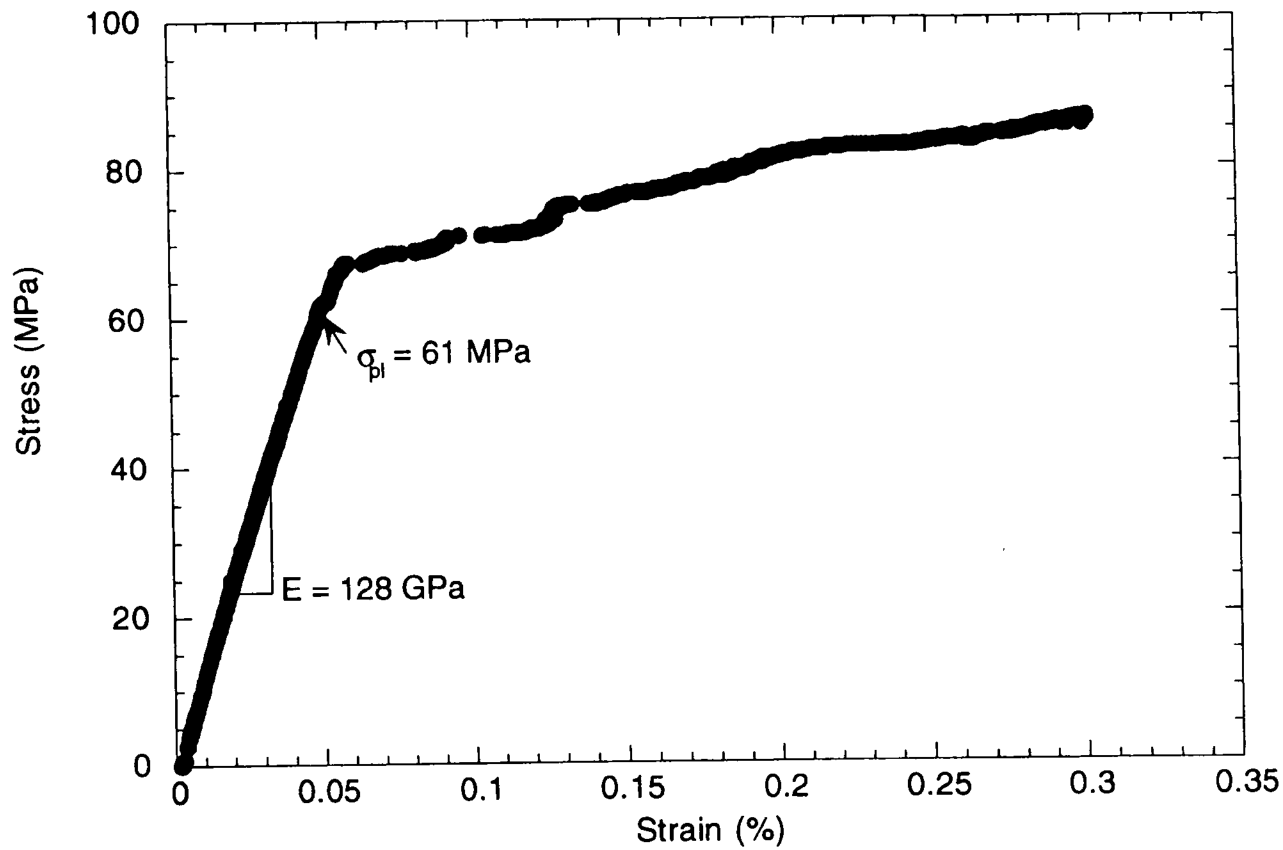

Figure 22. Stress-strain curve from a typical tensile test of Nextel/SiC composite. Notice the distinct proportional limit and much lower strength compared to the flexure strength.

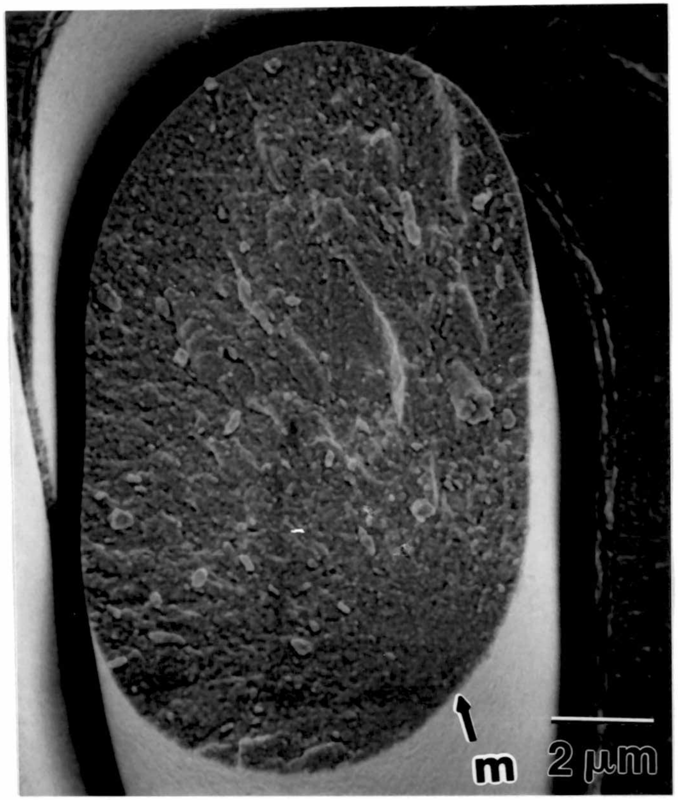

(a)

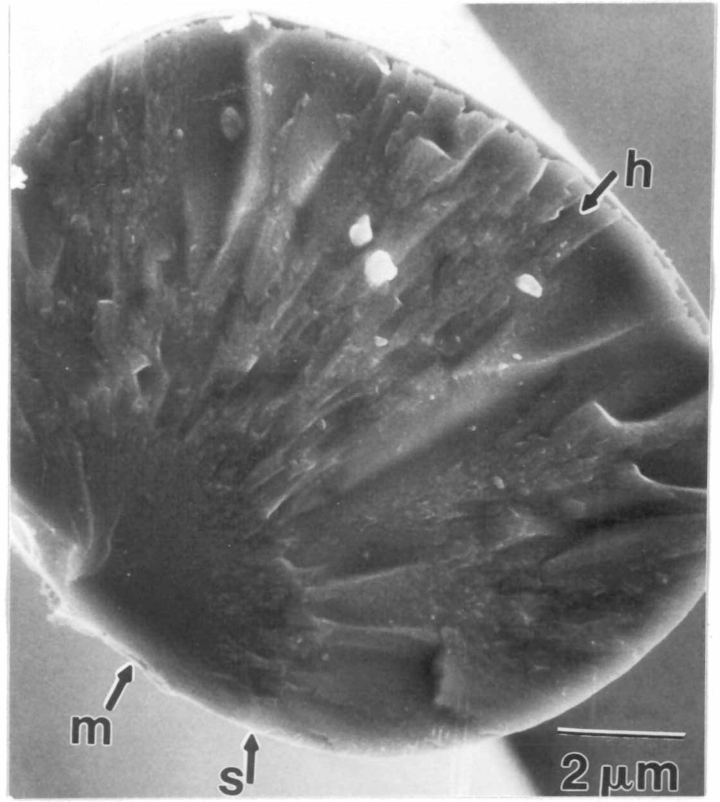

(b)

Figure 23. SEM micrographs of fractured (a) Nextel fiber and (b) Nicalon fiber, showing surface flaws that caused premature failure.

FATIGUE BEHAVIOR

S-N curves for transverse and edge-on orientations, obtained from fatigue tests in four-point bending in load control, were quite different. In the Nextel/SiC composite, both orientations specimens subjected to maximum stresses of 90 and 120 MPa survived 10^5 cycles, while at 150 MPa, close to the ultimate strength, failure occurred in less that 100 cycles, Fig. 24. Although there seems to be a cross-over in the two curves, it is believed that transverse and edge-on specimens fatigued at stress levels of 135 MPa and below had comparable fatigue lives. The mechanisms of the two orientations in fatigue were still quite different. The transverse orientation was much more "flexible" than edge-on specimens, so the plies were allowed to slide with respect to one another due to weak interlaminar shear, and the specimen went through a higher bending displacement without failing. In this particular case, weak interlaminar shear was beneficial because at lower stresses limited sliding allowed energy from the applied load to be dissipated. The magnitude of sliding was not enough, however, for the specimen to fail. Edge-on specimens, on the other hand, being stiffer due to in-plane shear of the fiber fabric, did not undergo a very large displacement compared to transverse specimens, although one obtains similar fatigue lives at lower applied stress levels for both orientations.

In the Nicalon/SiC composite, transverse and edge-on specimens survived 10^5 cycles when subjected to a maximum stress of 200 MPa and below, Fig. 25. At stresses of 220 MPa, transverse specimens failed at a low number of cycles (200-300 cycles), while edge-on specimens survived 10^5 cycles. In the Nicalon composite, because of higher interlaminar porosity, the difference between S-N curves in both orientations was magnified, compared to Nextel/SiC. Transverse

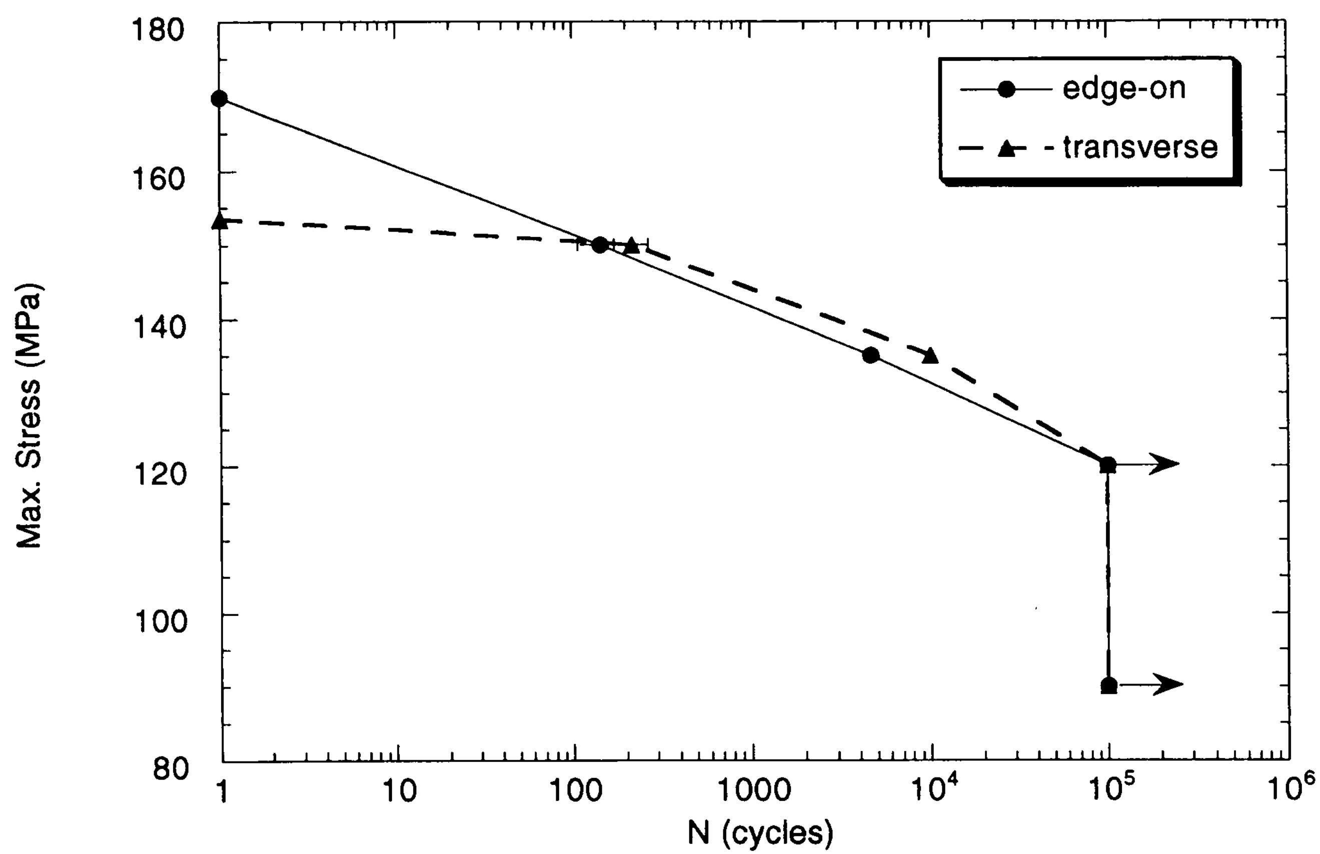

Figure 24. Comparison of S-N curves for transverse and edge-on orientations in Nextel/SiC composite. The transverse curve is concave due to the flexibility of the composite in this direction, caused by weak interlaminar shear between plies. The edge-on curve is linear due to the inherent stiffness of the composite in this direction, caused by strong in-plane shear of the fiber fabric.

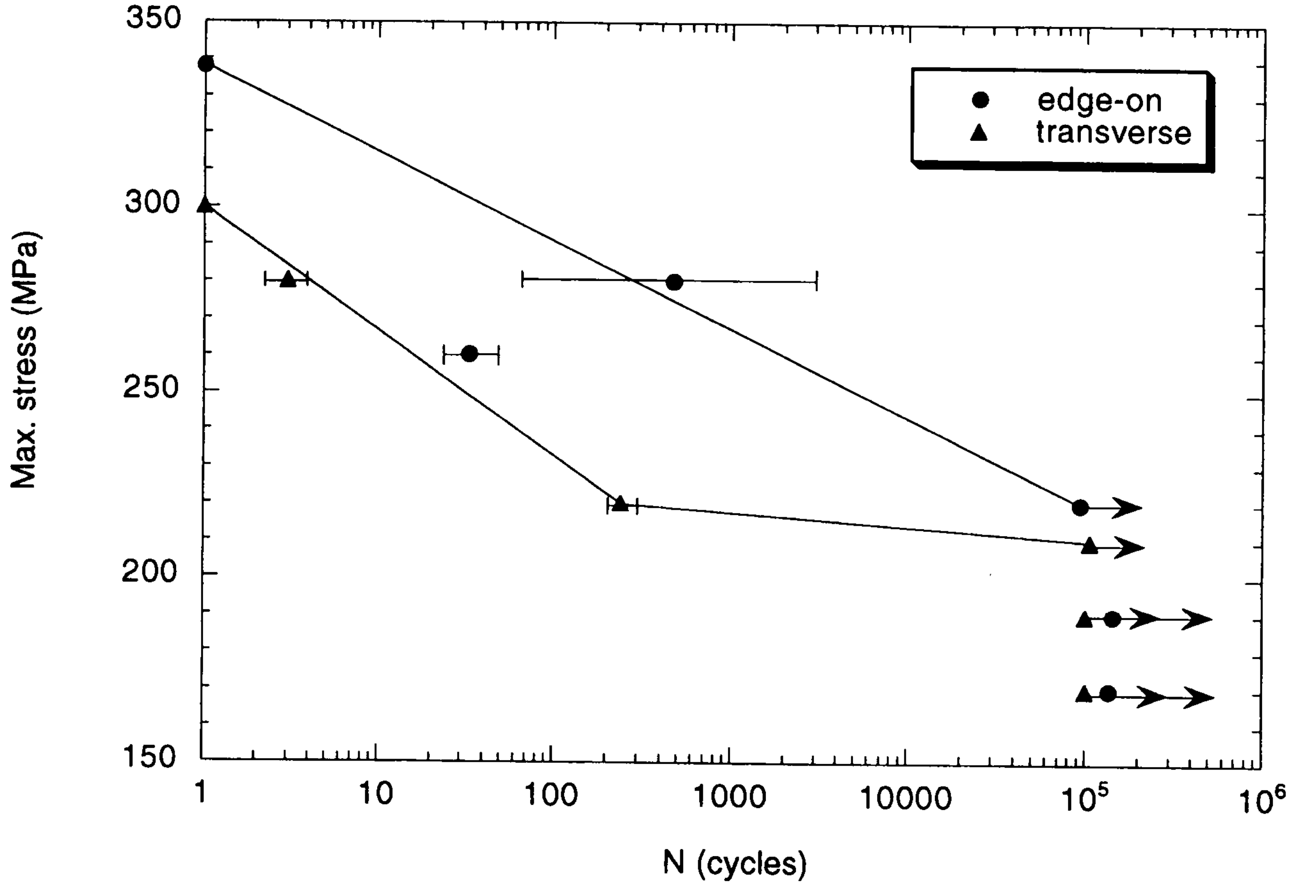

Figure 25. Comparison of S-N curves for transverse and edge-on orientations in Nicalon/SiC composite. The transverse curve is significantly lower than the edge-on curve due to higher porosity and more sliding in the Nicalon/SiC transverse orientation. The edge-on curve is still linear due to the inherently higher stiffness of the composite in this direction.

specimens now failed more prematurely because of an increased magnitude in sliding resulted in failure of the specimen. The edge-on orientation was not greatly affected by the porosity because the fiber fabric took up most of the load through in-plane shear mechanisms described above.

Post-fatigue monotonic flexure tests on specimens that survived 10^5 cycles were helpful in determining fatigue mechanisms in both orientations of the composites. Figure 26 shows a comparison of stress versus displacement curves for an as-received and a fatigued transverse specimen of the Nextel composite that survived 10^5 cycles at a stress amplitude of 90 MPa. Since sliding of the plies occurred during fatigue, the material became more compliant. In the post-fatigue monotonic test, then, sliding of the plies was easier which contributed to a higher work of fracture than that of the as-received material. Figure 27 shows a similar comparison for the edge-on case. In this orientation, the sliding mechanism that dissipated energy in the transverse orientation was not present so more fatigue damage was induced during the test, and the work of fracture was reduced substantially.

In the Nicalon/SiC composite, because of the greater extent of sliding, in addition to more compliant behavior after fatigue, discrete portions of plateau in load after the ultimate strength were observed, Fig. 28. These were caused by sliding, because an increase in displacement is observed but the same load was needed to slide the plies. In the transverse orientation, fatigue damage induced lower strengths because of more compliant behavior.

The edge-on orientation, on the other hand, suffered a significantly higher degradation in strength after fatigue, perhaps due to the absence of "flexibility" due to sliding in transverse specimens, Fig. 29. It should be noted, however,

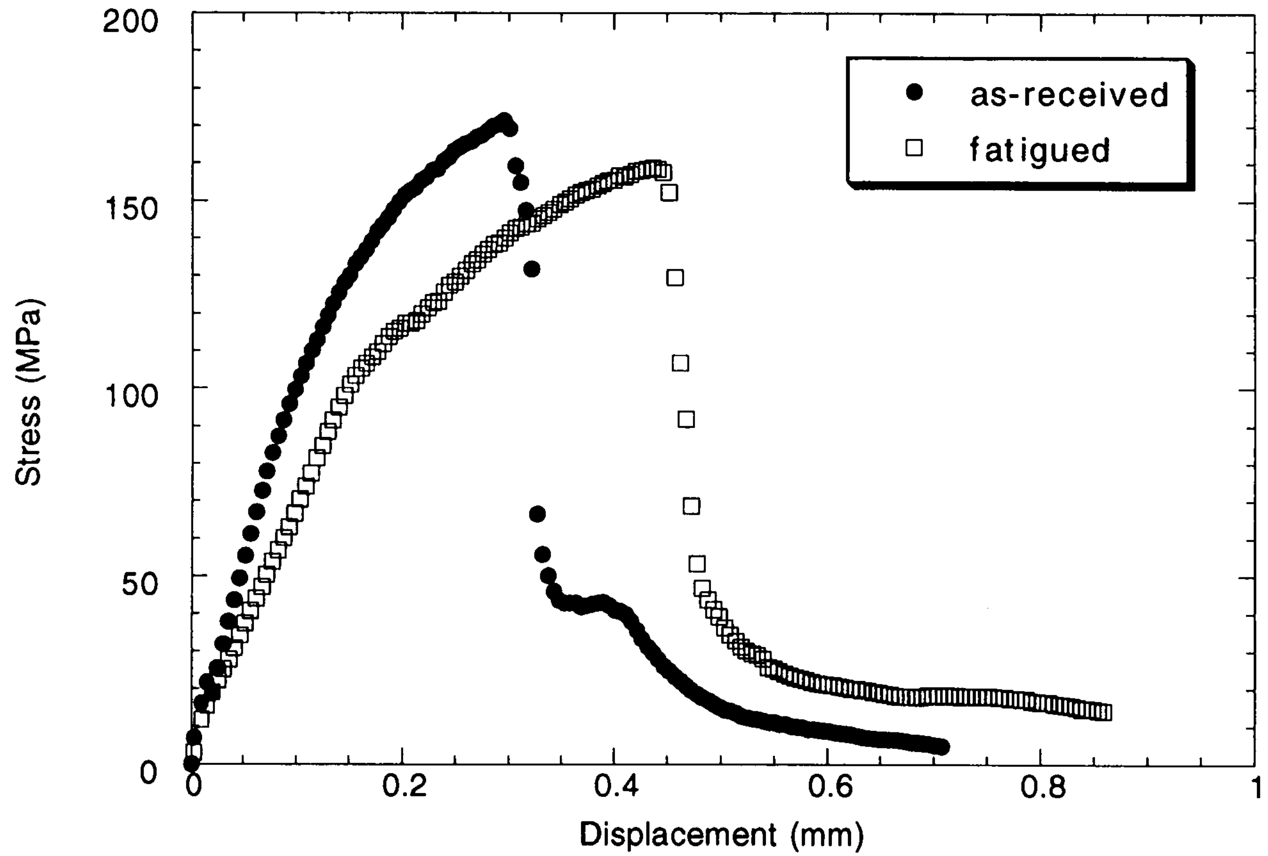

Figure 26. Stress versus displacement curves for transverse specimen of Nextel/SiC composite after 100,000 cycles at a maximum stress of 90 MPa. Notice that the material has become more compliant, while having a higher work of fracture than the as-received case.

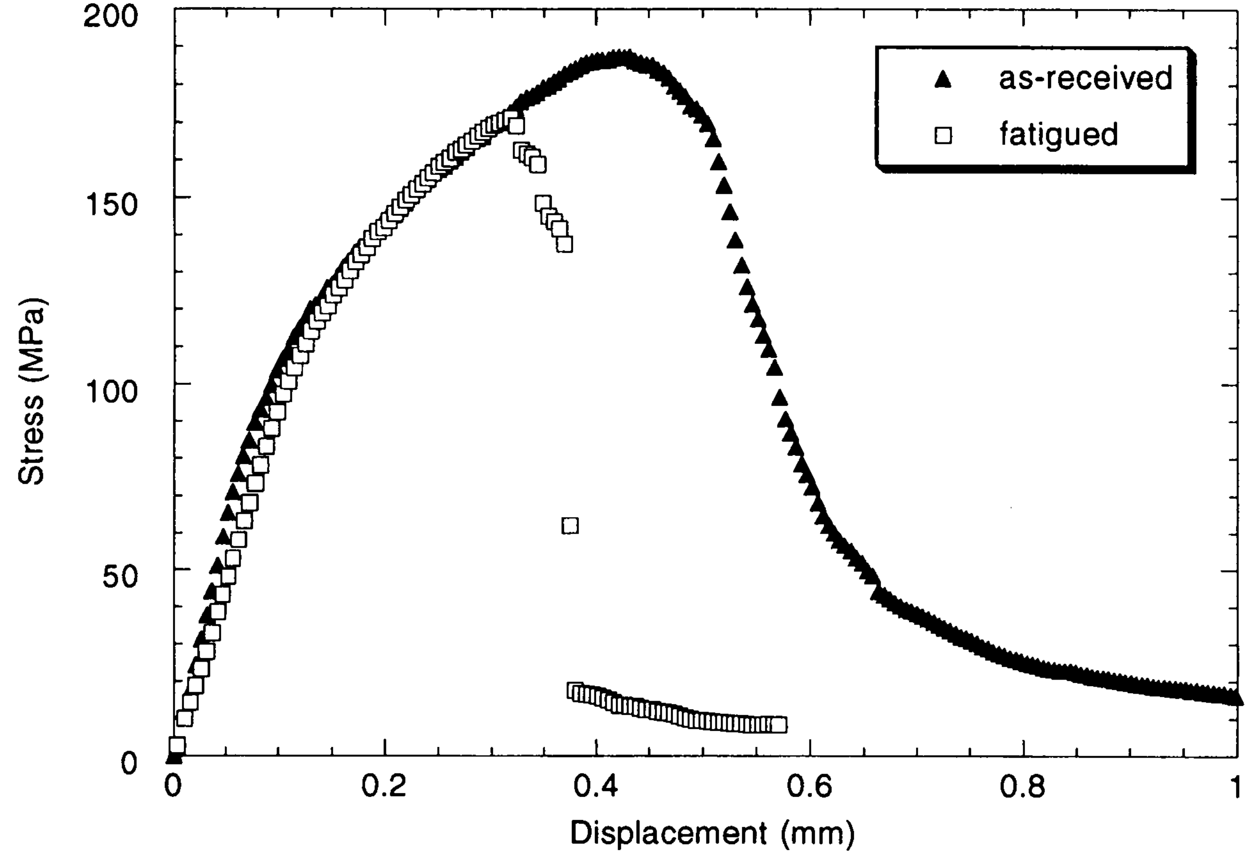

Figure 27. Stress versus displacement curve for an edge-on specimen of Nextel/SiC composite after 100,000 cycles at a maximum stress of 90 MPa. Notice that the work of fracture is reduced, compared to the as-received case.

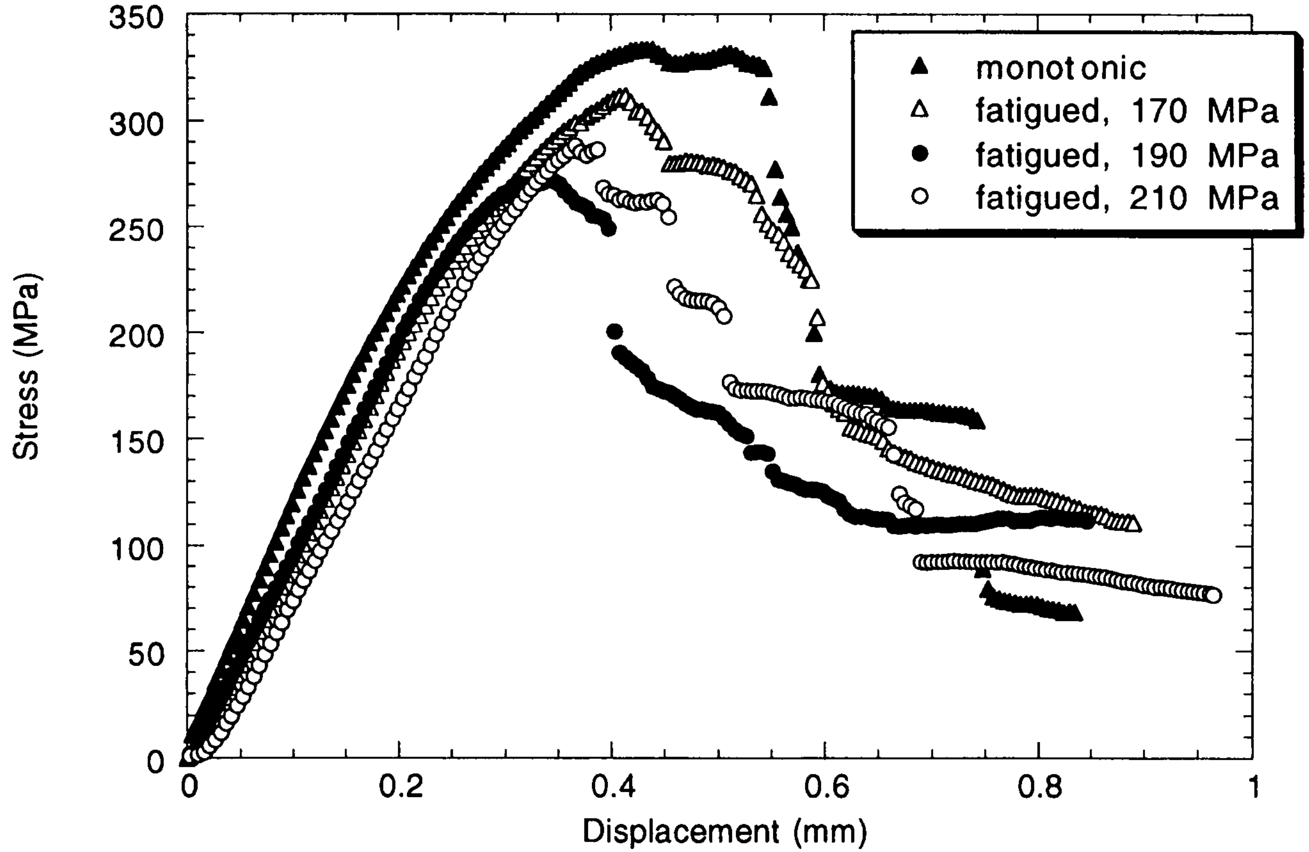

Figure 28. Stress versus displacement curve for transverse specimens of Nicalon/SiC composite after 100,000 cycles at various stress levels. Notice that, in addition to more compliant behavior after fatigue, discrete portions of plateau in the load after the ultimate strength are observed because of significant sliding events.

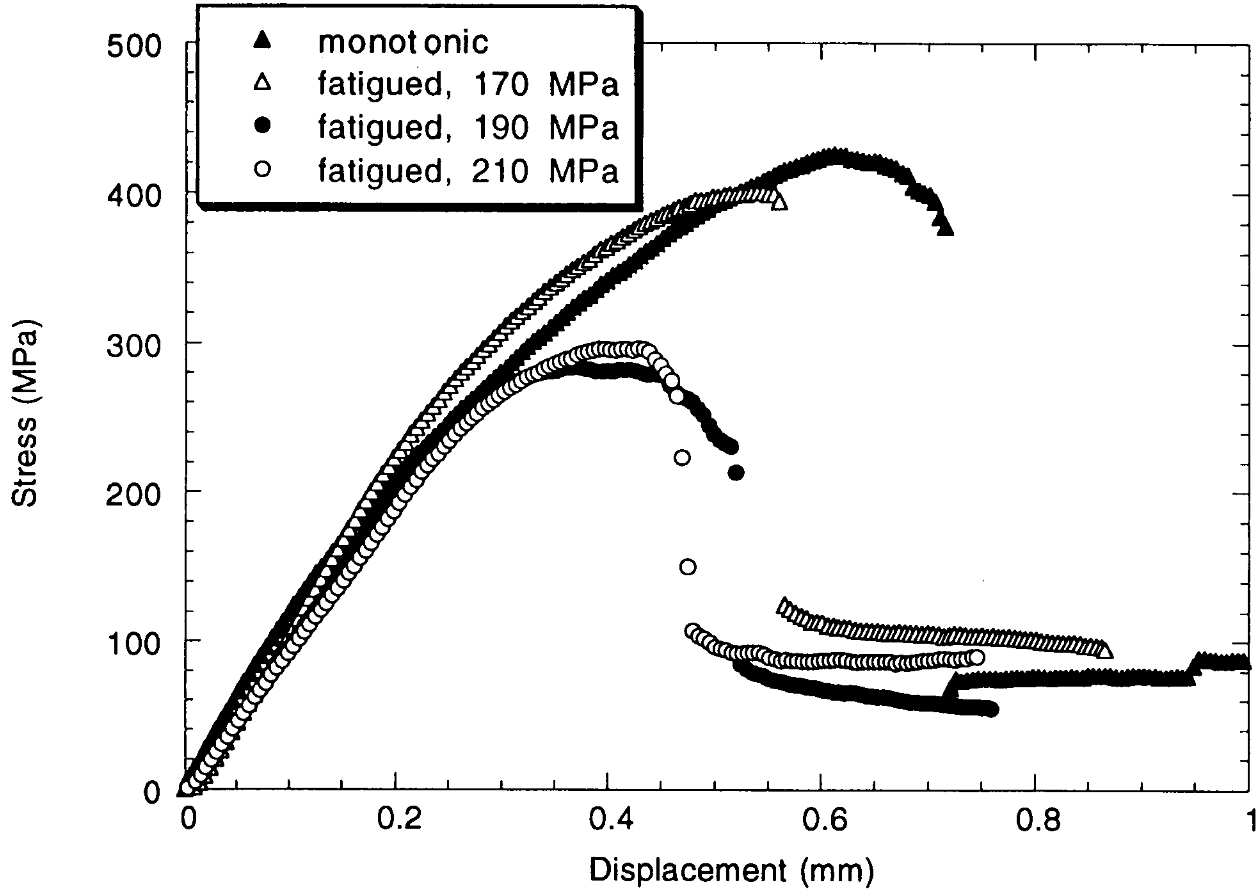

Figure 29. Stress versus displacement curves for edge-on specimens of Nicalon/SiC composite after 100,000 cycles at various stress levels. Fatigue damage induced lower strengths and more compliant behavior, but a significant amount of strength is retained after fatigue.

that although a greater decrease in strength was observed in the edge-on orientation, post-fatigue strength values for edge-on specimens were similar to those for transverse specimens fatigued at a given stress level.

It is interesting to note that in Nicalon/SiC specimens in both orientations, there was no noticeable proportional limit in post-fatigued specimens. This was because when cycling above the proportional limit, the matrix was substantially cracked and the applied load in the post-fatigue test was transferred primarily to the fibers. In Nextel/SiC composites, the curves in Figs. 26 and 27 are from specimens that were cycled very close to the proportional limit, so post-fatigued specimens also show a noticeable proportional limit.

Although there is a significant effect of σ_{pl} on strength, fatigue limits are not dependent on σ_{pl}. S-N curves for these materials showed runout above the proportional limit as well as below, which is not the case in fully-dense glass-ceramic matrix composites. The influence of proportional limit is perhaps more important where significant matrix cracking occurs in a fully dense matrix.

SEM examination revealed the micromechanisms that occurred in fatigue. Figure 30 shows fibers that slid with respect to the matrix during cyclic loading, in both composites. This abrasion between fiber and matrix during fatigue caused degradation of the fiber/matrix interface, leaving no coating between fiber and matrix. An incoming matrix crack after fatigue would propagate straight through the interface and no visible toughening would be obtained after fatigue. Perhaps a thicker coating at the fiber/matrix interface could alleviate this problem, so that degradation during fatigue would only remove part of the coating necessary for a tough composite.

(a)

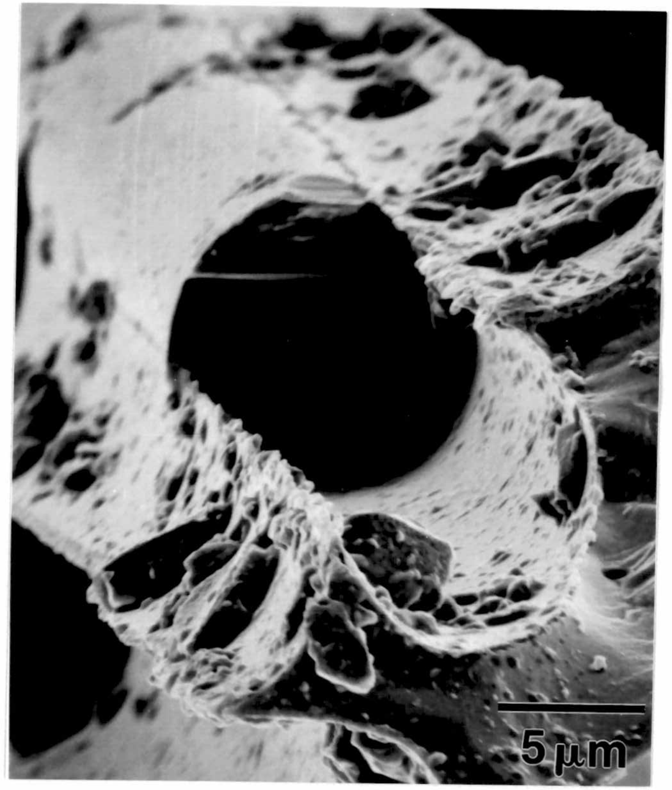

(b)

Figure 30. Fibers that slid with respect to the matrix during cyclic loading, (a) Nextel/SiC composite and (b) Nicalon/SiC composite.

Considerable damage was also observed in both composites, Fig. 31, due to localized matrix cracking at micropores within the fiber bundle. Such small asperities may have fallen between the fiber and matrix and caused further abrasion at the interface. Better infiltration to close micropores would be desirable to avoid such damage.

INTERLAMINAR AND IN-PLANE SHEAR

As expected, data from Lara-Curzio and Chawla (56) showed that interlaminar shear strengths (ILSS) were considerable lower than in-plane shear strengths. Double notched specimens showed higher ILSS for Nextel/SiC over Nicalon/SiC composites, due to the higher density of the former composite. Stress versus displacement curves for both composites showed a gradual ramp to the ultimate strength where failure occurred, Fig. 32. The Nextel/SiC composite had an ILSS of 50 MPa compared to 40 MPa for the Nicalon/SiC material.

Matrix volume fraction was crucial in ILSS. Figure 33 shows a comparison of fracture surfaces of the two composites. In an ILSS test, fracture occurred where each ply was bonded with an adjacent ply. In the Nicalon composite, due to lower densification, less bonding between plies was observed so the fracture surfaces were much "cleaner" that those of the Nextel composite. Notice parts of the matrix that were pulled off by shear, in Fig. 33, exposing the fibers in the bundle in Nextel/SiC.

In-plane shear strengths of the Nextel/SiC were about 140 MPa compared to 100 MPa in Nicalon/SiC. Shear stress versus displacement curves showed a gradual ramp in loading similar to that observed in ILSS tests, Fig. 34. Notice

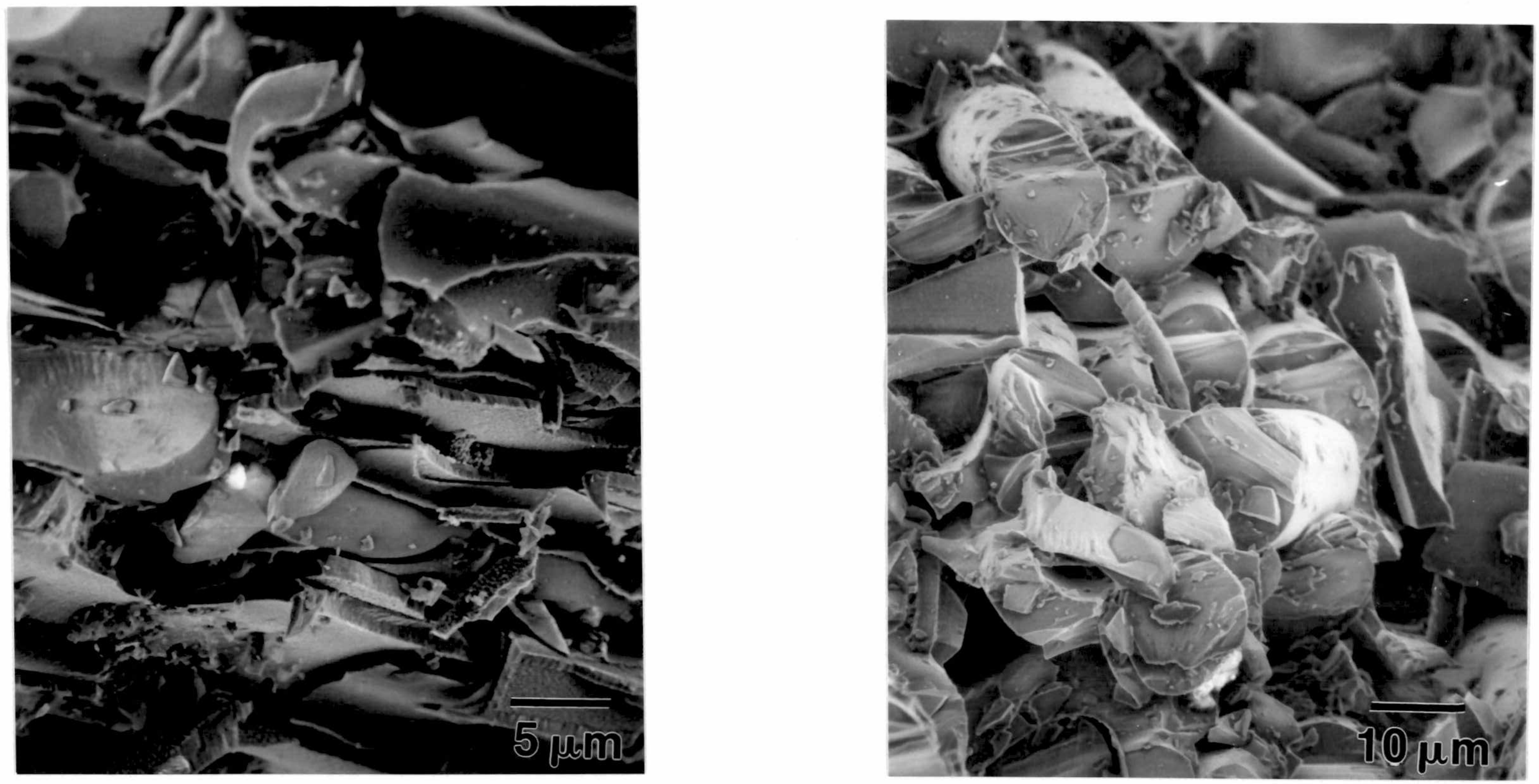

(a) (b)

Figure 31. Considerable fatigue damage in (a) Nextel/SiC composite and (b) Nicalon/SiC composite, due to localized matrx cracking at pores within the fiber bundle.

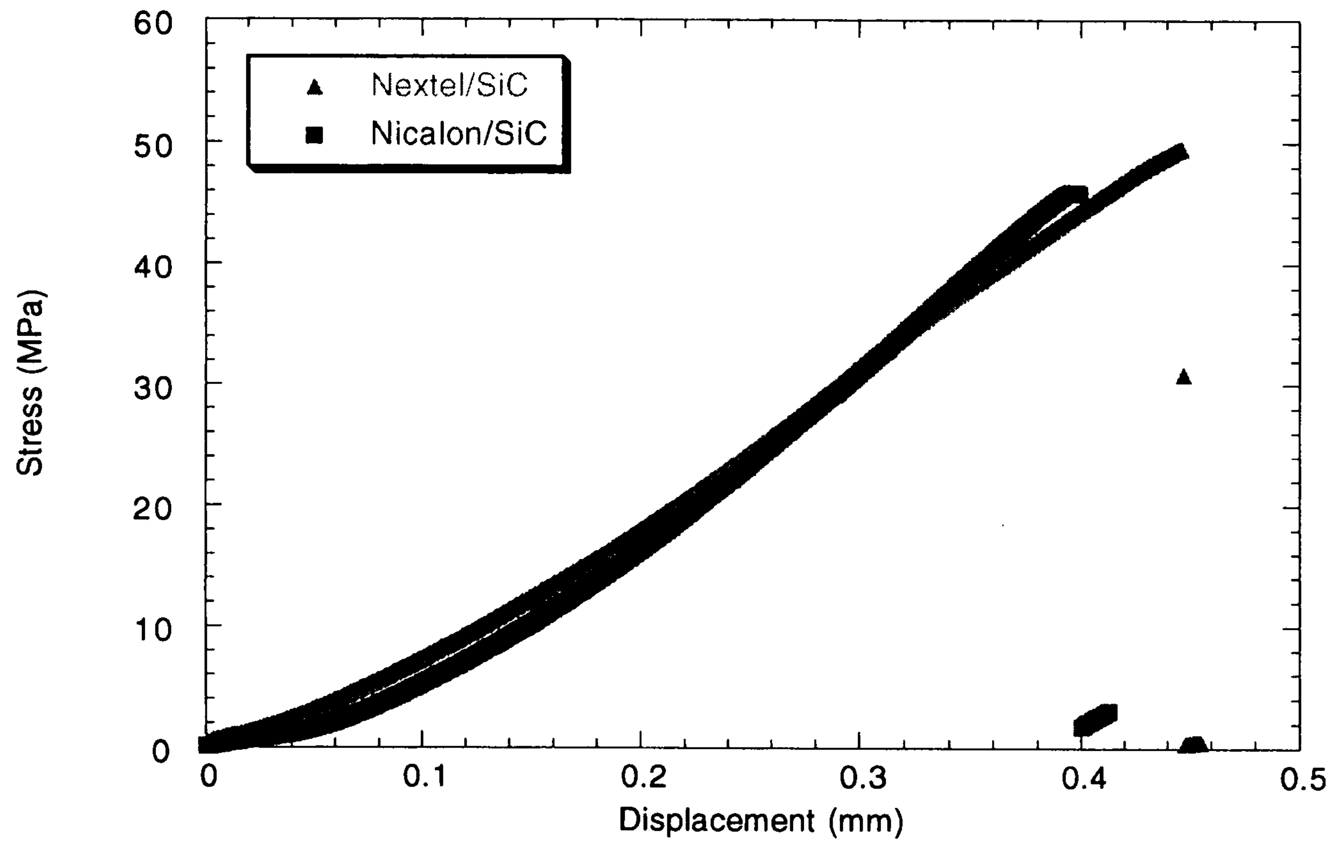

Figure 32. Typical stress versus displacement curves for double notched interlaminar shear tests in Nextel/SiC and Nicalon/SiC composites.

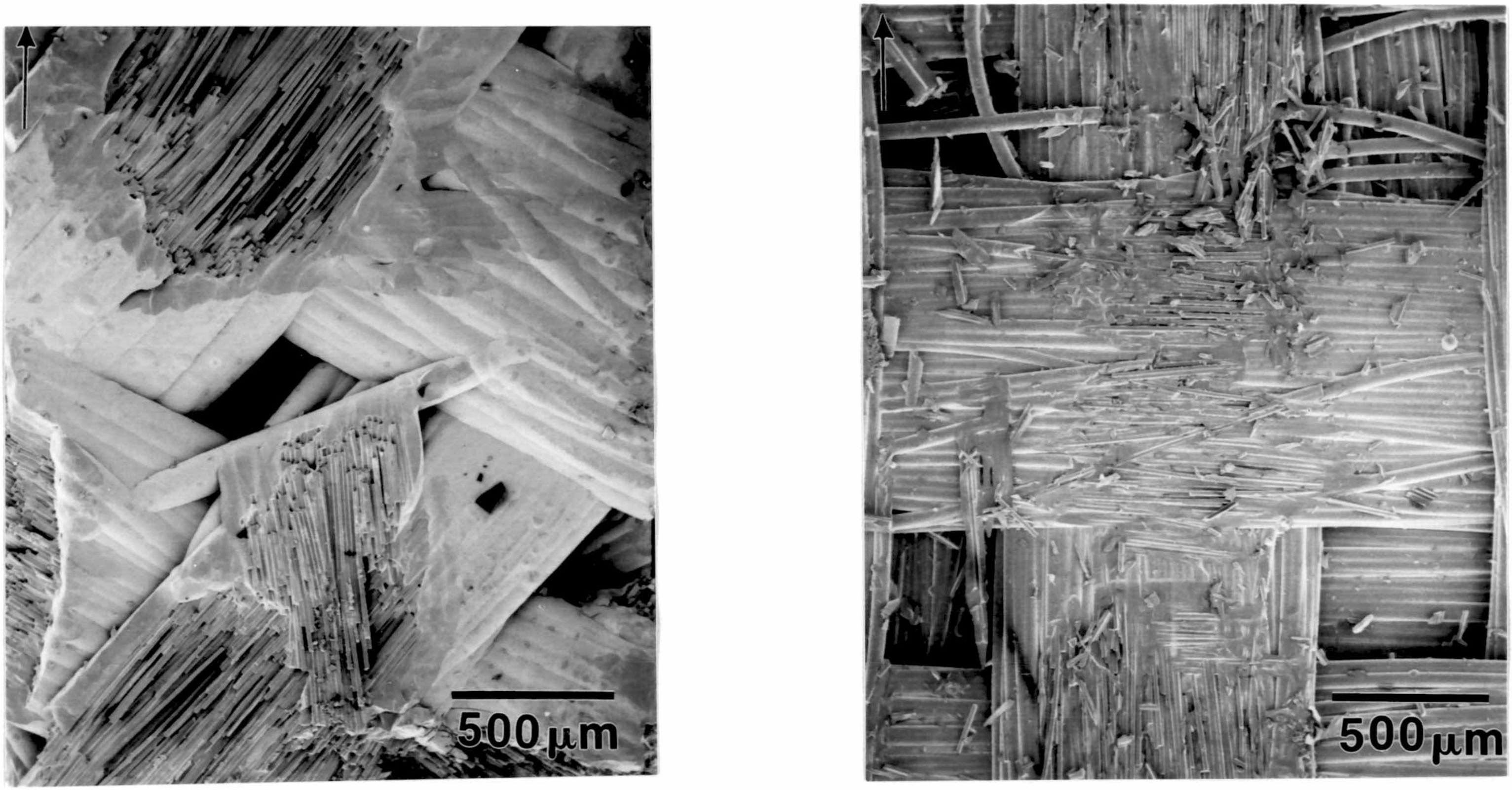

(a) (b)

Figure 33. Comparison of fracture surfaces of the two composites after interlaminar shear tests: (a) Nextel/SiC and (b) Nicalon/SiC. Notice more damage in Nextel/SiC composite due to higher ILSS.

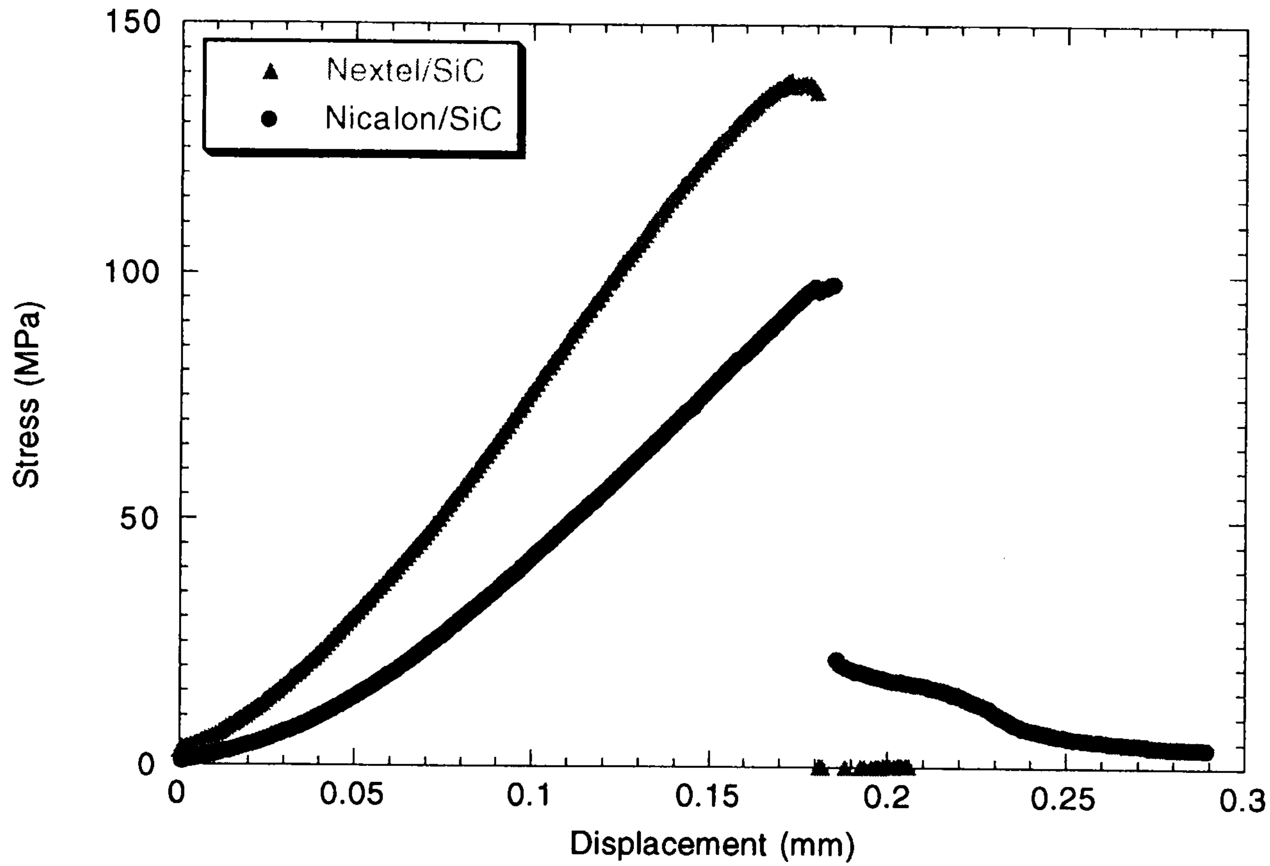

Figure 34. Stress versus displacement curves for Iosipescu in-plane shear tests for both composites.

that due to higher density, the Nextel/SiC composite failed completely, i.e., the load dropped to zero after failure, while the Nicalon/SiC composite curve dropped to about 50 MPa because of bridging of the crack by the Nicalon fiber fabric, which was observed during the test.

It is interesting to note that even with a much lower strength fiber, Nextel/SiC had a higher strength than Nicalon/SiC, indicating that interlaminar and in-plane shear strengths are directly related to matrix volume fraction and not fiber strength in these composites. This correlates with the limited results by Evans et. al (61, 62) who reported that in-plane shear deformation was primarily governed by matrix cracks, since fiber sliding was inhibited in shear loading. In our work, SEM showed this in both composites. Extensive damage, consisting of large sections of matrix being torn from the fiber fabric was observed, Fig. 35. More fiber pullout, which may have also added to higher shear strengths, was observed in the Nextel/SiC than in Nicalon/SiC composite.

FINITE ELEMENT METHOD (FEM)

Compliant layer analysis

The basis for FEM, as described above, was that a more or less continuous porous layer exists between plies in the composites. This is indeed the case, as can be seen in an optical micrograph of a Nicalon/SiC bar, Fig. 36. The fiber bundle is yellow surrounded by white matrix material. The remaining portion in the micrograph is red and constitutes the porosity in the composite.

In the compliant layer analysis, parametric plots were obtained showing the analytical solutions for axial stress distributions in the bar as a function of distance from the neutral axis, at a given stiffness of the compliant layer. FEM

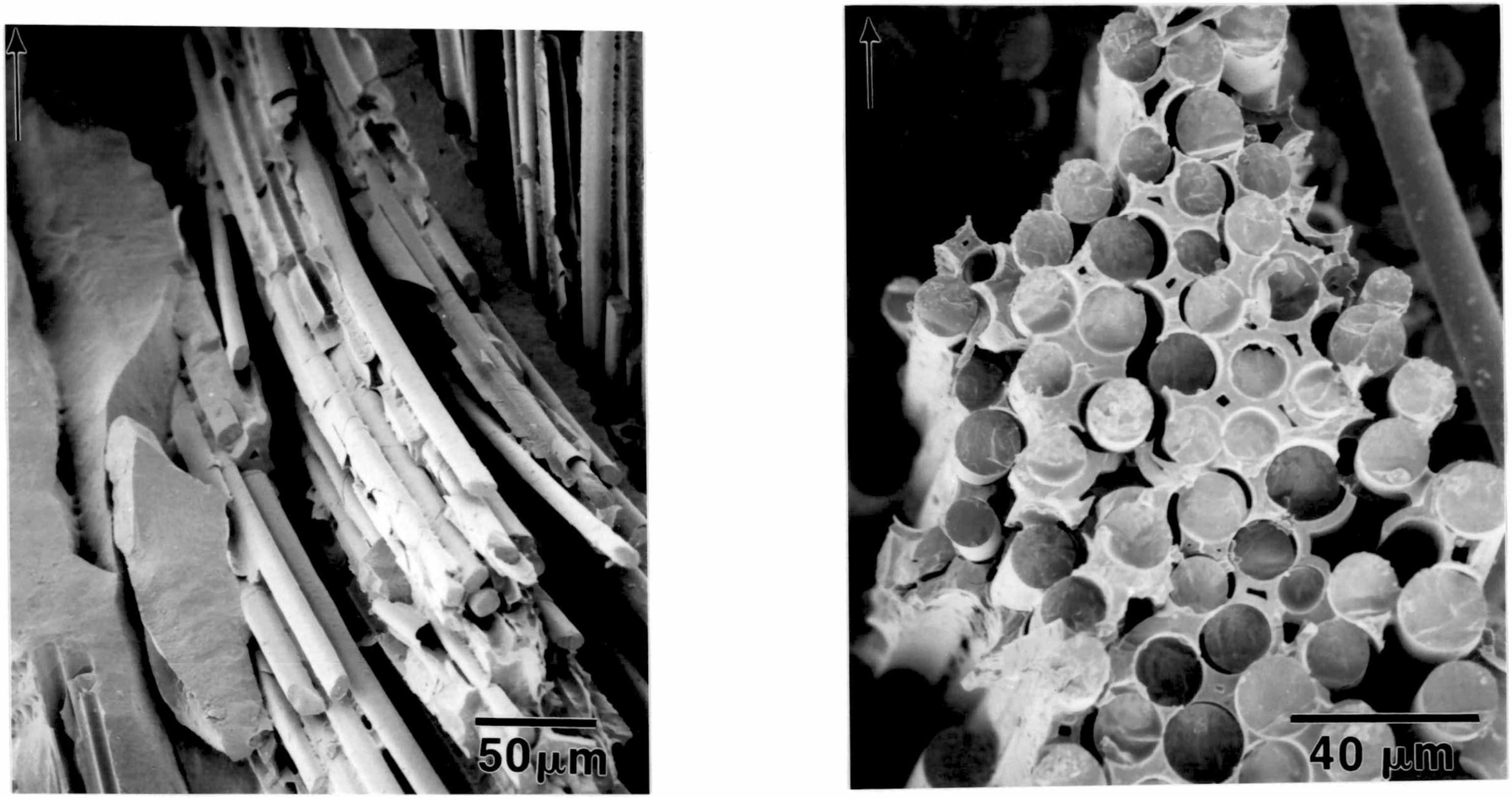

(a) (b)

Figure 35. Scanning electron micrographs of violent damage after in-plane shear tests of both composites (a) Nextel/SiC and (b) Nicalon/SiC.

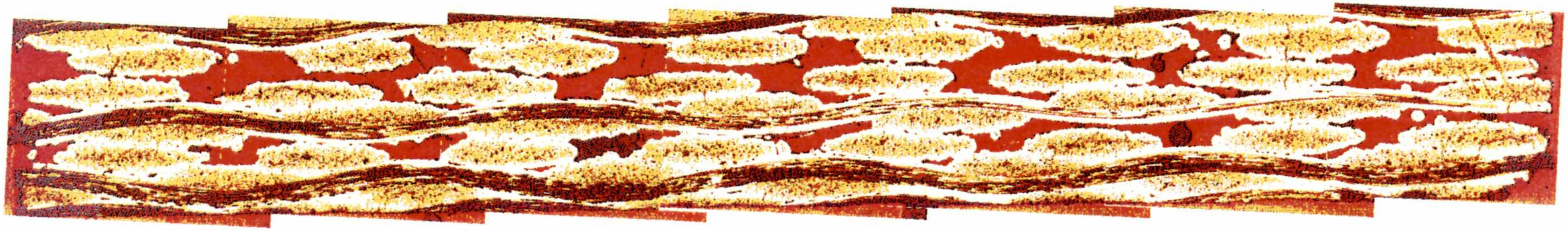

1.5 mm

Nicalon/SiC Composite
BF Goodrich
70-75% theoretical density

Figure 36. Optical montage of Nicalon/SiC composite showing a continuous layer of porosity, that is the basis for FEM analysis.

analysis was used to generate plots of maximum axial stress and maximum axial displacement as a function of aspect ratio, at a given stiffness of the compliant layer. Analytical results were compared to the FEM analysis, whenever possible.

Figure 37 shows axial stress distributions as a function of distance from the neutral axis with a compliant layer stiffness, E_{cl}, of 50 GPa for different aspect ratios. At high aspect ratios (e.g., 6.67) the stress distribution in the beam was much broader (due to higher applied moment) than at lower aspect ratios. At an aspect ratio of 1.67, for example, the stresses varied from -2×10^8 Pa to 2×10^8 Pa compared to -8.88×10^8 Pa to 8.88×10^8 Pa for an aspect ratio of 6.67. This explains why short beams are used for interlaminar shear tests, because the axial stresses are small compared to the shear stresses.

When the compliant layer stiffness was low (e.g., 0.5 GPa), the stresses in the compliant layer were close to zero, causing the mismatch at the interface between composite and compliant layers to be much larger and increasing the interlaminar shear stresses between the layers.

A comparison between analytical and FEM solutions for a beam with aspect ratio of 6.67 and E_{cl} of 50 GPa showed very good agreement, Fig. 38. A slight deviation was observed in the part of the beam under maximum compressive stresses, and this was due to a stress concentration at the load application point. For all spans, the analytically calculated stresses agreed fairly well when the compliant layer had a stiffness of 50 GPa, although there was a slight increase in error with increasing span, Fig. 39. At lower stiffnesses of the compliant layer, e.g. when E_{cl} was 0.5 GPa, the difference between analytical and FEM solutions became larger, Fig. 40. This was due to the fact that in the analytical solution we assumed that deformations in the composite and compliant layers were the

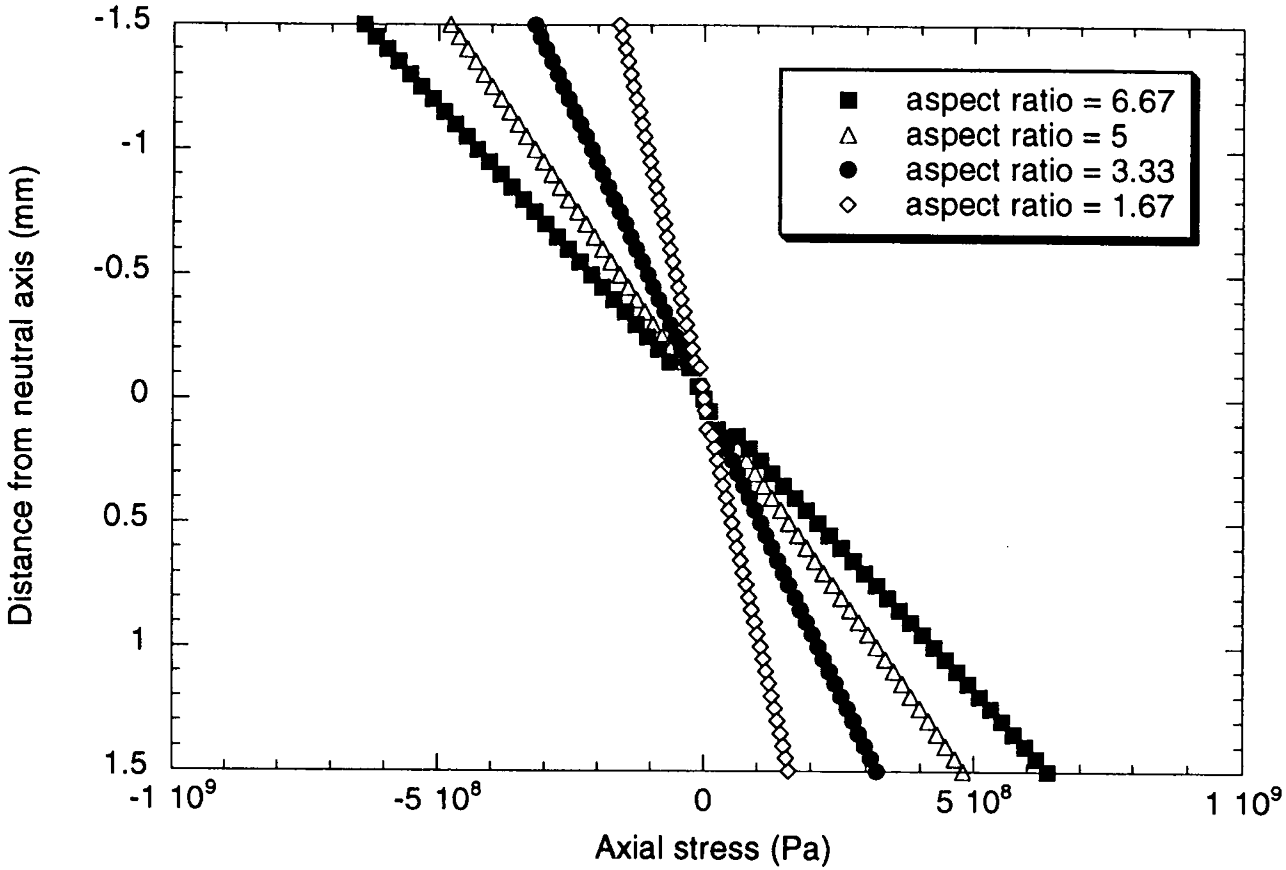

Figure 37. Analytical axial stress distributions in a beam in three-point bending, as a function of distance from the neutral axis with a compliant layer stiffness, E_{cl}, of 50 GPa.

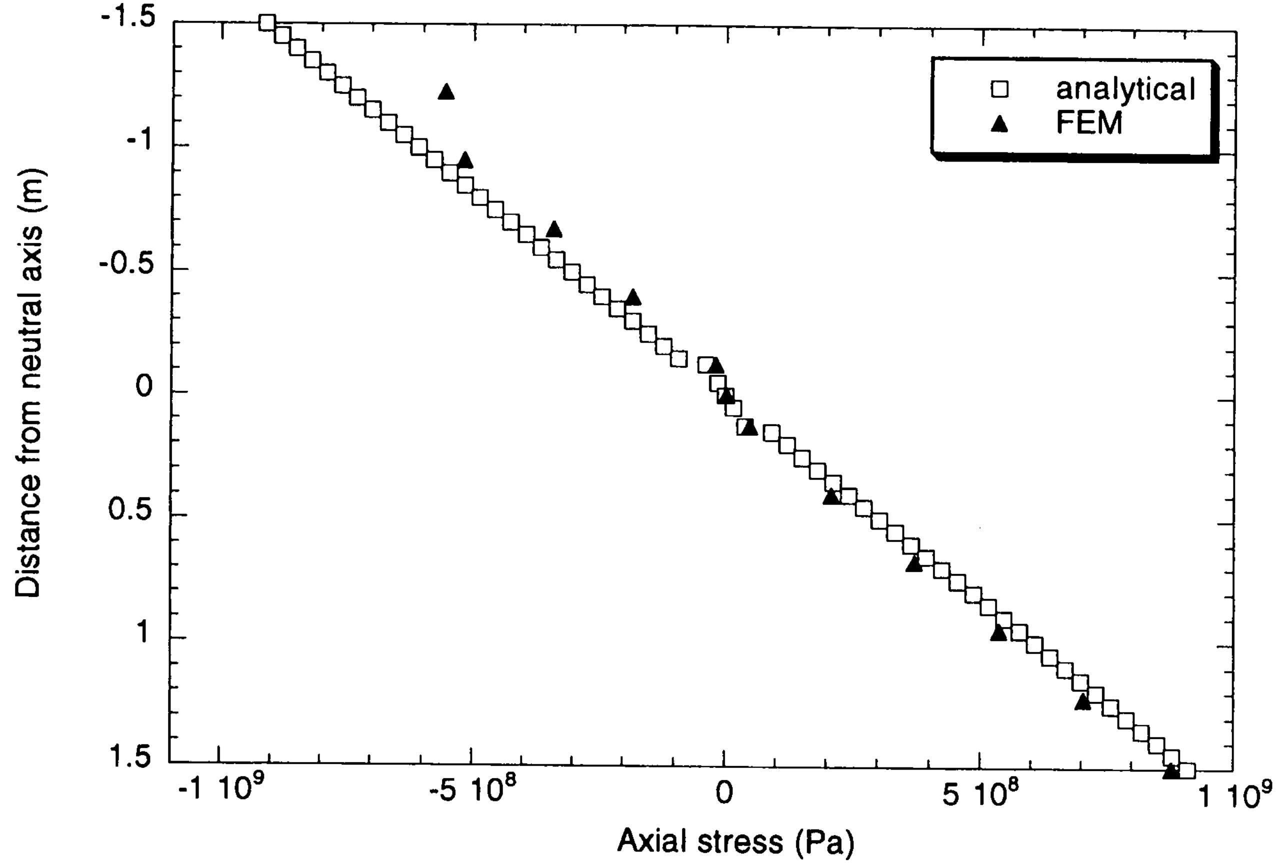

Figure 38. Comparison between analytical and FEM solutions of axial stresses as a function of distance from the neutral axis, for a beam with aspect ratio of 6.67 and E_{cl} of 50 GPa, showing very good agreement.

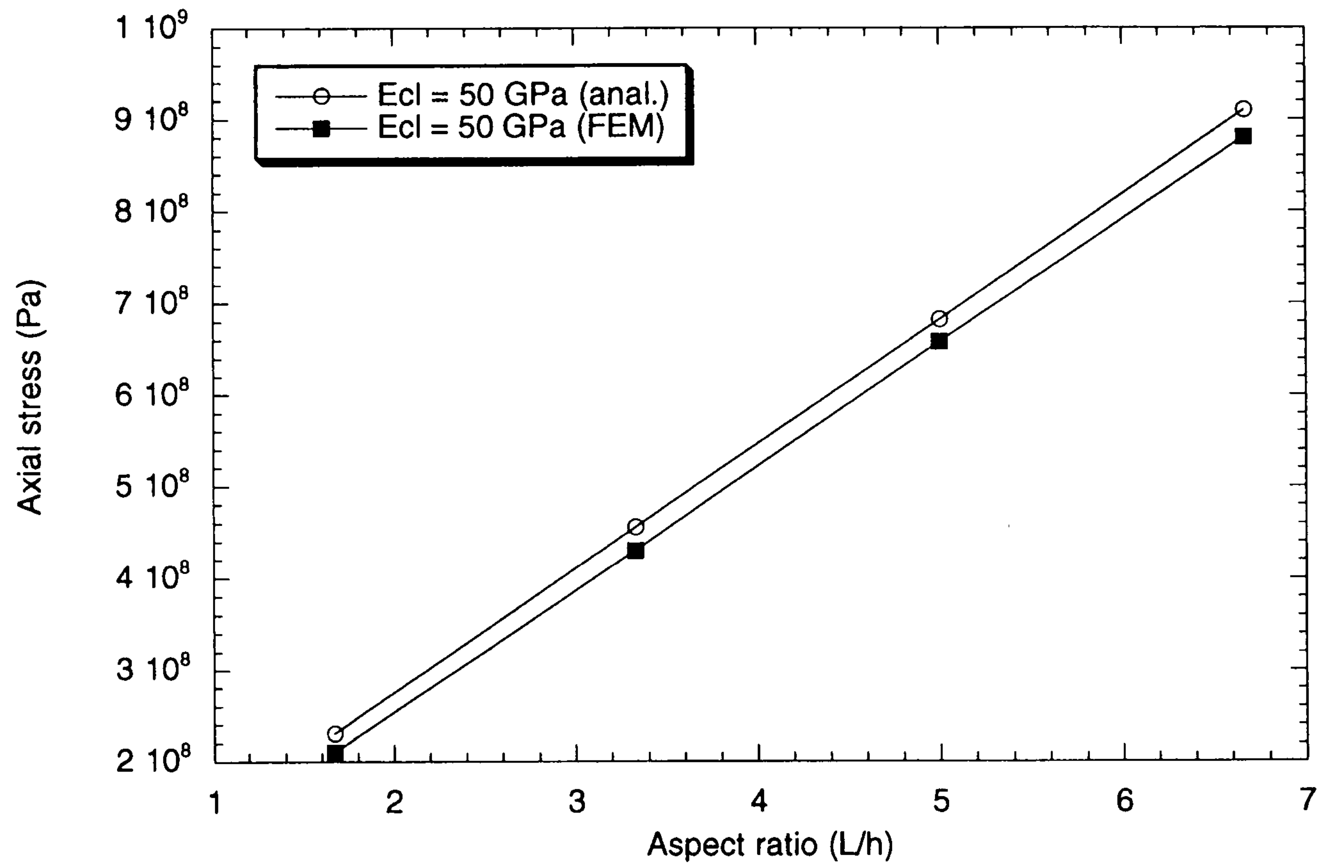

Figure 39. Comparison between analytical and FEM solutions for maximum axial stresses for all calculated spans at E_{cl} of 50 GPa, showing good agreement.

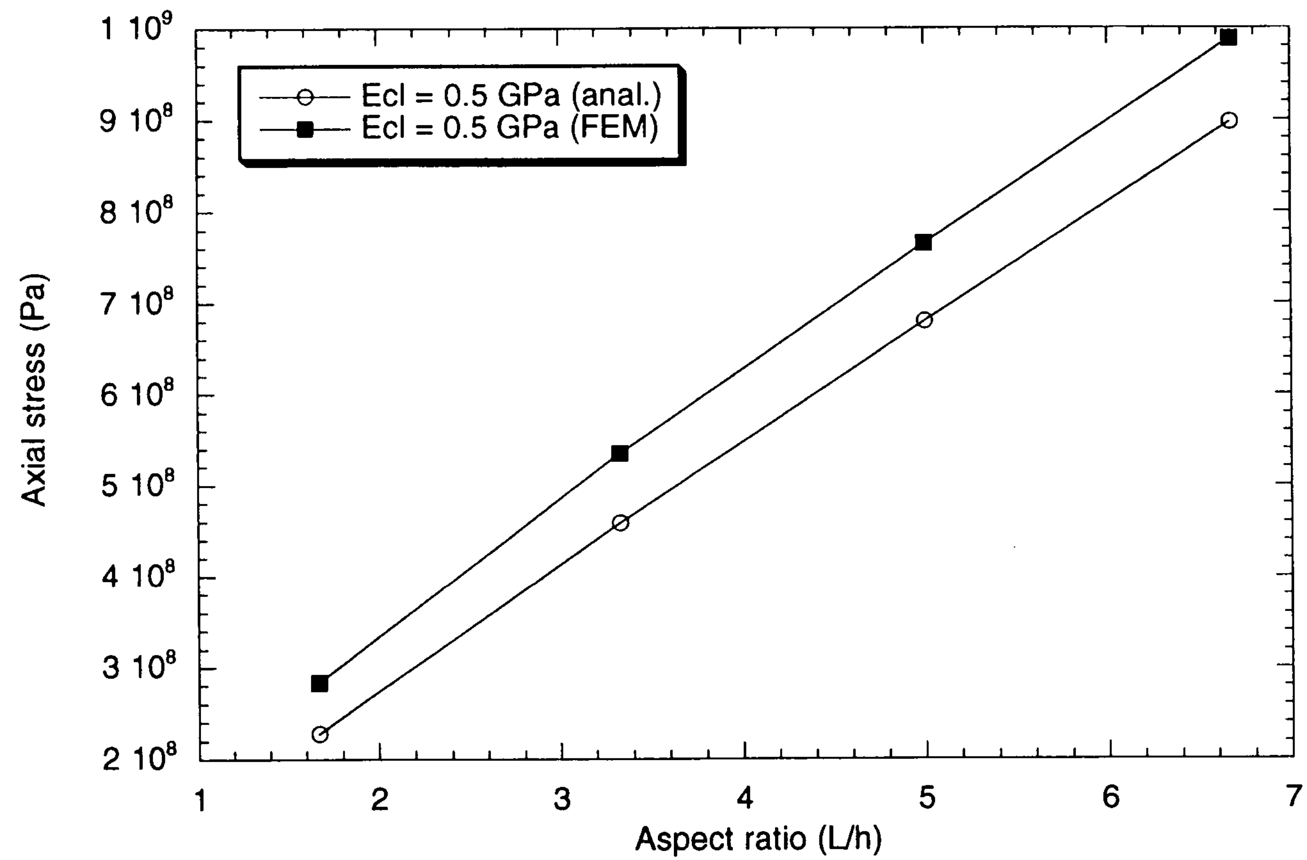

Figure 40. Comparison between analytical and FEM solutions for maximum axial stresses for all calculated spans at E_{cl} of 0.5 GPa, showing deviation in results because the analytical solution assumes that deformation in the composite and compliant layers are the same.

same. Since this is not true in practice, and the FEM solution did not make that assumption, the FEM results were more realistic. Thus, when the difference in deformation was small, as in the case of E_{cl} of 50 GPa, the two solutions were very close, but when deformation of the compliant layer was more severe, such as E_{cl} of 0.5 GPa, the analytical solution diverged from the FEM solution.

Finally, the variation in normalized maximum axial stresses was plotted versus aspect ratio at a given E_{cl}, Fig. 41. It can be seen that the lower the stiffness of the compliant layer and the lower the aspect ratio, the higher the stresses in the beam. This is as expected from the work of Steif and Trojnacki (32-34).

Color plots from FEM show the stress distributions in the beam. As would be expected in a simple beam, the tensile stresses (red) were at the bottom part of the beam while compressive stresses (purple) were at the top part of the beam. The neutral axis was at the center of the beam and is indicated by green. Notice that at higher aspect ratios, more of the beam was subjected to the applied load than at lower aspect ratios, Figs. 42 and 43.

Gap element analysis

Color plots of axial stress distributions obtained by the gap element analysis showed different results than those obtained in compliant layer analysis, Fig. 44. Each of the two layers behaved independently, that is, each layer showed a stress distribution from compressive to tensile. More importantly, it was observed that at the interface between the two layers, the top layer had maximum tensile stresses while the bottom layer had maximum compressive stresses. Therefore, at the interface we obtained a situation of complete

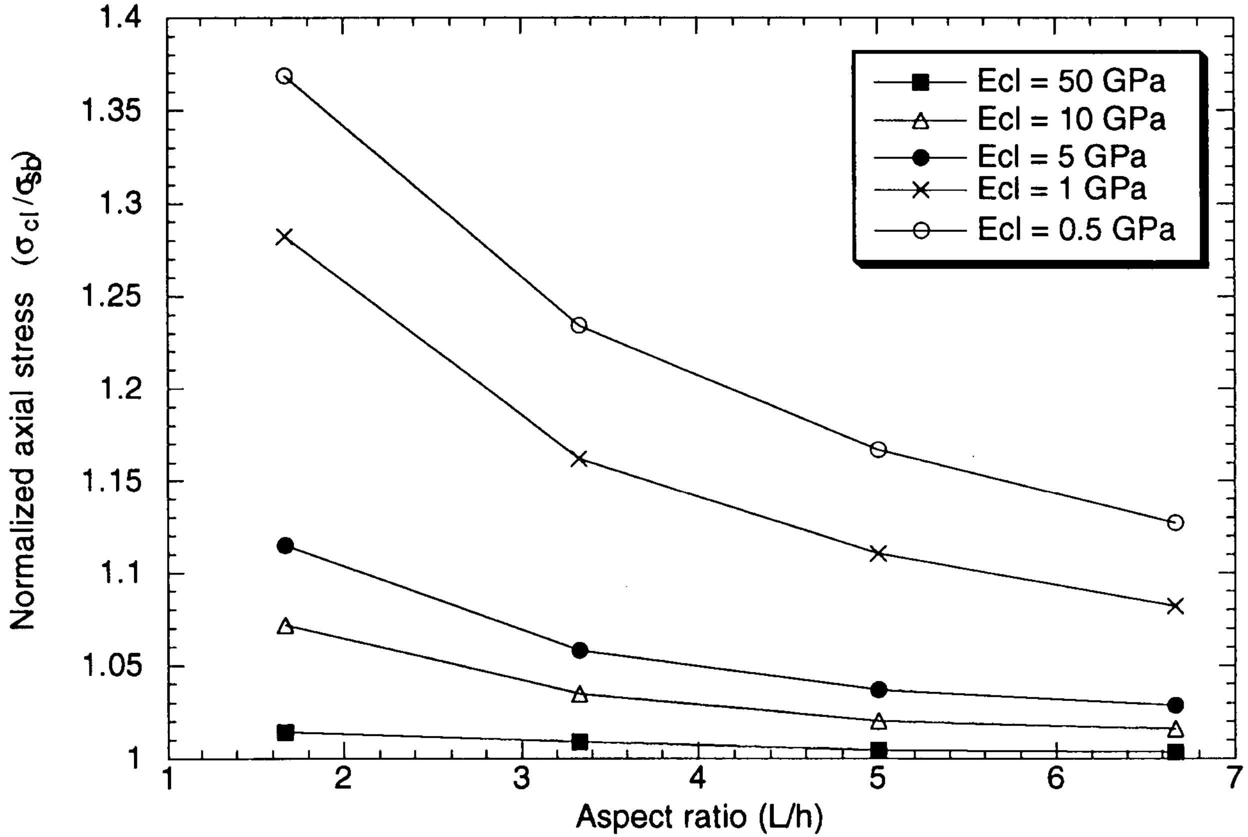

Figure 41. FEM Normalized maximum axial stresses versus aspect ratio for a given value of E_{cl}.

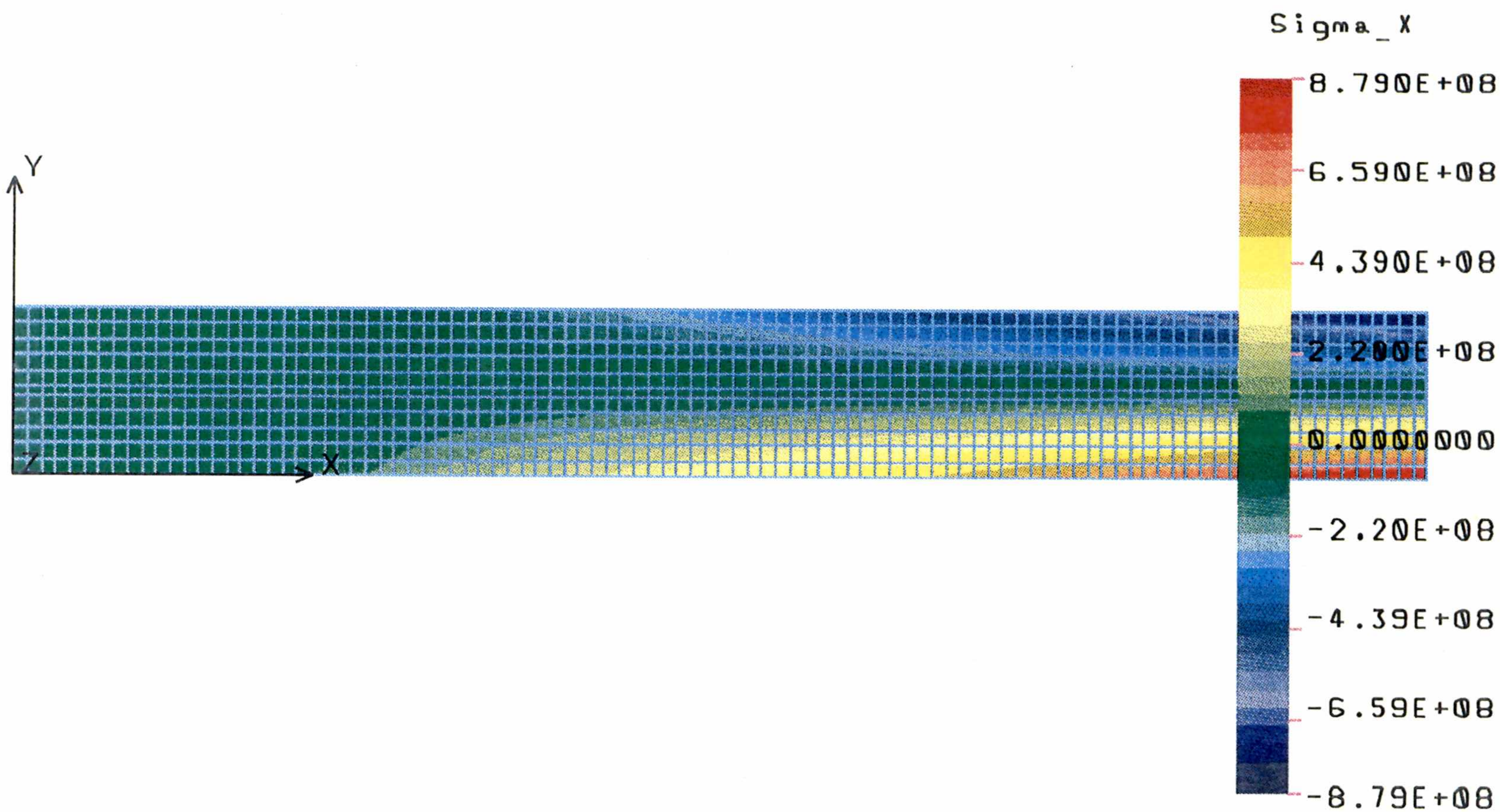

Figure 42. Color plot from FEM showing axial stress distributions of a beam of high aspect ratio, at E_{cl} of 50 GPa.

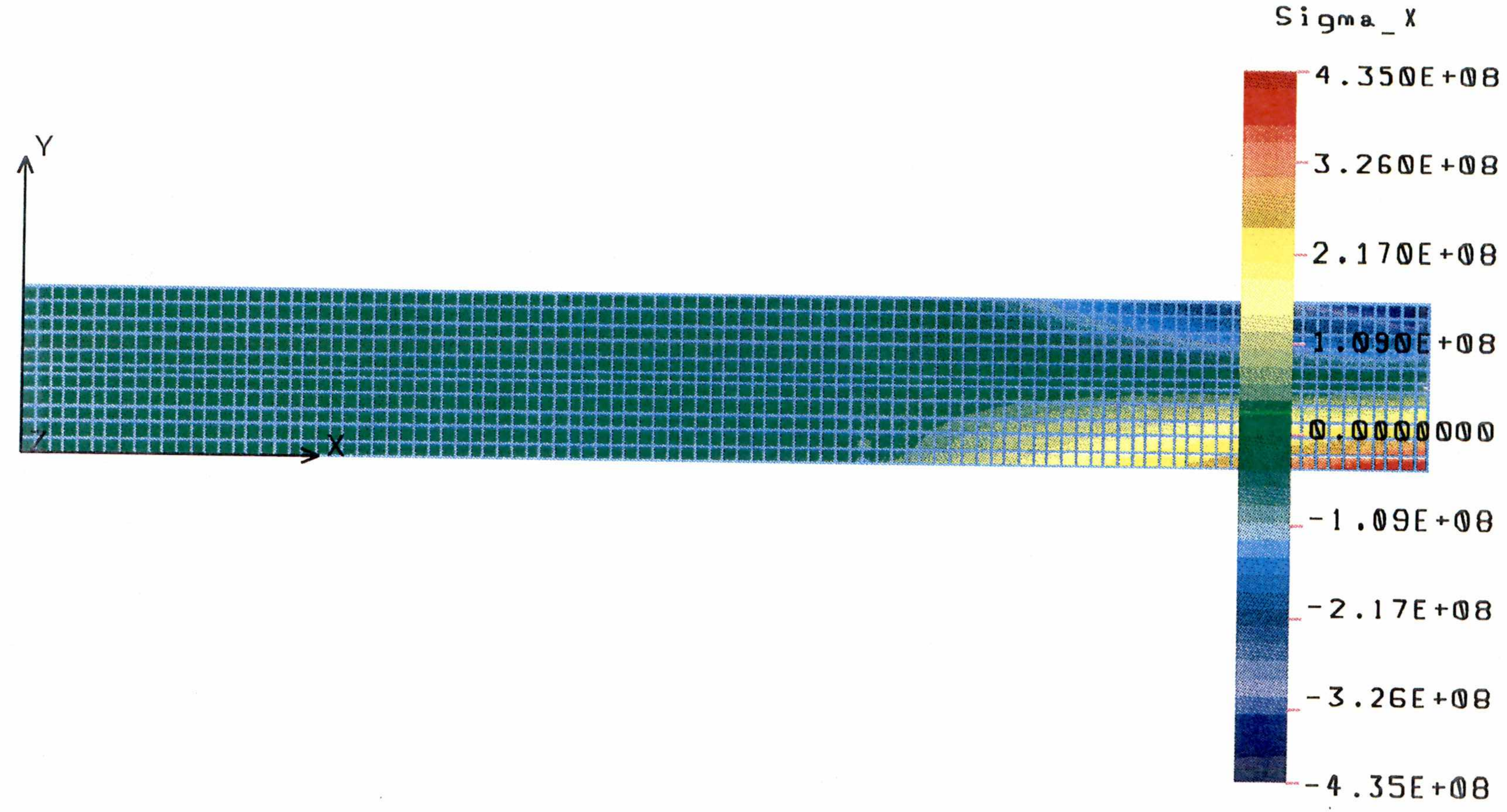

Figure 43. Color plot from FEM showing axial stress distributions of a beam of low aspect ratio, at E_{cl} of 50 GPa. Notice that at higher aspect ratios, more of the beam is subjected to loading that at lower aspect ratios.

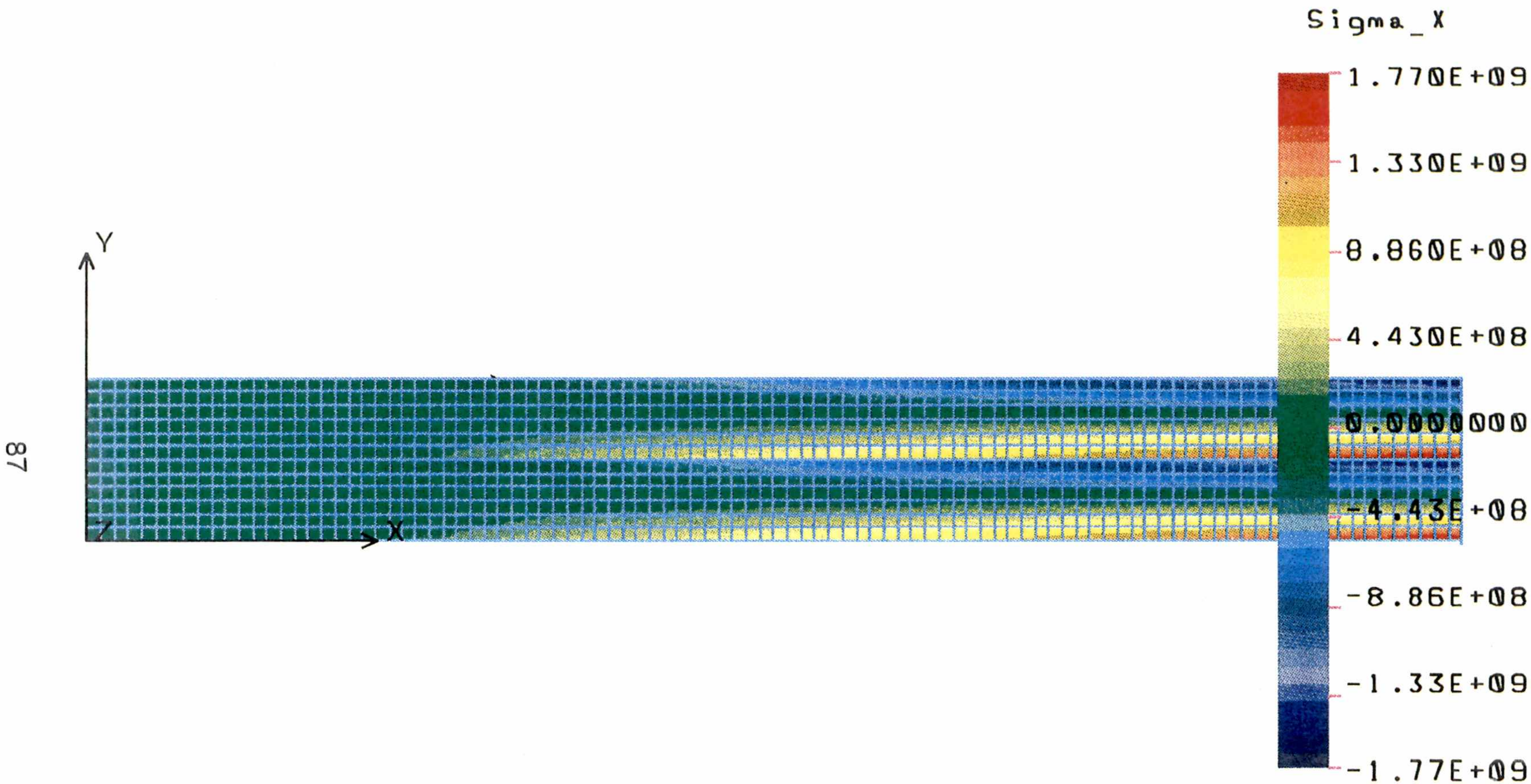

Figure 44. Color plot from FEM showing axial stress distributions of a beam using gap element analysis to simulate friction. Compressive-tensile stress mismatch at the interface of the two layers is responsible for high interlaminar shear stresses in the composite.

mismatch of stresses, from compressive in one layer to tensile in the other. This mismatch was responsible for the maximum shear stresses being present between the plies of the laminated composite, and consequently, when tested in bending, these materials failed by a weak interlaminar shear stress. A plot of the maximum axial displacement showed a similar situation at which there was a mismatch between negative and positive displacements at the interface, Fig. 45. This mismatch was greatest at the end of the beam where there was no constraint in the x-direction.

These results were not confined to a model with only two layers. In the two-layer model, the neutral axis of the beam coincided with the interface between the layers. To prove that this coincidence did not affect the results, a three layer model was used as well. Once again, the color plots for axial stresses and displacements showed mismatch at the interfaces, but in the three layer model one observed mismatch at two interfaces instead of one, Fig. 46.

Results for a beam in four-point bend showed a similar situation to a beam in three-point bend. As can be seen from the bending moment diagram of beams in three- and four-point bend, Fig. 7, the maximum stresses in four-point bend were constant between the top two loading points, instead of at a point for three-point bend. Since only a fourth of the beam is considered in the FEM analysis, the color contours of the beam in four-point bend are constant from the top support to the edge of the beam, Fig. 47.

Results were also obtained for the axial stress and displacement distributions at the interface between the two plies, as a function of position in the x direction, for all four analyzed aspect ratios. Figures 48 and 49 show the normalized stress distributions, with respect to the simple beam of same aspect ratio, for spans of 6.67 and 3.33, respectively. The stresses in both layers gradually

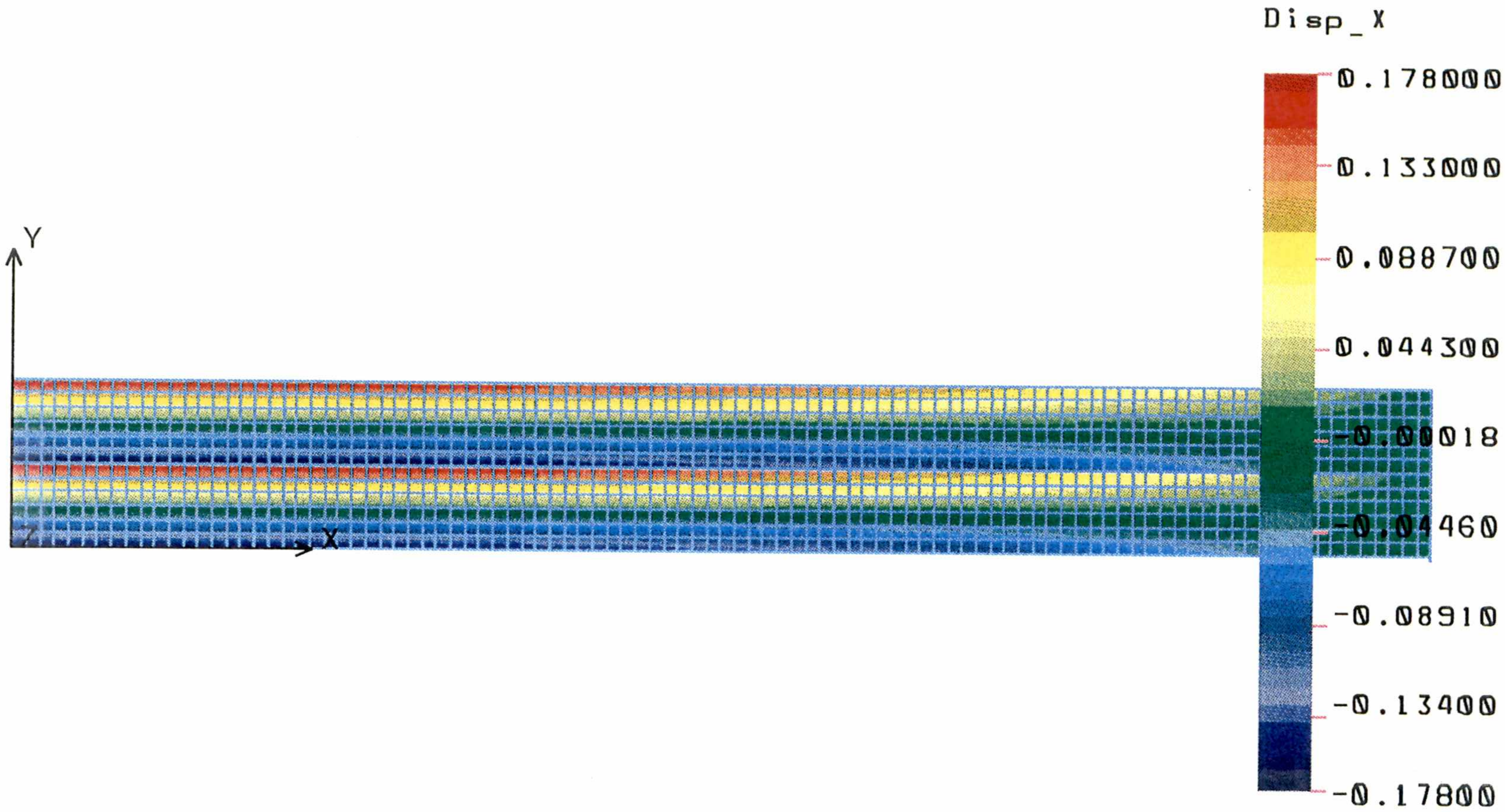

Figure 45. Color plot from FEM showing maximum axial displacement distributions of a beam using gap element analysis. Similar mismatch between negative and positive displacements at the interface is observed.

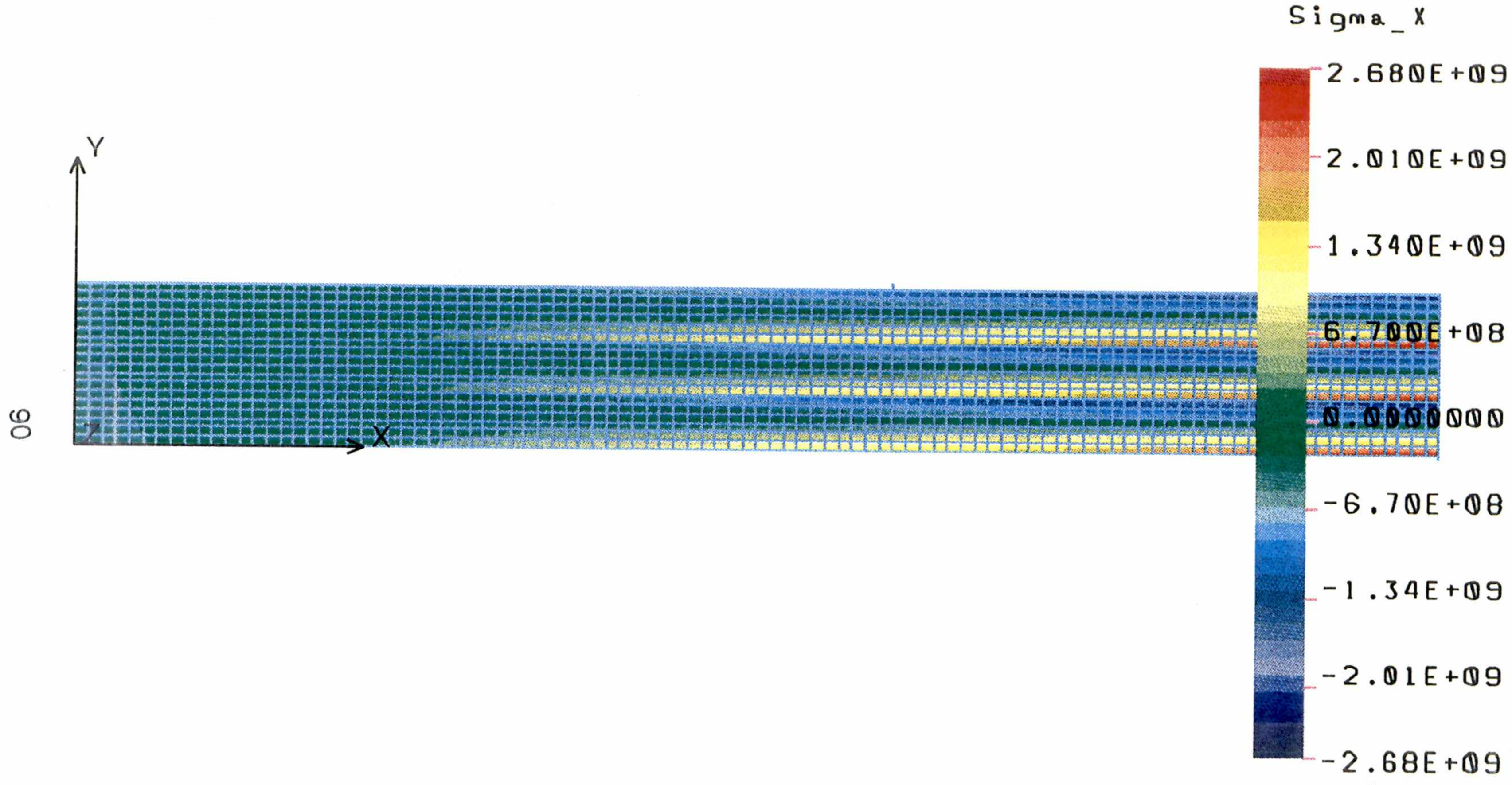

Figure 46. Color plot from FEM showing axial stress distributions in a three layered model. In this model one observes mismatch at two interfaces instead of one.

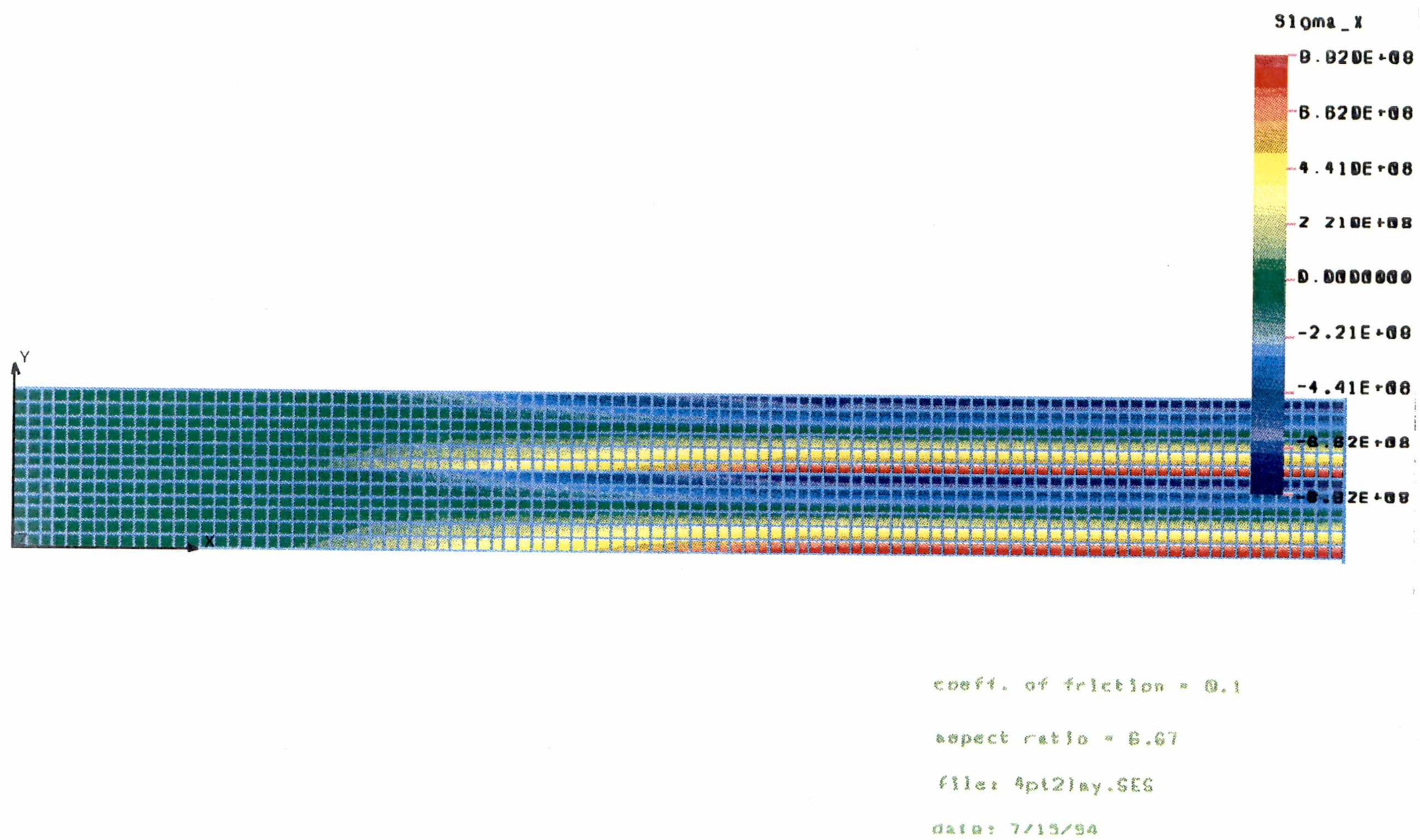

Figure 47. Color plot from FEM showing axial stress distributions in a two layered beam in four-point bending. Notice that the stress contours are constant between the top loading point and the edge of the beam in four-point bending, consistent with the bending moment diagram given in Fig. 7.

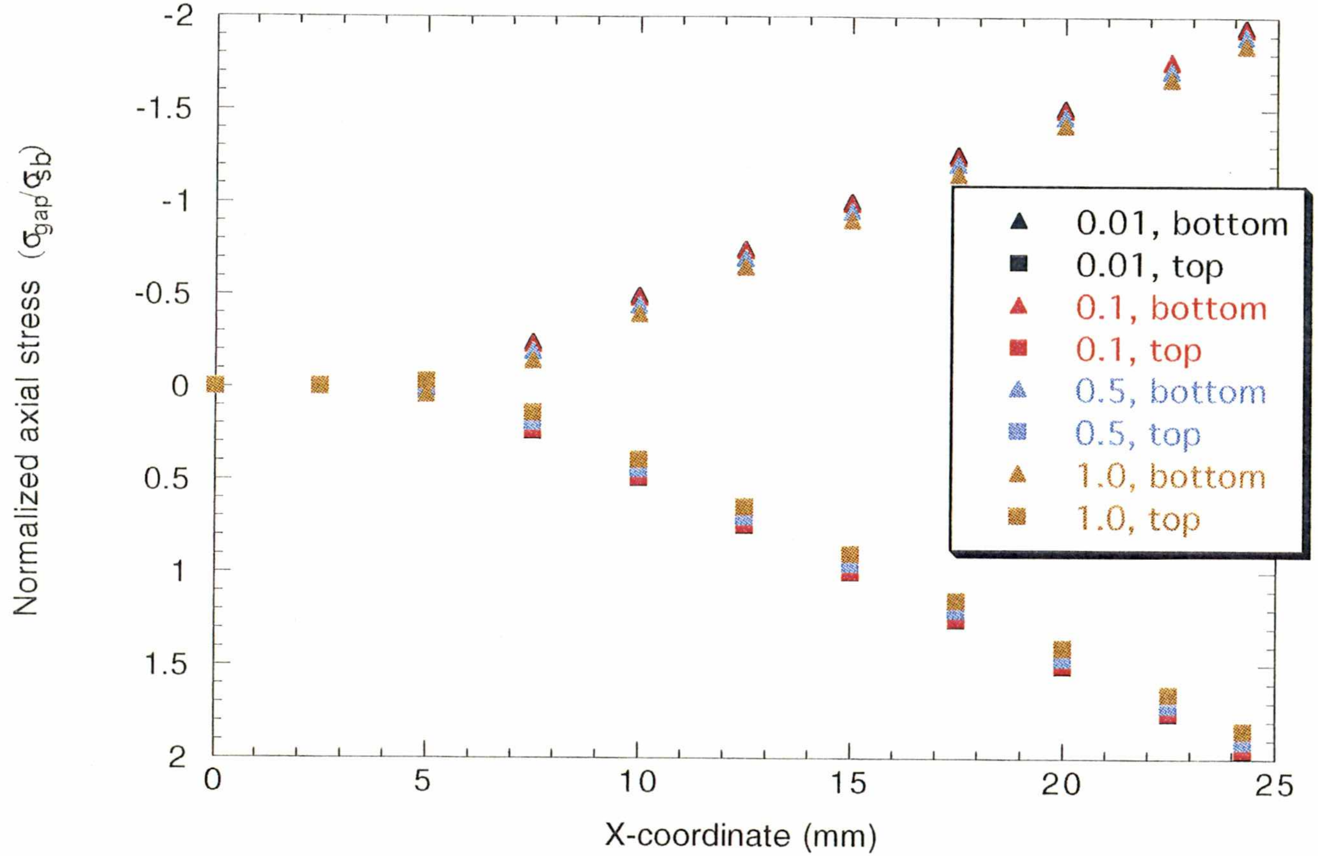

Figure 48. Normalized stress distributions at the interface between the two layers as a function of position in the x direction of aspect ratio of 6.67, at a given coefficient of friction.

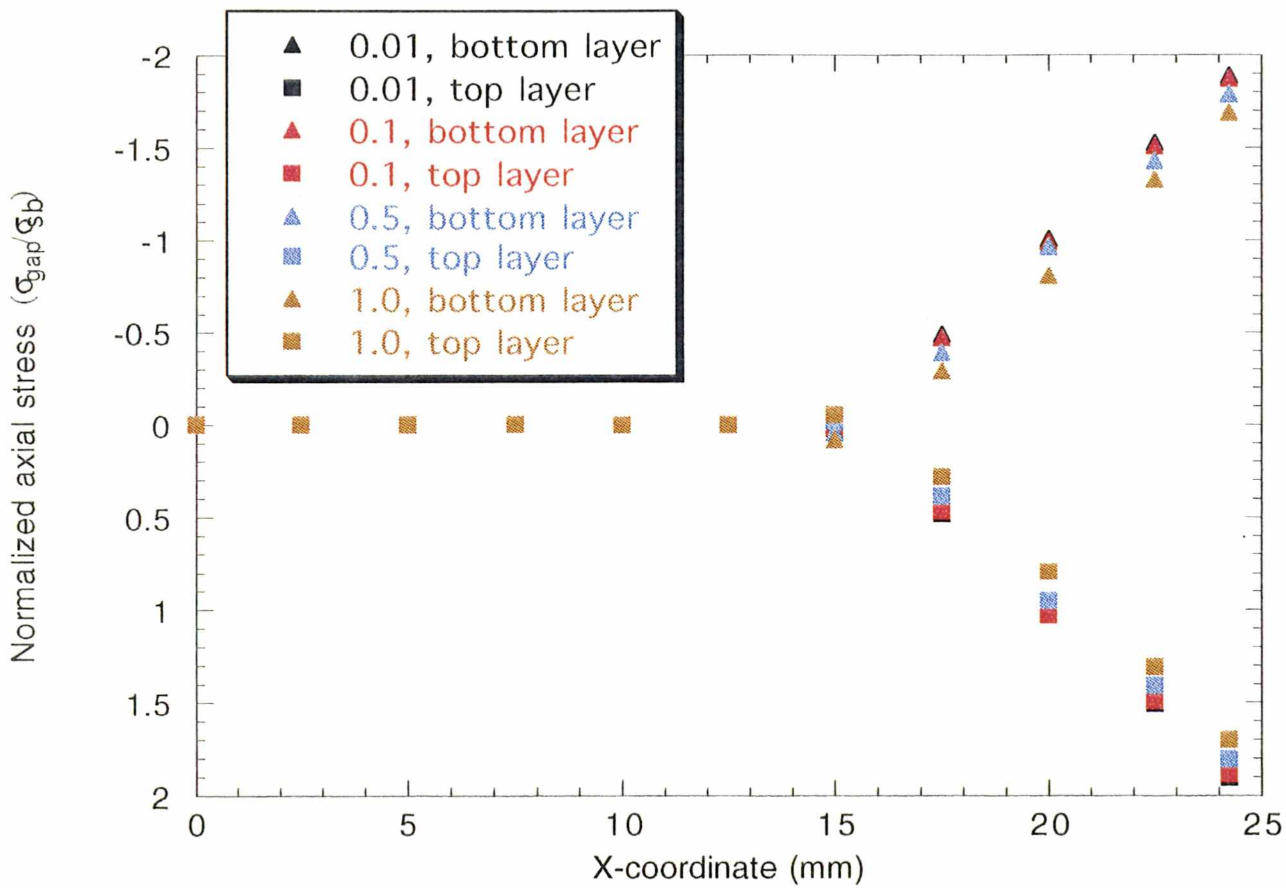

Figure 49. Normalized stress distributions at the interface between the two layers as a function of position in the x direction of aspect ratio of 3.33, at a given coefficient of friction.

increased from the support until they reached a maximum at the point where the load was applied. More importantly, the stress mismatch between the layers increased until it reached a maximum at the load application point.

It was interesting to note that the tensile stresses present in the top layer at the interface were only slightly lower than the tensile stresses on the tensile side of the beam. This is an important consideration because simple beam equations are typically used to measure applied stresses in these materials, and these equations only take into consideration the stresses on the tensile side of the beam. FEM showed, however, that these stresses are present in every layer and not only on the tensile surface of the beam.

These results can be explained in light of the fact that the normal applied stress, σ_y, can be related to the axial stress, σ_x, and the coefficient of friction, μ, by the following equation:

$$\sigma_y = \sigma_x \mu$$

This equation can be used to predict when sliding between plies will occur. If the normal stress exceeds the value given by the right hand side of the equation, sliding will occur. So, with a lower coefficient of friction, a lower normal stress is needed for sliding to begin. When more sliding occurs, the radius of curvature of the beam in bending will be increased, so large stresses will be applied, as confirmed by FEM.

By equating σ_y to the product of σ_x and the coefficient of friction, the right hand side of the equation can be considered a measure of the interlaminar shear strength of the composite. That is, when the interlaminar shear strength (in this case, controlled by the coefficient of friction, μ) is exceeded due to σ_y, sliding of the plies begins.

The results presented here were independent of aspect ratio because the analysis was conducted under the assumption that all nodes at the interface would slide when the above condition relating normal and axial forces through the coefficient of friction would occur. It should also be noted that the FEM model assumed that the extent of bonding was the same from one side of the bar to the other. In reality, this is likely to be true between a given pair of adjacently bonded plies, while in the rest of the composite, bonding may be imperfect and non-periodic. Furthermore, interbundle porosity was not taken into consideration because it was very small in comparison to interlaminar porosity and therefore not responsible for sliding. Interbundle porosity was very important in fatigue, however, due to localized matrix cracking and damage.

It was also noted that at a coefficient of friction close to zero, normalized maximum axial stresses were nearly twice that of the simple beam values. For a three-layer beam, the stresses were nearly tripled, see Fig. 46. A deformation plot of the three-layered beam is shown in Fig. 50. Notice the sliding of the layers with respect to each other after the bending load was applied.

A direct correlation between number of layers in the model and maximum axial stresses in each layer at a coefficient of friction of zero can be made as follows. Consider the equation for stresses in three-point bending (1,31):

$$M = \frac{P}{2} \cdot \frac{S}{2} = \frac{PS}{4} \quad \text{so}$$

$$\sigma = \frac{6PS}{4bh^2} = \frac{3PS}{2bh^2}$$

If we sub-divide the simple beam into a beam of n layers, that completely slip with respect to each other (since $\mu = 0$), each layer will have a thickness of h/n. Similarly, the maximum bending moment in each layer will be PS/4n. Substituting into the previous equation we find that:

$$\sigma = \frac{6PS}{4nb\frac{h^2}{n}} = \frac{3PSn}{2bh^2}$$

Thus, the maximum applied load in each layer is magnified n times, causing the beam to fail prematurely, assuming a completely linearly elastic approach is applied to this problem.

Axial stress distributions were also compared as a function of position in the y direction. Stresses were obtained across the height of the beam, at the point where the load was applied versus aspect ratio at a given coefficient of friction. Notice that the stress distributions in the two layers were almost mirror images of each other. Once again, the compressive-to-tensile jump in axial stress was observed at the interface between the two layers. Figures 51 and 52 show results for a beams with aspect ratios of 6.67 and 3.33, respectively.

As expected, friction did not play a role in the edge-on orientation. FEM color plots for coefficients of friction of 0.1 and 1.0 were identical, Figs. 53 and 54. Since the loading was distributed evenly in each ply, deflection of both layers was equal so no interlaminar shear effects were present.

Finally, from the FEM analysis presented above, we see that stress enhancement and sliding of plies in the transverse orientation was responsible for premature failure in CVI composites with low interlaminar shear strength.

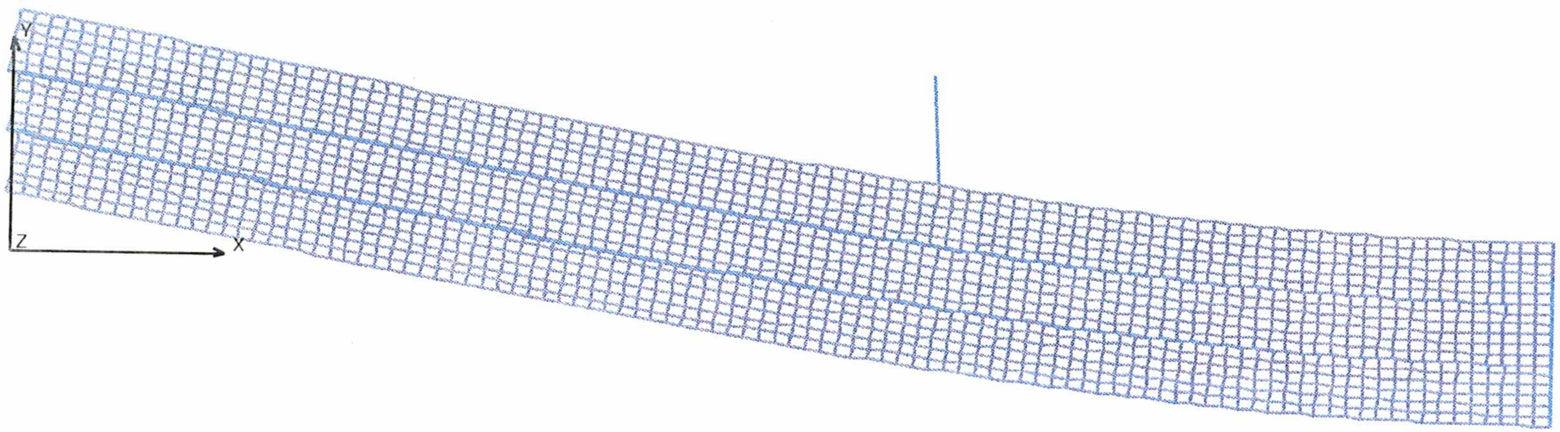

Figure 50. Deformation plot of a three-layered beam using gap element analysis. Notice sliding between layers after deformation.

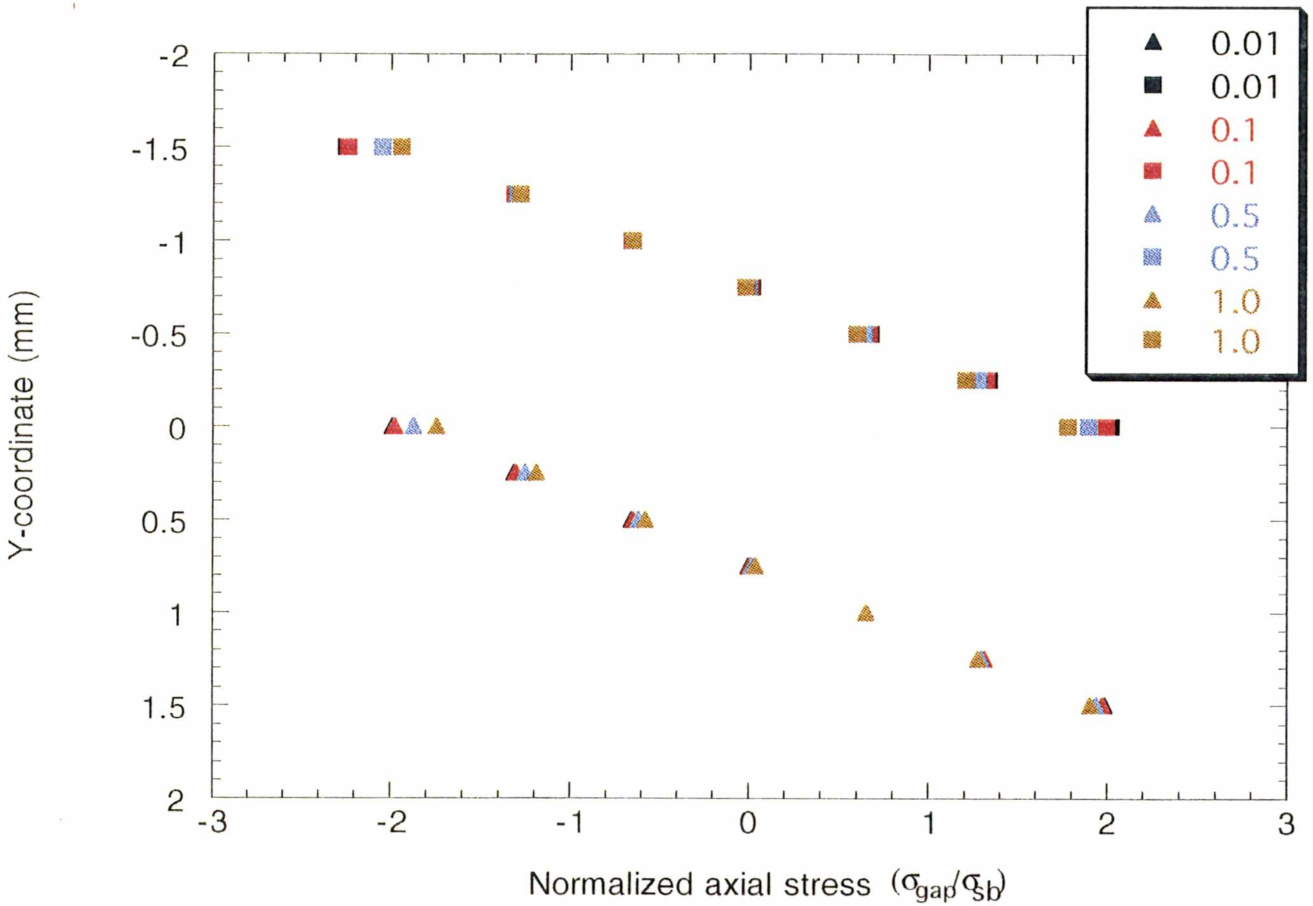

Figure 51. Normalized stress distributions as a function of distance from the neutral axis for a beam of aspect ratio of 6.67, at a given coefficient of friction.

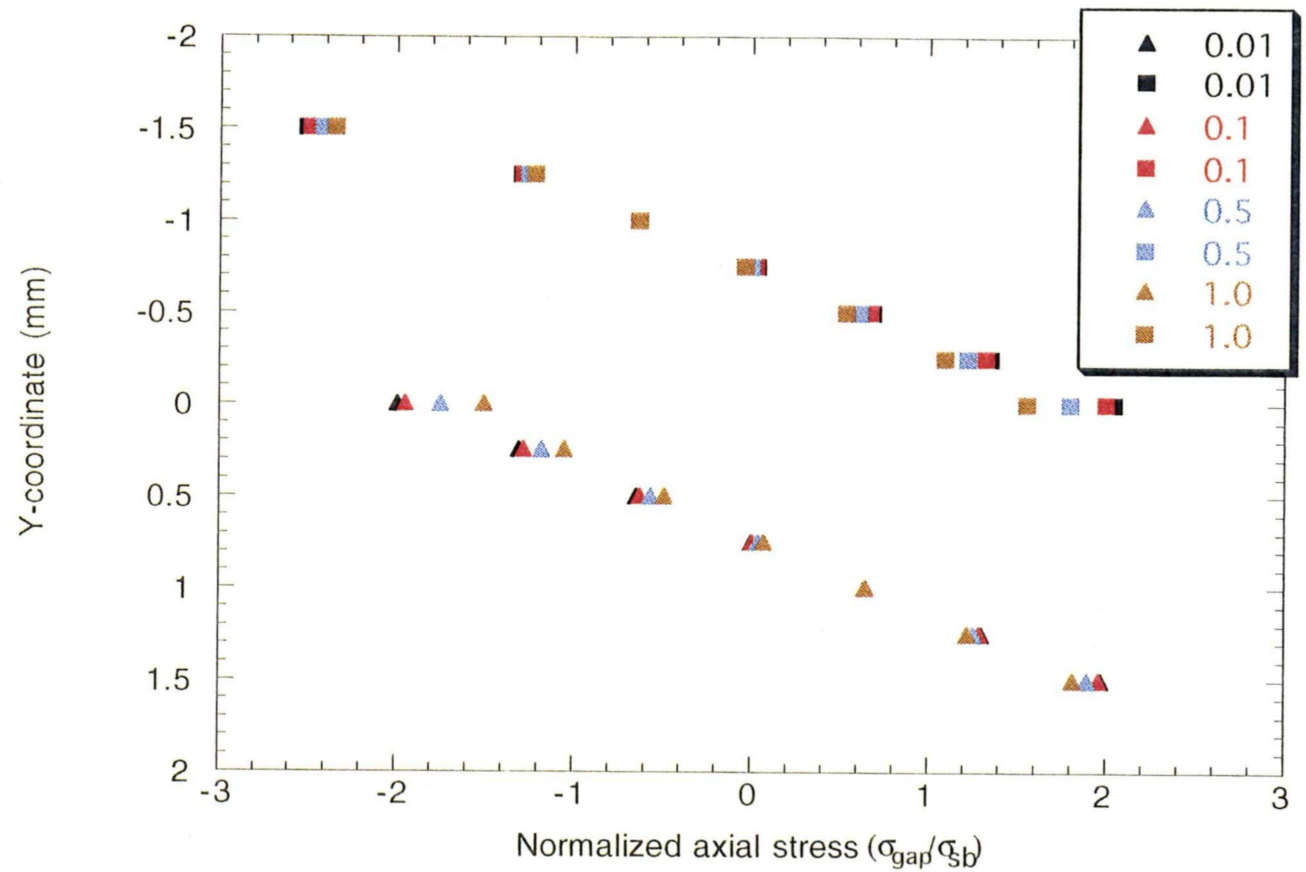

Figure 52. Normalized stress distributions as a function of distance from the neutral axis for a beam of aspect ratio of 3.33, at a given coefficient of friction.

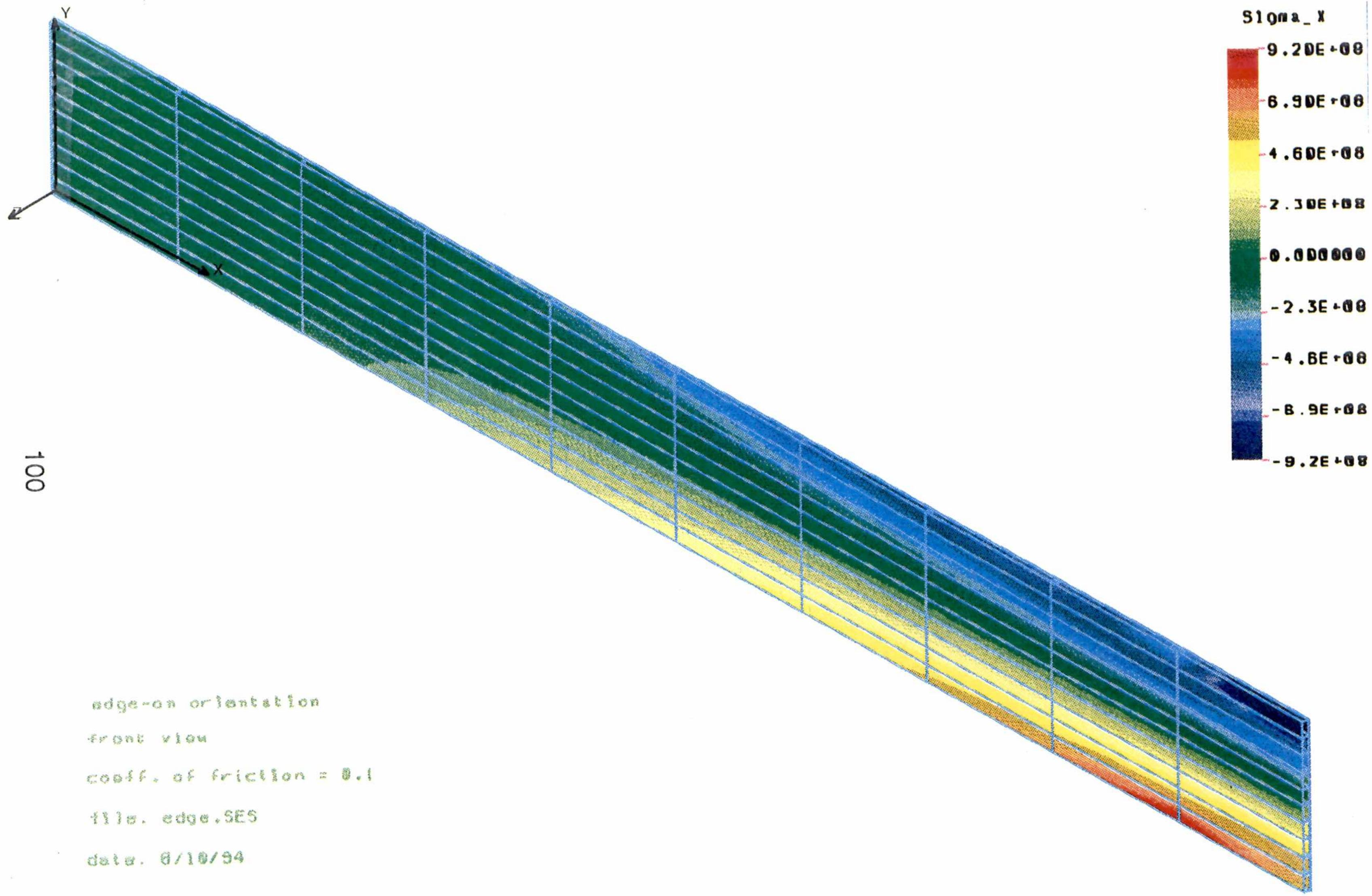

Figure 53. Color plot of axial stress distribution in a beam of edge-on orientation for coefficient of friction of 0.1.

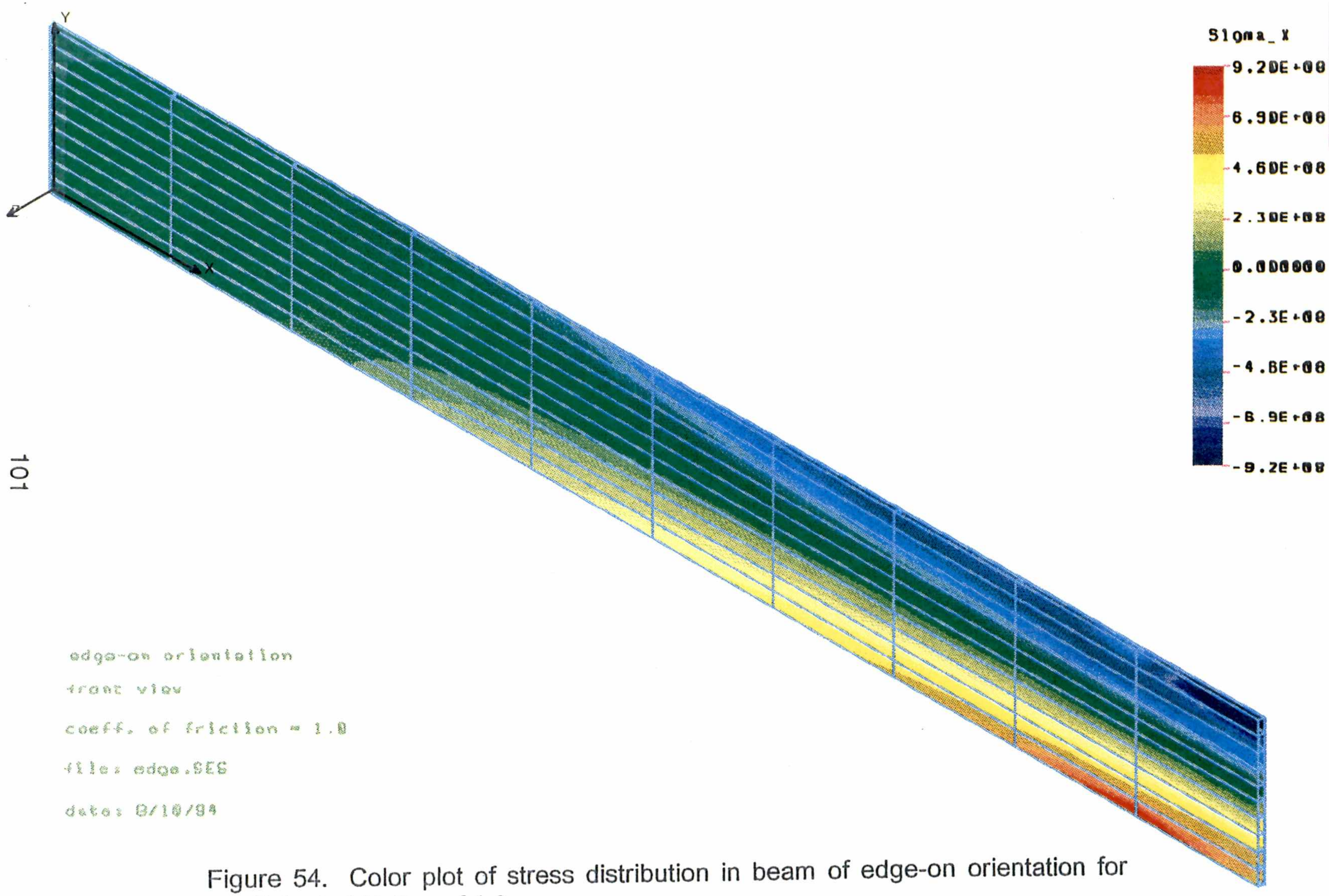

Figure 54. Color plot of stress distribution in beam of edge-on orientation for coefficient of friction of 1.0.

The edge-on orientation, on the other hand, was not susceptible to friction effects so higher strengths were obtained in this orientation.

Furthermore, it was shown, by using compliant layers with different moduli values to model porosity, that the lower the stiffness of the compliant layer, the higher the enhancement of stresses in the beam. More importantly, this analysis also showed that the smaller the span, the higher the amount of shear stresses between layers and therefore the greater the stress enhancement.

Gap elements used to simulate different coefficients of friction showed that the lower the coefficient of friction (i.e., the weaker the bonding between layers), the higher the stress enhancement in the beam. Therefore, with a higher degree of interlaminar porosity, stress enhancement in the beam is larger and failure would occur at lower loads than expected. It follows that in a composite that is 100% dense, the difference in strength between the two orientations should be negligible. This explains why, in monotonic and cyclic loading, the difference between edge-on and transverse was greater in Nicalon/SiC composite than in Nextel/SiC, since the latter composite was denser.

CHAPTER V

CONCLUSIONS

From the results and discussion, we can draw the following conclusions on the effect of fiber fabric orientation, with respect to the loading axis, on the monotonic and cyclic loading behavior of FCVI ceramic matrix composites:

Monotonic flexure tests showed higher toughness and strength in edge-on than in transverse geometry. This behavior was due to the different failure mechanisms in the two geometries. The primary failure mechanism in the transverse orientation was branching and arrest of the crack due to interlaminar shear. In the edge-on orientation, load was transferred equally between plies and failure was predominantly by in-plane shear in the fiber fabric. Fiber pullout was predominant in both composites and geometries accounting for most of the toughness in both composite systems.

S-N curves showed that transverse specimens were more flexible than edge-on specimens due to weak interlaminar and strong in-plane shear deformation mechanisms, respectively. The curves of Nicalon/SiC composites showed more difference between the two geometries because of lower overall density which made transverse specimens fail more prematurely due to increased sliding of plies.

Post-fatigue tests on specimens that survived 10^5 cycles indicated that the transverse orientation became more compliant, and showed higher work of fracture than the as-received material in both composites. Nicalon/SiC transverse specimens showed plateaus in stress after the ultimate strength was reached, due to sliding of plies. Edge-on specimens had lower work of fracture after cyclic fatigue due to fatigue damage, but due to the absence of sliding between plies, retained a higher percentage of their overall strength.

Interlaminar shear strengths of both composites were lower in comparison to in-plane shear strengths, because sliding of plies (interlaminar shear) took place at lower stresses compared to tearing of the fiber fabric (in-plane shear). This further corroborates the mechanisms proposed to explain failure in bending of transverse and edge-on orientations.

Due to higher matrix volume fraction (higher overall density) Nextel/SiC composites showed higher interlaminar shear strengths. Matrix volume fractions also played an important role in in-plane shear strengths, because even with a much lower strength fiber, Nextel/SiC composites had higher strengths than Nicalon/SiC composites.

Compliant layer analysis in FEM showed that normalized axial stresses and displacements were enhanced over the stresses in a simple beam as the aspect ratio increased. Therefore, transverse beams with short spans will fail at premature stresses due to interlaminar shear interactions compared to edge-on beams. This behavior was observed experimentally in both Nicalon/SiC and Nextel/SiC composites.

Gap element analysis in FEM showed that each layer in the beam had a compressive to tensile distribution such that the mismatch at the interface of these layers caused the greatest amount of interlaminar shear. As the coefficient of friction between the layers decreased, the normalized axial stresses and displacements increased. Therefore, a greater amount of interlaminar porosity will result in greater stress enhancement in a beam. This explains why transverse Nicalon/SiC, which was less dense than Nextel/SiC, had a lower strength compared to edge-on Nicalon/SiC. A similar comparison in Nextel/SiC showed that the strength difference in the two orientations was less significant.

Three-layer beams analyzed using gap elements showed that at coefficient of friction of 0 (i.e., complete sliding occurred and there was no bonding between plies), stress enhancement was directly related to the number of layers in the beam.

CHAPTER VI

SUGGESTED FUTURE WORK

Based on the results obtained in this work, the following suggestions for future work can be made:

1. Conduct tensile testing of both orientation and compare to bending results.

2. Test specimens in fatigue with different interfacial coating thicknesses. A thicker coating will perhaps not be completely degraded after fiber sliding during fatigue, so the post-fatigue properties may not be degraded.

3. Obtain information on frequency effect, testing in displacement control, and high temperatures on the fatigue behavior of these CVI composites. Higher frequency can cause substantial increases in temperature at the fiber/matrix interface due to frictional heating (63). The extent of heating can also be equated to the frictional shear stress at the interface. Testing at high temperatures will likely cause oxidation of the carbon interface layer and the formation of a glassy phase that promotes a strong bond between fiber and matrix. Clearly, a high temperature, oxidation resistant fiber coating is desperately needed.

4. Examine the effect of aspect ratio on the flexural behavior of transverse and edge-on orientations. Using Steif and Trojnacki's analysis or a modified

analysis, the bend strengths can be correlated to tensile behavior, as well as coupling interlaminar shear strengths with aspect ratio.

5. Examine the orientation effect in different material systems, since orientation of the laminate with respect to the applied load is very important in design applications. Improvements in processing to increase the interlaminar shear strength are needed for CFCCs to be used in service.

6. Modify existing FEM codes so that one can input the interlaminar shear strength in a composite and directly observe the enhancement in bend stress.

LIST OF REFERENCES

LIST OF REFERENCES

1. K.K. Chawla, **Ceramic Matrix Composites**, Chapman & Hall, London, 1993, p. 4-10.

2. J.A. DiCarlo, *Adv. Mater. & Proc.*, June 1989, 41.

3. T.M. Besmann, B.W. Sheldon, R.A. Lowden, D.P. Stinton, *Science*, **253** (1991) 1104.

4. N. Chawla, P.K. Liaw, E. Lara-Curzio, R.A. Lowden, and M.K. Ferber, in **High Performance Composites - Commonalty of Phenomena**, K.K. Chawla, P.K. Liaw, and S.G. Fishman (eds.), Warrendale, PA, 1994, p. 291.

5. R. Venkatesh and K.K. Chawla, *J. Mater. Sci. Lett.*, **11** (1992) 650.

6. J.D. Embury, N.J. Petch, A.E. Wraith, and E.S. Wright, *Trans. AIME*, **239** (1967) 114.

7. K.K. Chawla, **Composite Materials, Science and Engineering**, Springer-Verlag, New York, 1987, p. 130.

8. H.E. Helms and P.J. Haley, in **Ceramic Materials and Components for Engines**, ed. V.J. Tennery, Amer. Ceram. Soc., Westerville, OH, 1989, p. 1347.

9. J.W. Holmes, in **Ceramics and Ceramic Matrix Composites**, S.R. Levine (ed.), ASME, New York, 1992, p. 193.

10. L.M. Sheppard, *Adv. Mater. & Proc.*, May 1987, 11.

11. K.M. Prewo, *J. Mater. Sci.*, **22** (1987) 2695.

12. E. Minford and K.M. Prewo, in **Tailoring Multiphase and Composite Ceramics**, C.G. Patano and R.E. Messing (eds.), Plenum Publishing Co., NY, 1986, p. 561.

13. V. Ramakrishnan and N. Jayaraman, *J. Mater. Sci.*, **28** (1993) 5580.

14. T. Ishikawa, in **Silicon Carbide Ceramics - 2**, eds. S. Somiya and Y. Inomata, Elsevier Press, New York, 1991, p. 81.

15. W.J. Lackey, D.P. Stinton, G.A. Cerny, L.L. Fehrenbacher, and A.C. Schaffhauser, in **Proceedings of International Symposium on Ceramic Components for Heat Engines**, Oct. 17-21, 1983, Hakone, Japan.

16. J.W. Holmes, T. Kotil, and W.T. Foulds, in **Symposium on High Temperature Composites**, American Society for Composites, Dayton, OH, (1989), p. 176.

17. J.W. Holmes, *J. Am. Ceram. Soc.*, **74** [7] (1991) 1639.

18. J.W. Holmes, *J. Mater. Sci.*, **22** (1991) 1808.

19. P.C. Paris and F. Erdogan, *J. Basic Engng. Trans*, **85** (1963) 528.

20. A.A. Morrone, S.R. Nutt, and S. Suresh, *J. Mater. Sci.*, **22** (1988) 3206.

21. L.X. Han and S. Suresh, *J. Am. Ceram. Soc.*, **72** [7] (1989) C1233.

22. C.J. Lin and D.F. Socie, *J. Am. Ceram. Soc.*, **74** [7] (1991) 1511.

23. E.Y. Luh, R.H. Dauskardt, and R.O. Ritchie, *J. Mater. Sci. Lett.*, **9** (1990) 719.

24. D.B. Marshall and B.N. Cox, *Acta. Mettall.*, **35** (1987) 2607.

25. S.L. Ogin, P.A. Smith, and P.W.R. Beaumont, *Composites Sci. Tech.*, **22** (1985) 23.

26. W.S. Johnson, in **Damage in Composite Materials**, ASTM STP 775, American Society for Testing and Materials, Philadelphia, (1992), p. 83.

27. P.G. Karandikar and T.-W. Chou, *Ceram. Eng. Sci. Proc.*, **13** (1992) 881.

28. L.P. Zawada, L. Butkus, and G.A. Hartman, *Ceram. Eng. Sci. Proc.*, **11** (1992) 1592.

29. **Flexural Strength of High Performance Ceramics at Ambient Temperature**, MIL-STD-1942(MR), Department of the Army, November, 1983, p. 1.

30. E. Lara-Curzio, private communication, 1994.

31. E.P. Popov, **Mechanics of Materials**, Prentice-Hall, Englewood Cliffs, NJ, 1976, p. 122.

32. P.S. Steif and A. Trojnacki, *J. Am. Ceram. Soc.*, **77** 1 (1994) 221.

33. P.S. Steif and A. Trojnacki, *Int. J. Solids Structures*, **30** (1993) 1355.

34. P.S. Steif and A. Trojnacki, *Int. J. Solids Structures*, **30** (1993) 1369.

35. H. Murakami, *J. App. Mech.*, **51** (1984) 551.

36. W. Krzys and A. Trojnacki, *Arch. Mech. Engng.*, **36** (1989) 217.

37. W. Krzys and A. Trojnacki, *Arch. Mech. Engng.*, **37** (1990) 5.

38. R.Y. Itani and G.S. Hiremath, *J. Eng. Mech. Div., ASCE*, **106** EM4 (1980) 739.

39. E.G. Thompson, J.R. Goodman, and M.D. Vanderbilt, *J. Str. Div., ASCE*, **101** ST12 (1975) 2659.

40. G.C. Shih and L.J. Ebert, *J. Mater. Sci.*, **21** (1986) 3957.

41. O. Ottinger, M. Gruber, C. Grau, and R.F. Singer, in **High Performance Composites - Commonalty of Phenomena**, K.K. Chawla, P.K. Liaw, and S.G. Fishman (eds.), Warrendale, PA, 1994, p. 275.

42. M.G. Jenkins, J.P. Piccola, M.D. Mello, E. Lara-Curzio, and A.A. Wereszczak, *Ceram. Eng. Sci. Proc.*, **15** (1994) 209.

43. E. Lara-Curzio, private communication, 1994.

44. C. Zweben, W.S. Smith, and M.W. Wardle, in **Composite Materials: Testing and Design (Fifth Conference)**, ASTM STP 674, S.W. Tsai, ed., American Society for Testing Materials, ASTM standard, 1979, p. 228.

45. N.J.-J. Fang and T.-W. Chou, *J. Am. Ceram. Soc.*, **76** (1993) 2539.

46. C.C. Chiao, R.L. Moore, and T.T. Chiao, *Composites*, **8** 3 (1977) 161.

47. K.T. Kedward, *Fibre Sci. Technol.*, **5** (1972) 85.

48. P. Dadras and J.S. McDowell, *Exp. Mech.*, **30** 2 (1990) 184.

49. J.W. Sawyer, Report. No. TM 100647, NASA, September 1988.

50. N. Iosipescu, *J. Mater.*, **2** (1967) 537.

51. D.E. Walrath and D.F. Adams, *J. Compos. Technol. Res.*, **9** 3 (1987) 88.

52. E.M. Odom, D.M. Blackketter, and B.R. Suratno, *Exp. Mech.*, **34** 1 (1994) 10.

53. H. Ho, M.Y. Tsai, J. Morton, and G.L. Farley, *Exp. Mech.*, **34** 1 (1994) 45.

54. COSMOS guide, **Structural Research and Analysis Corporation (SRAC)**, 1992, p. 45.

55. K.H. Huebner and E.A. Thornton, **The Finite Element Method for Engineers**, John Wiley & Sons, New York, 1982, p. 4.

56. E. Lara-Curzio and N. Chawla, unpublished work, 1994.

57 R.A. Lowden, private communication, 1993.

58. J.J. Mecholsky, S.W. Freiman, and R.W. Rice, *J. Mater. Sci.*, **11** (1976) 1310.

59. J.J. Mecholsky, S.W. Freiman, and S.M. Morey, in **Fiber Optics: Advances in Research and Development**, B. Bendow and S.S. Mitra (eds.), Plenum Publishing Co., NY, 1979, p. 187.

60. D. Singh and J.P. Singh, *Ceram. Eng. Sci. Proc.*, **13** (1992) 257.

61. P.A. Brondsted, F.E. Heredia, and A.G. Evans, *J. Am. Ceram. Soc.*, in press.

62. A.G. Evans, J.-M. Domergue, and E. Vagaggini, *J. Am. Ceram. Soc.*, **77** 6 (1994) 1425.

63. C. Cho, J.W. Holmes, and J.R. Barber, *J. Am. Ceram. Soc.*, **74** 11 (1991) 2801.

APPENDIX

FEM convergence plots, meshes, and session files

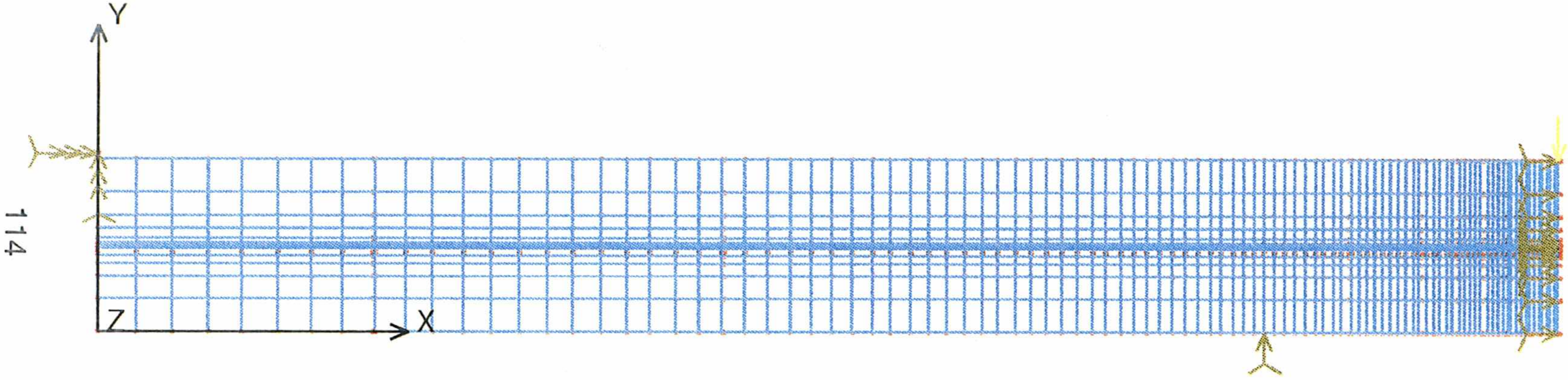

Figure A1. Finite element meshes used to determine solution convergence: (a) mesh #1.

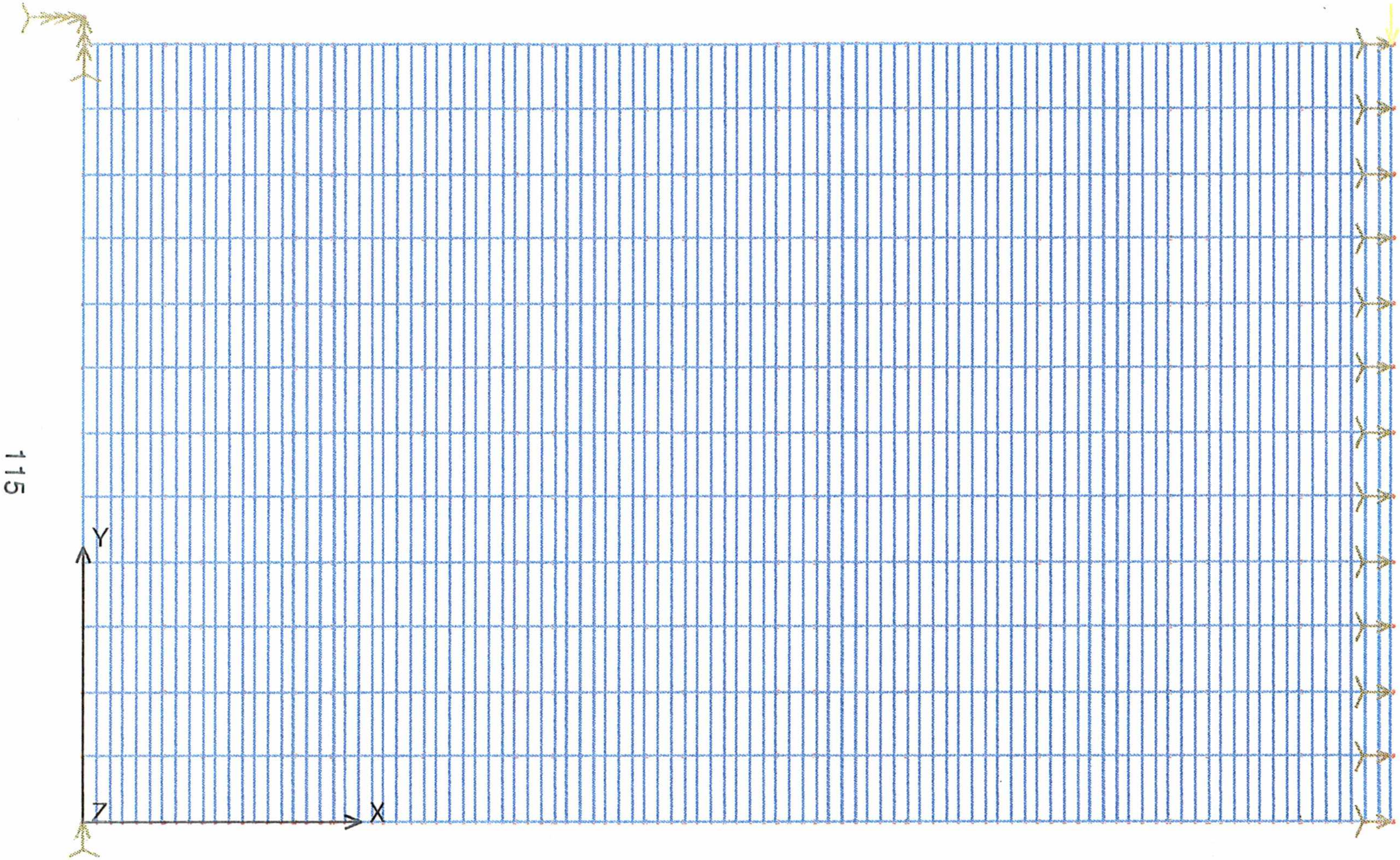

Figure A1. Finite element meshes used to determine solution convergence: (b) mesh #2.

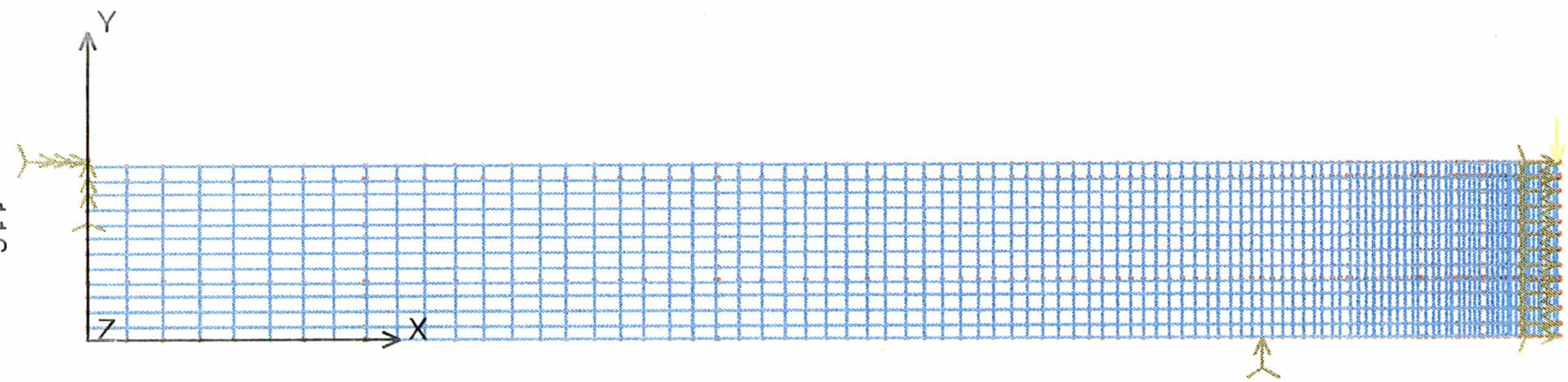

Figure A1. Finite element meshes used to determine solution convergence: (c), mesh #3.

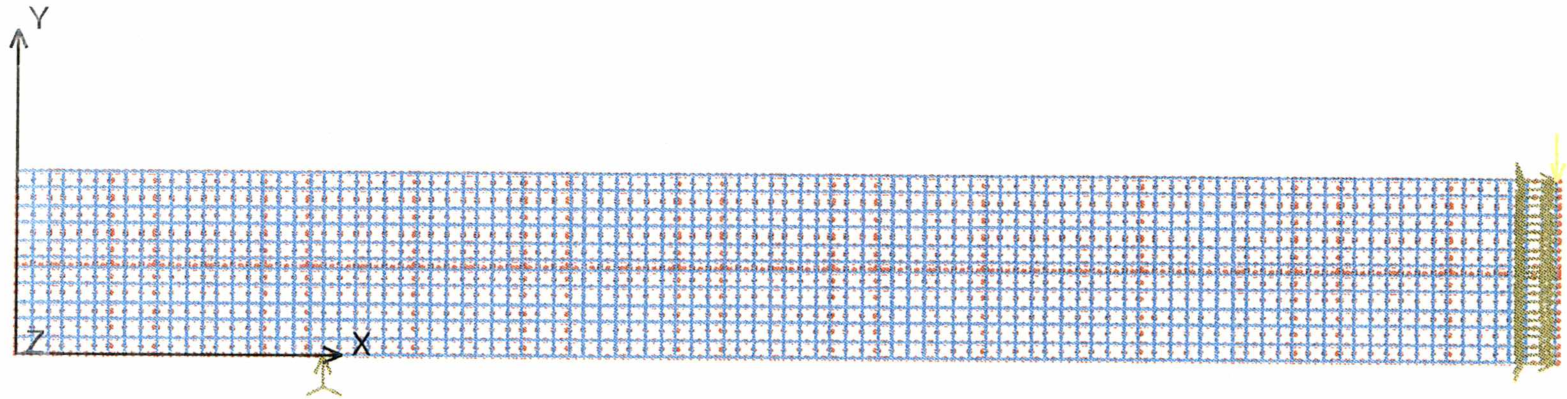

Figure A1. Finite element meshes used to determine solution convergence: (d) regular mesh or mesh used.

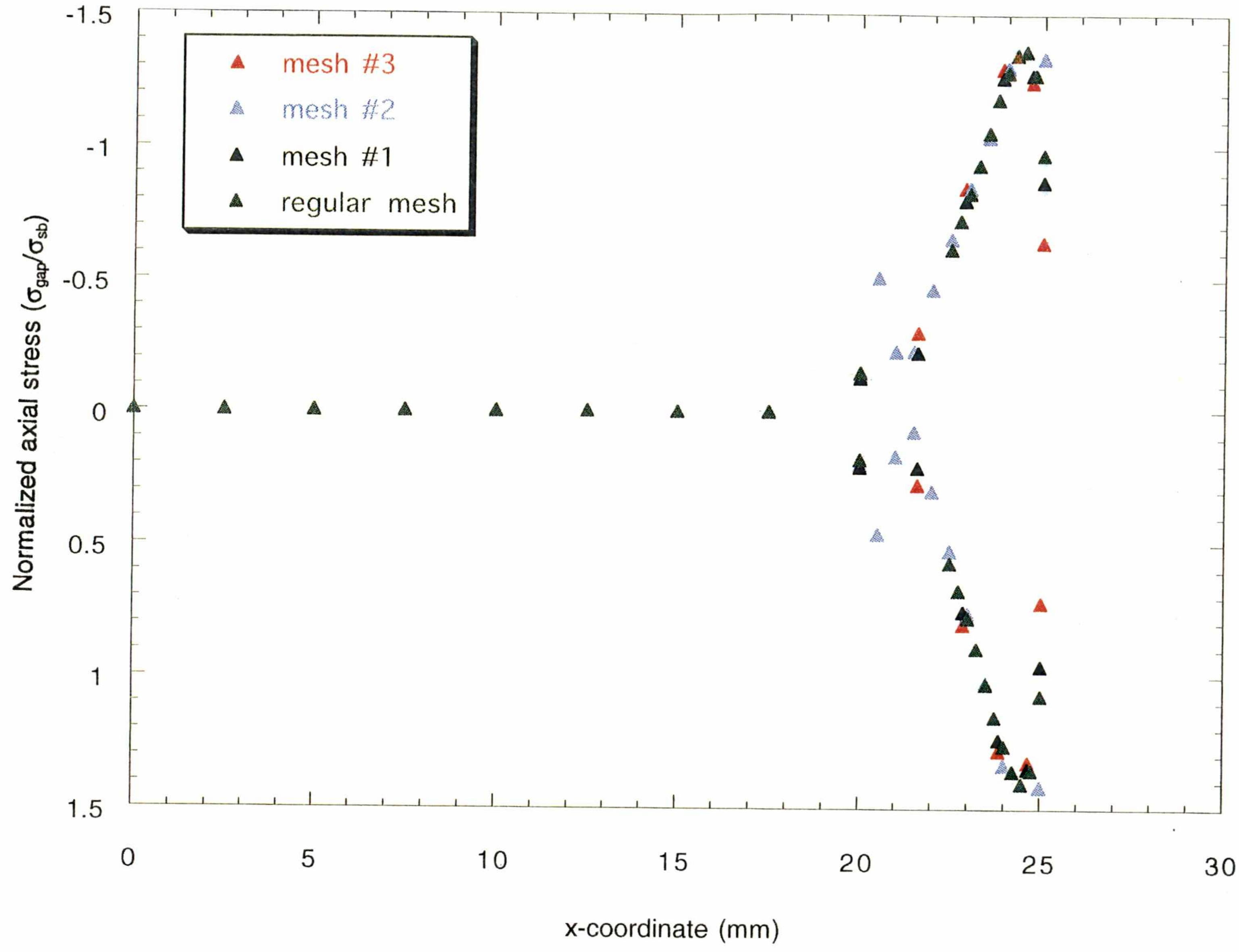

Figure A2. Normalized stress distributions, for a variety of meshes, at the interface of a two-layered beam of aspect ratio 1.67.

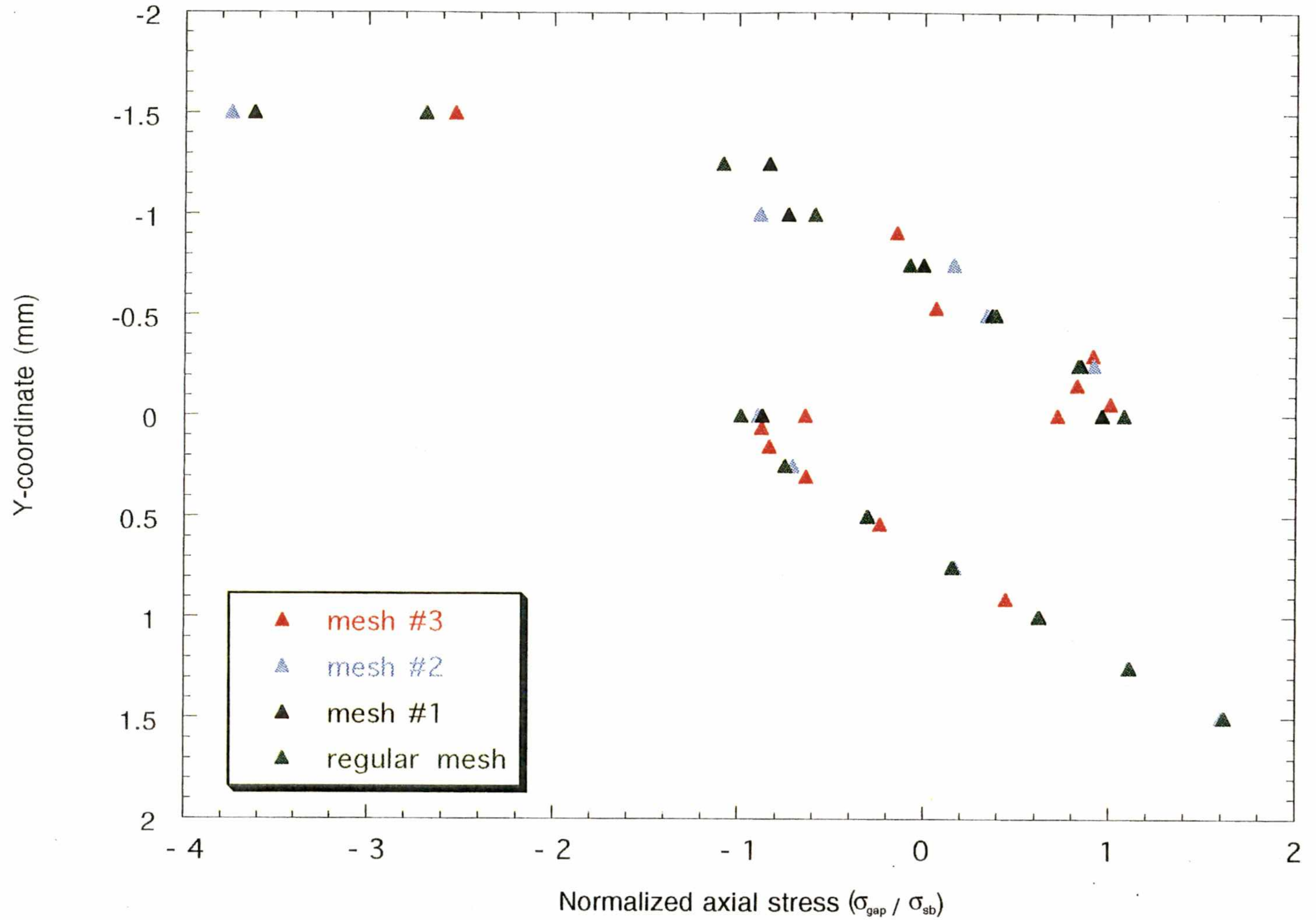

Figure A3. Normalized stress distributions, for a variety of meshes, as a function of distance from the neutral axis of a two-layered beam of aspect ratio 1.67.

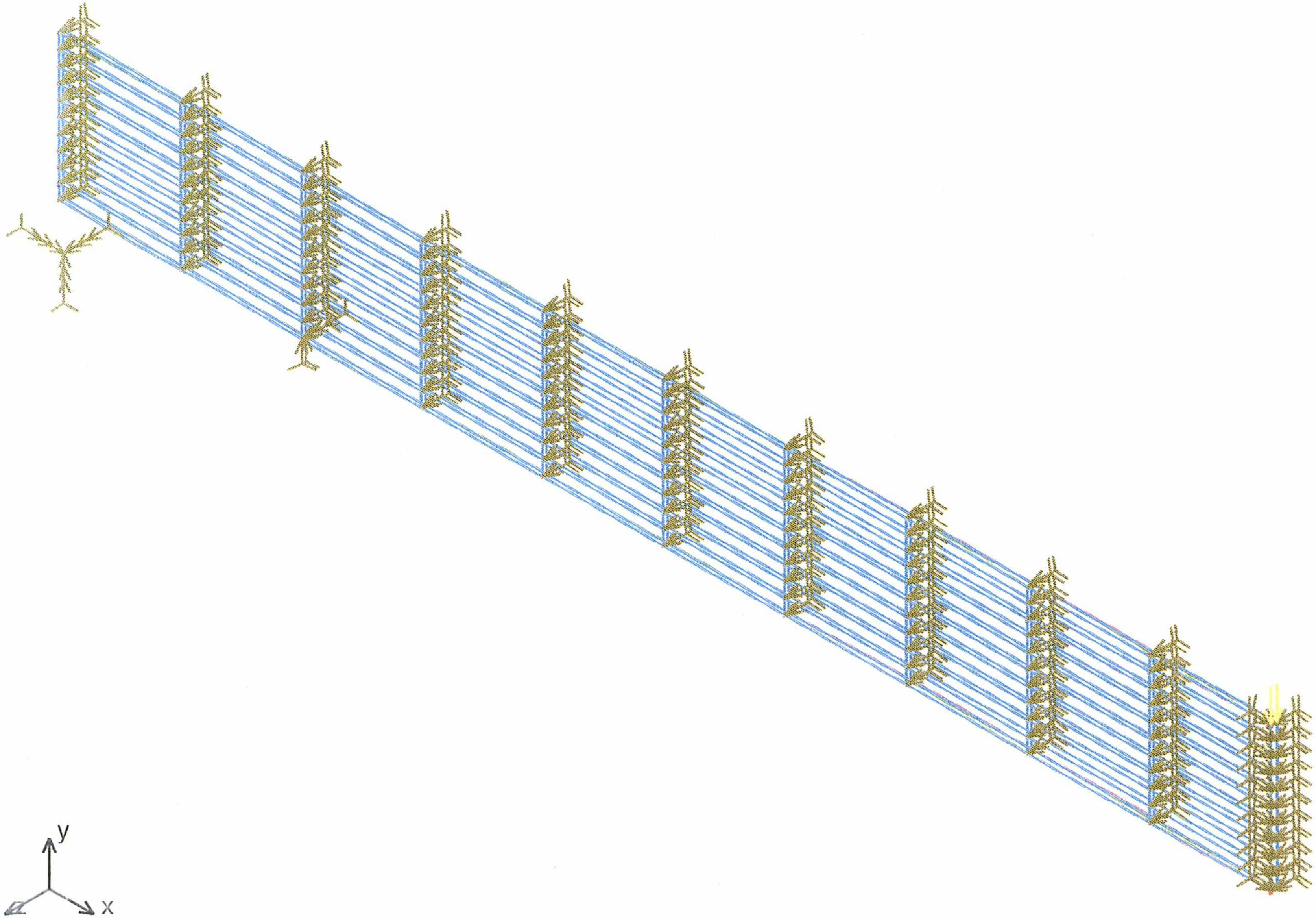

Figure A4. Finite element mesh used to model edge-on orientation.

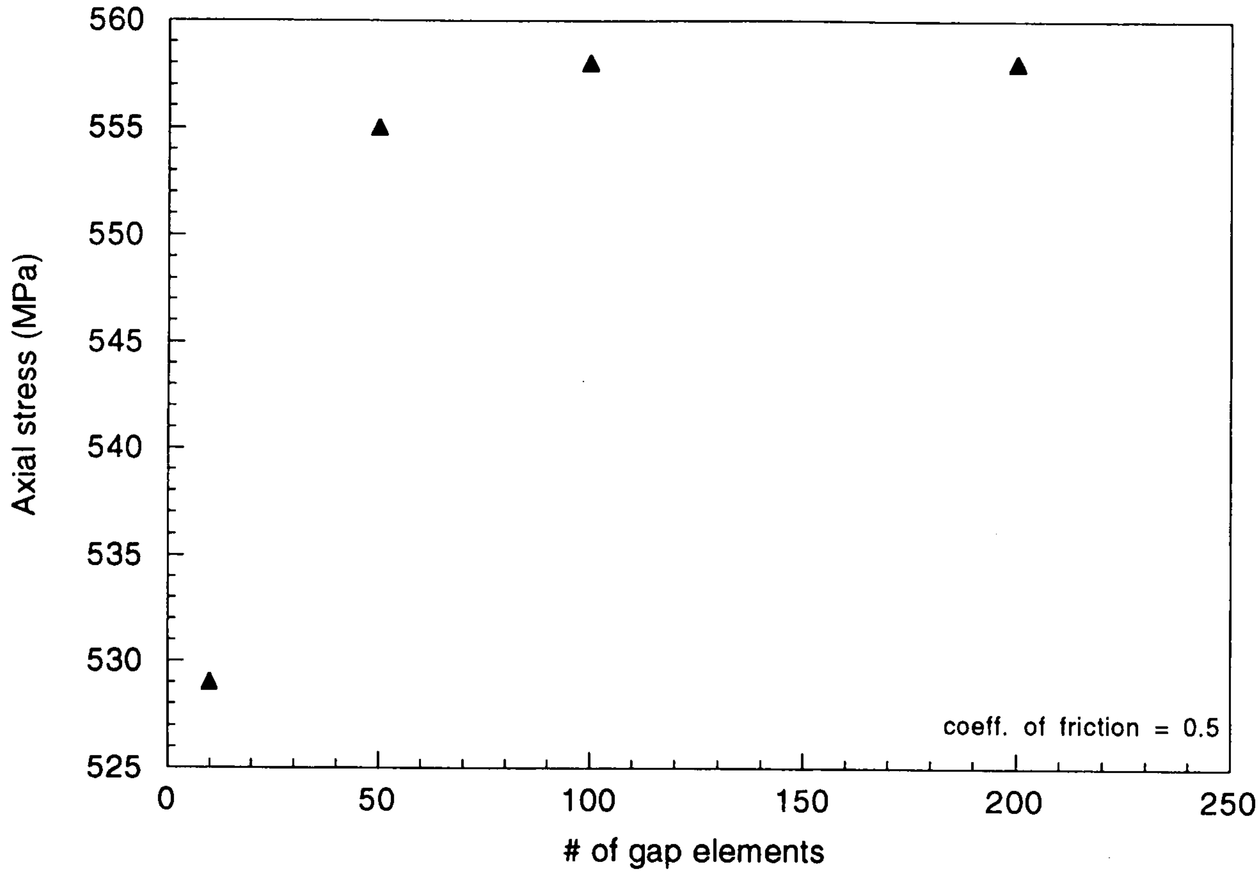

Figure A5. Convergence plot of axial stress versus number of gap elements.

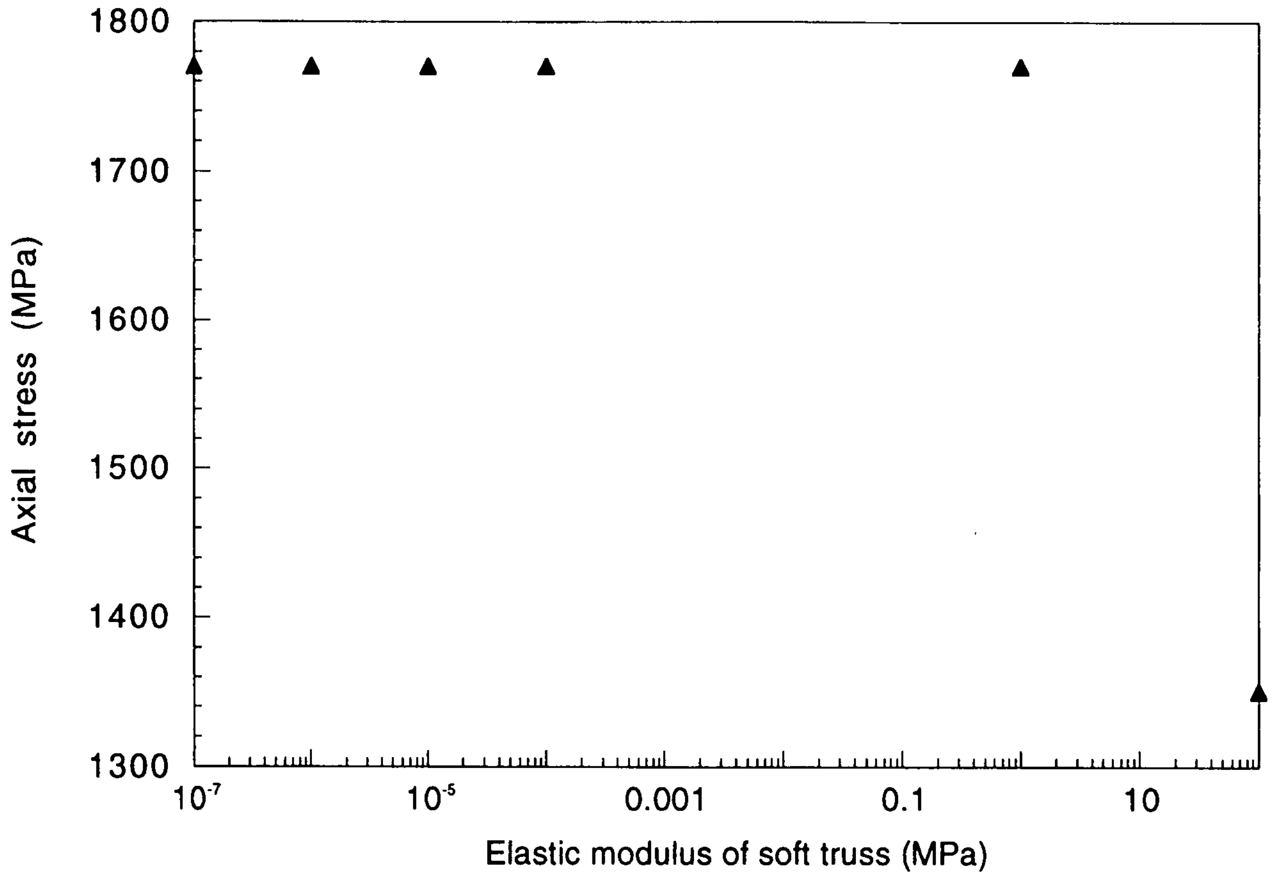

Figure A6. Convergence plot of axial stress versus elastic modulus of soft truss.

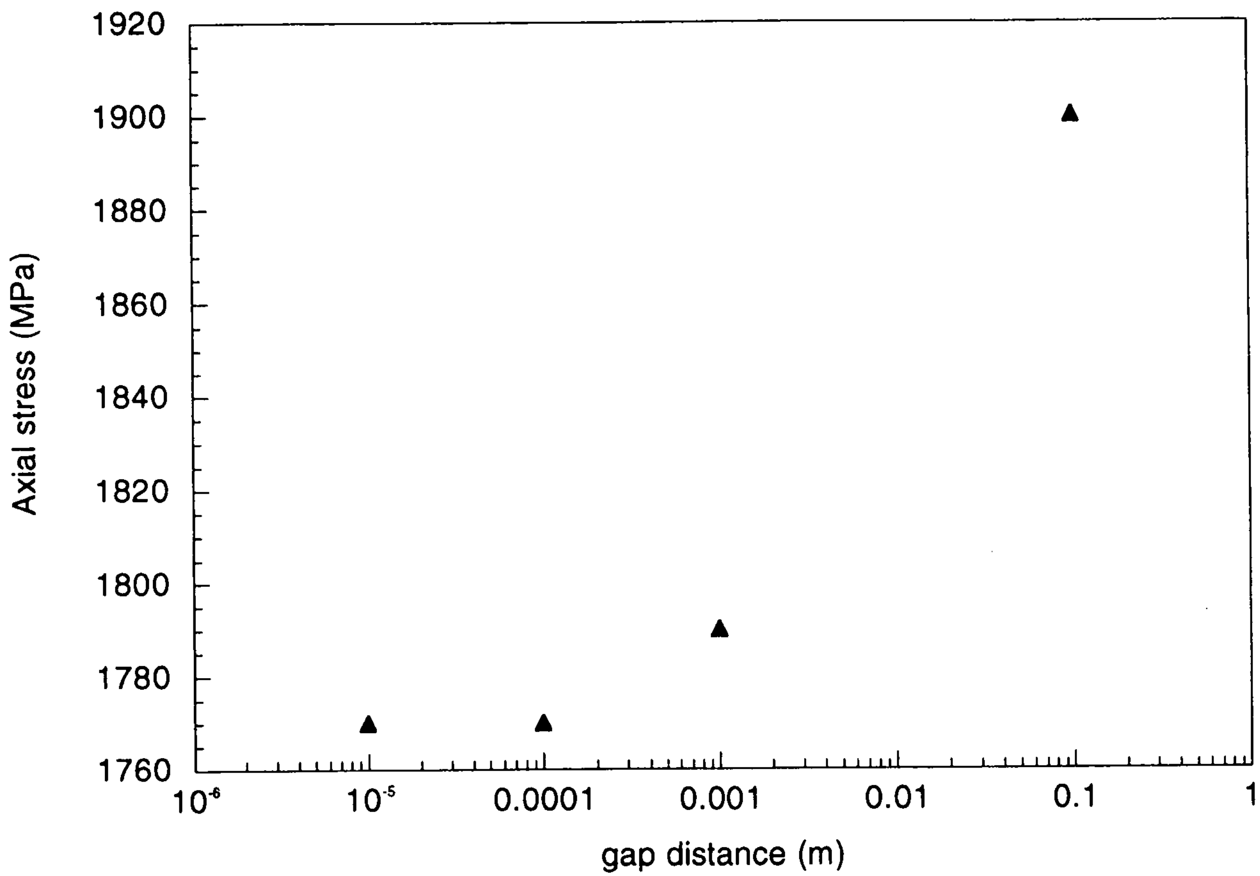

Figure A7. Convergence plot of axial stress versus gap distance.

```
C* Compliant layer analysis.  Two composite surfaces bonded by a compliant
C* layer
C* Points defining two surfaces (x,y,z coordinates)
PT 1 0 0 0
PT 2 0.025 0 0
SCALE 0
VIEW 0 0 1 0
PT 3 0.025 0.001425 0
PT 4 0 0.001425 0
PT 5 0.025 0.001575 0
PT 6 0 0.001575 0
PT 7 0.025 0.003 0
PT 8 0 0.003 0

C* Formation of surfaces
SF4PT 1 1 2 3 4 0
SF4PT 2 4 3 5 6 0
SF4PT 3 6 5 7 8 0

C* Surfaces defined as 2 dimensional planes
EGROUP 1 PLANE2D 0 1 0 0 0 0 0

C* Thickness of surfaces is 1.5 mm
RCONST 1 1 1 2 0.0015 0

C*  Material properties of surfaces
MPROP 1 EX 100E9 NUXY 0.3

C* Meshing of surfaces using 8 noded, 100X5 elements, with equal spacing
M_SF 1 1 1 8 100 5 1 1
M_SF 3 3 1 8 100 5 1 1

C* Material properties of compliant layer
MPROP 2 EX 50E9 NUXY 0.3

C* Meshing of compliant layer surface
M_SF 2 2 1 8 100 1 1 1

C* Merging of nodes
NMERGE 1 3925 1 0.00000001 0 1 0

C* Constrainment of nodes
DND 41 UY 0 41 1
DCR 4 UX 0 4 1
DCR 10 UX 0 10 1
DCR 7 UX 0 7 1

C* Application of force
FND 3422 FY -100 3422 1
```
Figure A8. Session file for compliant layer analysis of transverse orientation.

```
C* Transverse model.  Two surfaces perpendicular to the loading direction
C* bonded by gap elements with a given coefficient of friction.
C* Points defining two surfaces (x,y,z coordinates)
PT 1 0 0 0
PT 2 25 0 0
SCALE 0
VIEW 0 0 1 0
PT 3 25 1.49995 0
PT 4 0 1.49995 0
PT 5 25 1.50005 0
PT 6 0 1.50005 0
PT 7 25 3 0
PT 8 0 3 0

C* Formation of surfaces
SF4PT 1 1 2 3 4 0
SF4PT 2 6 5 7 8 0

C* Surfaces defined as 2 dimensional planes
EGROUP 1 PLANE2D 0 1 0 0 0 0 0

C* Thickness of surfaces is 1.5 mm
RCONST 1 1 1 2 1.5 0

C*  Material properties of surfaces
MPROP 1 EX 100E9 NUXY 0.3

C* Meshing of surfaces using 4 noded, 100X6 elements, with equal spacing
M_SF 1 1 1 4 100 6 1 1
M_SF 2 2 1 4 100 6 1 1

C* Gap defined with friction and sliding
EGROUP 2 GAP 1 2 0 0 0 0 0

C* Coefficient of friction is 0.01
RCONST 2 2 1 7 0 0.01 0 0 1E+08 0 1

ACTSET EG 2
ACTSET RC 2

C* Individual gaps are defined as two noded elements
EL 1201 CR 0 3 607 708 1 0 0 0 0 0 0
EL 1202 CR 0 3 608 709 1 0 0 0 0 0 0
EL 1203 CR 0 3 609 710 1 0 0 0 0 0 0
EL 1204 CR 0 3 610 711 1 0 0 0 0 0 0
EL 1205 CR 0 3 611 712 1 0 0 0 0 0 0
EL 1206 CR 0 3 612 713 1 0 0 0 0 0 0
EL 1207 CR 0 3 613 714 1 0 0 0 0 0 0
EL 1208 CR 0 3 614 715 1 0 0 0 0 0 0
```

Figure A9. Session file for gap element analysis of transverse orientation.

EL 1209 CR 0 3 615 716 1 0 0 0 0 0 0
EL 1210 CR 0 3 616 717 1 0 0 0 0 0 0
EL 1211 CR 0 3 617 718 1 0 0 0 0 0 0
EL 1212 CR 0 3 618 719 1 0 0 0 0 0 0
EL 1213 CR 0 3 619 720 1 0 0 0 0 0 0
EL 1214 CR 0 3 620 721 1 0 0 0 0 0 0
EL 1215 CR 0 3 621 722 1 0 0 0 0 0 0
EL 1216 CR 0 3 622 723 1 0 0 0 0 0 0
EL 1217 CR 0 3 623 724 1 0 0 0 0 0 0
EL 1218 CR 0 3 624 725 1 0 0 0 0 0 0
EL 1219 CR 0 3 625 726 1 0 0 0 0 0 0
EL 1220 CR 0 3 626 727 1 0 0 0 0 0 0
EL 1221 CR 0 3 627 728 1 0 0 0 0 0 0
EL 1222 CR 0 3 628 729 1 0 0 0 0 0 0
EL 1223 CR 0 3 629 730 1 0 0 0 0 0 0
EL 1224 CR 0 3 630 731 1 0 0 0 0 0 0
EL 1225 CR 0 3 631 732 1 0 0 0 0 0 0
EL 1226 CR 0 3 632 733 1 0 0 0 0 0 0
EL 1227 CR 0 3 633 734 1 0 0 0 0 0 0
EL 1228 CR 0 3 634 735 1 0 0 0 0 0 0
EL 1229 CR 0 3 635 736 1 0 0 0 0 0 0
EL 1230 CR 0 3 636 737 1 0 0 0 0 0 0
EL 1231 CR 0 3 637 738 1 0 0 0 0 0 0
EL 1232 CR 0 3 638 739 1 0 0 0 0 0 0
EL 1233 CR 0 3 639 740 1 0 0 0 0 0 0
EL 1234 CR 0 3 640 741 1 0 0 0 0 0 0
EL 1235 CR 0 3 641 742 1 0 0 0 0 0 0
EL 1236 CR 0 3 642 743 1 0 0 0 0 0 0
EL 1237 CR 0 3 643 744 1 0 0 0 0 0 0
EL 1238 CR 0 3 644 745 1 0 0 0 0 0 0
EL 1239 CR 0 3 645 746 1 0 0 0 0 0 0
EL 1240 CR 0 3 646 747 1 0 0 0 0 0 0
EL 1241 CR 0 3 647 748 1 0 0 0 0 0 0
EL 1242 CR 0 3 648 749 1 0 0 0 0 0 0
EL 1243 CR 0 3 649 750 1 0 0 0 0 0 0
EL 1244 CR 0 3 650 751 1 0 0 0 0 0 0
EL 1245 CR 0 3 651 752 1 0 0 0 0 0 0
EL 1246 CR 0 3 652 753 1 0 0 0 0 0 0
EL 1247 CR 0 3 653 754 1 0 0 0 0 0 0
EL 1248 CR 0 3 654 755 1 0 0 0 0 0 0
EL 1249 CR 0 3 655 756 1 0 0 0 0 0 0
EL 1250 CR 0 3 656 757 1 0 0 0 0 0 0
EL 1251 CR 0 3 657 758 1 0 0 0 0 0 0
EL 1252 CR 0 3 658 759 1 0 0 0 0 0 0
EL 1253 CR 0 3 659 760 1 0 0 0 0 0 0
EL 1254 CR 0 3 660 761 1 0 0 0 0 0 0
EL 1255 CR 0 3 661 762 1 0 0 0 0 0 0
EL 1256 CR 0 3 662 763 1 0 0 0 0 0 0
EL 1257 CR 0 3 663 764 1 0 0 0 0 0 0

```
EL 1258 CR 0 3 664 765 1 0 0 0 0 0 0
EL 1259 CR 0 3 665 766 1 0 0 0 0 0 0
EL 1260 CR 0 3 666 767 1 0 0 0 0 0 0
EL 1261 CR 0 3 667 768 1 0 0 0 0 0 0
EL 1262 CR 0 3 668 769 1 0 0 0 0 0 0
EL 1263 CR 0 3 669 770 1 0 0 0 0 0 0
EL 1264 CR 0 3 670 771 1 0 0 0 0 0 0
EL 1265 CR 0 3 671 772 1 0 0 0 0 0 0
EL 1266 CR 0 3 672 773 1 0 0 0 0 0 0
EL 1267 CR 0 3 673 774 1 0 0 0 0 0 0
EL 1268 CR 0 3 674 775 1 0 0 0 0 0 0
EL 1269 CR 0 3 675 776 1 0 0 0 0 0 0
EL 1270 CR 0 3 676 777 1 0 0 0 0 0 0
EL 1271 CR 0 3 677 778 1 0 0 0 0 0 0
EL 1272 CR 0 3 678 779 1 0 0 0 0 0 0
EL 1273 CR 0 3 679 780 1 0 0 0 0 0 0
EL 1274 CR 0 3 680 781 1 0 0 0 0 0 0
EL 1275 CR 0 3 681 782 1 0 0 0 0 0 0
EL 1276 CR 0 3 682 783 1 0 0 0 0 0 0
EL 1277 CR 0 3 683 784 1 0 0 0 0 0 0
EL 1278 CR 0 3 684 785 1 0 0 0 0 0 0
EL 1279 CR 0 3 685 786 1 0 0 0 0 0 0
EL 1280 CR 0 3 686 787 1 0 0 0 0 0 0
EL 1281 CR 0 3 687 788 1 0 0 0 0 0 0
EL 1282 CR 0 3 688 789 1 0 0 0 0 0 0
EL 1283 CR 0 3 689 790 1 0 0 0 0 0 0
EL 1284 CR 0 3 690 791 1 0 0 0 0 0 0
EL 1285 CR 0 3 691 792 1 0 0 0 0 0 0
EL 1286 CR 0 3 692 793 1 0 0 0 0 0 0
EL 1287 CR 0 3 693 794 1 0 0 0 0 0 0
EL 1288 CR 0 3 694 795 1 0 0 0 0 0 0
EL 1289 CR 0 3 695 796 1 0 0 0 0 0 0
EL 1290 CR 0 3 696 797 1 0 0 0 0 0 0
EL 1291 CR 0 3 697 798 1 0 0 0 0 0 0
EL 1292 CR 0 3 698 799 1 0 0 0 0 0 0
EL 1293 CR 0 3 699 800 1 0 0 0 0 0 0
EL 1294 CR 0 3 700 801 1 0 0 0 0 0 0
EL 1295 CR 0 3 701 802 1 0 0 0 0 0 0
EL 1296 CR 0 3 702 803 1 0 0 0 0 0 0
EL 1297 CR 0 3 703 804 1 0 0 0 0 0 0
EL 1298 CR 0 3 704 805 1 0 0 0 0 0 0
EL 1299 CR 0 3 705 806 1 0 0 0 0 0 0
EL 1300 CR 0 3 706 807 1 0 0 0 0 0 0
EL 1301 CR 0 3 707 808 1 0 0 0 0 0 0

C* Definition of "soft" two-dimensional trusses
EGROUP 3 TRUSS2D 0 0 0 0 0 0 0
RCONST 3 3 1 2 0.01 0
```

```
C* Material property of truss
MPROP 3 EX 1e1

C* Soft truss element
ND 1415 25 -0.1 0.00 0 0 0 0 0 0
EL 1302 CR 0 2 1415 101 0 0 0 0 0 0

C* Constrainment of nodes
DND 1415 AL 0 1415 1
DND 21 UY 0 21 1
DCR 8 UX 0 8 1
DCR 4 UX 0 4 1
SCALE 0

C* Loading times and load-time curve definition
ACTSET TC 1
TIMES 0 5 1
CURDEF TIME 1 1 0 0 5 1E+08

C* Application of force
FND 1414 FY -1 1414 1
NL_NRESP 1 101 0
```

```
C* Edge-on model. Two surfaces parallel to loading direction connected by
C* gap elements
C* Points defining two surfaces (x,y,z coordinates)

PT 1 0 0 0
PT 2 0 3 0
PT 3 25 3 0
PT 4 25 0 0
SCALE 0
PT 5 0 0 0.1
PT 6 0 3 0.1
PT 7 25 3 0.1
PT 8 25 0 0.1

C* Formation of surfaces

SF4PT 1 1 2 3 4 0
SF4PT 2 5 6 7 8 0

C* Surfaces defined as shell surfaces with 1.5 mm thickness
EGROUP 1 SHELL4 1 0 0 0 0 0 0
RCONST 1 1 1 6 1.5 0 0 0 0 0

C* Material properties of surfaces
MPROP 1 EX 100E9 NUXY 0.3

C* Meshing of surfaces using 4 noded, 10X10 elements, with equal spacing
M_SF 1 1 1 4 10 10 1 1
M_SF 2 2 1 4 10 10 1 1

C* Gap defined with friction and sliding
EGROUP 2 GAP 1 2 1 0 0 0 0

C* Coefficient of friction is 0.01
RCONST 2 2 1 7 0 0.1 0 0 1E+08 0 1
ND 1011 0 -1 0 0 0 0 0 0 0

C* Individual gaps are defined as two noded elements
EL 201 CR 0 3 122 1 1011 0 0 0 0 0 0
EL 202 CR 0 3 123 2 1011 0 0 0 0 0 0
EL 203 CR 0 3 124 3 1011 0 0 0 0 0 0
EL 204 CR 0 3 125 4 1011 0 0 0 0 0 0
EL 205 CR 0 3 126 5 1011 0 0 0 0 0 0
EL 206 CR 0 3 127 6 1011 0 0 0 0 0 0
EL 207 CR 0 3 128 7 1011 0 0 0 0 0 0
EL 208 CR 0 3 129 8 1011 0 0 0 0 0 0
EL 209 CR 0 3 130 9 1011 0 0 0 0 0 0
EL 210 CR 0 3 131 10 1011 0 0 0 0 0 0
EL 211 CR 0 3 132 11 1011 0 0 0 0 0 0
```

Figure A10. Session file for analysis of edge-on orientation.

EL 212 CR 0 3 133 12 1011 0 0 0 0 0 0
EL 213 CR 0 3 134 13 1011 0 0 0 0 0 0
EL 214 CR 0 3 135 14 1011 0 0 0 0 0 0
EL 215 CR 0 3 136 15 1011 0 0 0 0 0 0
EL 216 CR 0 3 137 16 1011 0 0 0 0 0 0
EL 217 CR 0 3 138 17 1011 0 0 0 0 0 0
EL 218 CR 0 3 139 18 1011 0 0 0 0 0 0
EL 219 CR 0 3 140 19 1011 0 0 0 0 0 0
EL 220 CR 0 3 141 20 1011 0 0 0 0 0 0
EL 221 CR 0 3 142 21 1011 0 0 0 0 0 0
EL 222 CR 0 3 143 22 1011 0 0 0 0 0 0
EL 223 CR 0 3 144 23 1011 0 0 0 0 0 0
EL 224 CR 0 3 145 24 1011 0 0 0 0 0 0
EL 225 CR 0 3 146 25 1011 0 0 0 0 0 0
EL 226 CR 0 3 147 26 1011 0 0 0 0 0 0
EL 227 CR 0 3 148 27 1011 0 0 0 0 0 0
EL 228 CR 0 3 149 28 1011 0 0 0 0 0 0
EL 229 CR 0 3 150 29 1011 0 0 0 0 0 0
EL 230 CR 0 3 151 30 1011 0 0 0 0 0 0
EL 231 CR 0 3 152 31 1011 0 0 0 0 0 0
EL 232 CR 0 3 153 32 1011 0 0 0 0 0 0
EL 233 CR 0 3 154 33 1011 0 0 0 0 0 0
EL 234 CR 0 3 155 34 1011 0 0 0 0 0 0
EL 235 CR 0 3 156 35 1011 0 0 0 0 0 0
EL 236 CR 0 3 157 36 1011 0 0 0 0 0 0
EL 237 CR 0 3 158 37 1011 0 0 0 0 0 0
EL 238 CR 0 3 159 38 1011 0 0 0 0 0 0
EL 239 CR 0 3 160 39 1011 0 0 0 0 0 0
EL 240 CR 0 3 161 40 1011 0 0 0 0 0 0
EL 241 CR 0 3 162 41 1011 0 0 0 0 0 0
EL 242 CR 0 3 163 42 1011 0 0 0 0 0 0
EL 243 CR 0 3 164 43 1011 0 0 0 0 0 0
EL 244 CR 0 3 165 44 1011 0 0 0 0 0 0
EL 245 CR 0 3 166 45 1011 0 0 0 0 0 0
EL 246 CR 0 3 167 46 1011 0 0 0 0 0 0
EL 247 CR 0 3 168 47 1011 0 0 0 0 0 0
EL 248 CR 0 3 169 48 1011 0 0 0 0 0 0
EL 249 CR 0 3 170 49 1011 0 0 0 0 0 0
EL 250 CR 0 3 171 50 1011 0 0 0 0 0 0
EL 251 CR 0 3 172 51 1011 0 0 0 0 0 0
EL 252 CR 0 3 173 52 1011 0 0 0 0 0 0
EL 253 CR 0 3 174 53 1011 0 0 0 0 0 0
EL 254 CR 0 3 175 54 1011 0 0 0 0 0 0
EL 255 CR 0 3 176 55 1011 0 0 0 0 0 0
EL 256 CR 0 3 177 56 1011 0 0 0 0 0 0
EL 257 CR 0 3 178 57 1011 0 0 0 0 0 0
EL 258 CR 0 3 179 58 1011 0 0 0 0 0 0
EL 259 CR 0 3 180 59 1011 0 0 0 0 0 0
EL 260 CR 0 3 181 60 1011 0 0 0 0 0 0

EL 261 CR 0 3 182 61 1011 0 0 0 0 0 0
EL 262 CR 0 3 183 62 1011 0 0 0 0 0 0
EL 263 CR 0 3 184 63 1011 0 0 0 0 0 0
EL 264 CR 0 3 185 64 1011 0 0 0 0 0 0
EL 265 CR 0 3 186 65 1011 0 0 0 0 0 0
EL 266 CR 0 3 187 66 1011 0 0 0 0 0 0
EL 267 CR 0 3 188 67 1011 0 0 0 0 0 0
EL 268 CR 0 3 189 68 1011 0 0 0 0 0 0
EL 269 CR 0 3 190 69 1011 0 0 0 0 0 0
EL 270 CR 0 3 191 70 1011 0 0 0 0 0 0
EL 271 CR 0 3 192 71 1011 0 0 0 0 0 0
EL 272 CR 0 3 193 72 1011 0 0 0 0 0 0
EL 273 CR 0 3 194 73 1011 0 0 0 0 0 0
EL 274 CR 0 3 195 74 1011 0 0 0 0 0 0
EL 275 CR 0 3 196 75 1011 0 0 0 0 0 0
EL 276 CR 0 3 197 76 1011 0 0 0 0 0 0
EL 277 CR 0 3 198 77 1011 0 0 0 0 0 0
EL 278 CR 0 3 199 78 1011 0 0 0 0 0 0
EL 279 CR 0 3 200 79 1011 0 0 0 0 0 0
EL 280 CR 0 3 201 80 1011 0 0 0 0 0 0
EL 281 CR 0 3 202 81 1011 0 0 0 0 0 0
EL 282 CR 0 3 203 82 1011 0 0 0 0 0 0
EL 283 CR 0 3 204 83 1011 0 0 0 0 0 0
EL 284 CR 0 3 205 84 1011 0 0 0 0 0 0
EL 285 CR 0 3 206 85 1011 0 0 0 0 0 0
EL 286 CR 0 3 207 86 1011 0 0 0 0 0 0
EL 287 CR 0 3 208 87 1011 0 0 0 0 0 0
EL 288 CR 0 3 209 88 1011 0 0 0 0 0 0
EL 289 CR 0 3 210 89 1011 0 0 0 0 0 0
EL 290 CR 0 3 211 90 1011 0 0 0 0 0 0
EL 291 CR 0 3 212 91 1011 0 0 0 0 0 0
EL 292 CR 0 3 213 92 1011 0 0 0 0 0 0
EL 293 CR 0 3 214 93 1011 0 0 0 0 0 0
EL 294 CR 0 3 215 94 1011 0 0 0 0 0 0
EL 295 CR 0 3 216 95 1011 0 0 0 0 0 0
EL 296 CR 0 3 217 96 1011 0 0 0 0 0 0
EL 297 CR 0 3 218 97 1011 0 0 0 0 0 0
EL 298 CR 0 3 219 98 1011 0 0 0 0 0 0
EL 299 CR 0 3 220 99 1011 0 0 0 0 0 0
EL 300 CR 0 3 221 100 1011 0 0 0 0 0 0
EL 301 CR 0 3 222 101 1011 0 0 0 0 0 0
EL 302 CR 0 3 223 102 1011 0 0 0 0 0 0
EL 303 CR 0 3 224 103 1011 0 0 0 0 0 0
EL 304 CR 0 3 225 104 1011 0 0 0 0 0 0
EL 305 CR 0 3 226 105 1011 0 0 0 0 0 0
EL 306 CR 0 3 227 106 1011 0 0 0 0 0 0
EL 307 CR 0 3 228 107 1011 0 0 0 0 0 0
EL 308 CR 0 3 229 108 1011 0 0 0 0 0 0
EL 309 CR 0 3 230 109 1011 0 0 0 0 0 0

```
EL 310 CR 0 3 231 110 1011 0 0 0 0 0 0
EL 311 CR 0 3 232 111 1011 0 0 0 0 0 0
EL 312 CR 0 3 233 112 1011 0 0 0 0 0 0
EL 313 CR 0 3 234 113 1011 0 0 0 0 0 0
EL 314 CR 0 3 235 114 1011 0 0 0 0 0 0
EL 315 CR 0 3 236 115 1011 0 0 0 0 0 0
EL 316 CR 0 3 237 116 1011 0 0 0 0 0 0
EL 317 CR 0 3 238 117 1011 0 0 0 0 0 0
EL 318 CR 0 3 239 118 1011 0 0 0 0 0 0
EL 319 CR 0 3 240 119 1011 0 0 0 0 0 0
EL 320 CR 0 3 241 120 1011 0 0 0 0 0 0
EL 321 CR 0 3 242 121 1011 0 0 0 0 0 0

C* Definition of "soft" two-dimensional trusses
EGROUP 3 TRUSS2D 0 0 0 0 0 0 0
RCONST 3 3 1 2 0.01 0

C* Material property of truss
MPROP 2 EX 1E1

C* Soft truss elements at each gap location to stabilize structure
EL 322 CR 0 2 122 1 0 0 0 0 0 0
EL 323 CR 0 2 123 2 0 0 0 0 0 0
EL 324 CR 0 2 124 3 0 0 0 0 0 0
EL 325 CR 0 2 125 4 0 0 0 0 0 0
EL 326 CR 0 2 126 5 0 0 0 0 0 0
EL 327 CR 0 2 127 6 0 0 0 0 0 0
EL 328 CR 0 2 128 7 0 0 0 0 0 0
EL 329 CR 0 2 129 8 0 0 0 0 0 0
EL 330 CR 0 2 130 9 0 0 0 0 0 0
EL 331 CR 0 2 131 10 0 0 0 0 0 0
EL 332 CR 0 2 132 11 0 0 0 0 0 0
EL 333 CR 0 2 133 12 0 0 0 0 0 0
EL 334 CR 0 2 134 13 0 0 0 0 0 0
EL 335 CR 0 2 135 14 0 0 0 0 0 0
EL 336 CR 0 2 136 15 0 0 0 0 0 0
EL 337 CR 0 2 137 16 0 0 0 0 0 0
EL 338 CR 0 2 138 17 0 0 0 0 0 0
EL 339 CR 0 2 139 18 0 0 0 0 0 0
EL 340 CR 0 2 140 19 0 0 0 0 0 0
EL 341 CR 0 2 141 20 0 0 0 0 0 0
EL 342 CR 0 2 142 21 0 0 0 0 0 0
EL 343 CR 0 2 143 22 0 0 0 0 0 0
EL 344 CR 0 2 144 23 0 0 0 0 0 0
EL 345 CR 0 2 145 24 0 0 0 0 0 0
EL 346 CR 0 2 146 25 0 0 0 0 0 0
EL 347 CR 0 2 147 26 0 0 0 0 0 0
EL 348 CR 0 2 148 27 0 0 0 0 0 0
EL 349 CR 0 2 149 28 0 0 0 0 0 0
```

EL 350 CR 0 2 150 29 0 0 0 0 0 0
EL 351 CR 0 2 151 30 0 0 0 0 0 0
EL 352 CR 0 2 152 31 0 0 0 0 0 0
EL 353 CR 0 2 153 32 0 0 0 0 0 0
EL 354 CR 0 2 154 33 0 0 0 0 0 0
EL 355 CR 0 2 155 34 0 0 0 0 0 0
EL 356 CR 0 2 156 35 0 0 0 0 0 0
EL 357 CR 0 2 157 36 0 0 0 0 0 0
EL 358 CR 0 2 158 37 0 0 0 0 0 0
EL 359 CR 0 2 159 38 0 0 0 0 0 0
EL 360 CR 0 2 160 39 0 0 0 0 0 0
EL 361 CR 0 2 161 40 0 0 0 0 0 0
EL 362 CR 0 2 162 41 0 0 0 0 0 0
EL 363 CR 0 2 163 42 0 0 0 0 0 0
EL 364 CR 0 2 164 43 0 0 0 0 0 0
EL 365 CR 0 2 165 44 0 0 0 0 0 0
EL 366 CR 0 2 166 45 0 0 0 0 0 0
EL 367 CR 0 2 167 46 0 0 0 0 0 0
EL 368 CR 0 2 168 47 0 0 0 0 0 0
EL 369 CR 0 2 169 48 0 0 0 0 0 0
EL 370 CR 0 2 170 49 0 0 0 0 0 0
EL 371 CR 0 2 171 50 0 0 0 0 0 0
EL 372 CR 0 2 172 51 0 0 0 0 0 0
EL 373 CR 0 2 173 52 0 0 0 0 0 0
EL 374 CR 0 2 174 53 0 0 0 0 0 0
EL 375 CR 0 2 175 54 0 0 0 0 0 0
EL 376 CR 0 2 176 55 0 0 0 0 0 0
EL 377 CR 0 2 177 56 0 0 0 0 0 0
EL 378 CR 0 2 178 57 0 0 0 0 0 0
EL 379 CR 0 2 179 58 0 0 0 0 0 0
EL 380 CR 0 2 180 59 0 0 0 0 0 0
EL 381 CR 0 2 181 60 0 0 0 0 0 0
EL 382 CR 0 2 182 61 0 0 0 0 0 0
EL 383 CR 0 2 183 62 0 0 0 0 0 0
EL 384 CR 0 2 184 63 0 0 0 0 0 0
EL 385 CR 0 2 185 64 0 0 0 0 0 0
EL 386 CR 0 2 186 65 0 0 0 0 0 0
EL 387 CR 0 2 187 66 0 0 0 0 0 0
EL 388 CR 0 2 188 67 0 0 0 0 0 0
EL 389 CR 0 2 189 68 0 0 0 0 0 0
EL 390 CR 0 2 190 69 0 0 0 0 0 0
EL 391 CR 0 2 191 70 0 0 0 0 0 0
EL 392 CR 0 2 192 71 0 0 0 0 0 0
EL 393 CR 0 2 193 72 0 0 0 0 0 0
EL 394 CR 0 2 194 73 0 0 0 0 0 0
EL 395 CR 0 2 195 74 0 0 0 0 0 0
EL 396 CR 0 2 196 75 0 0 0 0 0 0
EL 397 CR 0 2 197 76 0 0 0 0 0 0
EL 398 CR 0 2 198 77 0 0 0 0 0 0

EL 399 CR 0 2 199 78 0 0 0 0 0 0
EL 400 CR 0 2 200 79 0 0 0 0 0 0
EL 401 CR 0 2 201 80 0 0 0 0 0 0
EL 402 CR 0 2 202 81 0 0 0 0 0 0
EL 403 CR 0 2 203 82 0 0 0 0 0 0
EL 404 CR 0 2 204 83 0 0 0 0 0 0
EL 405 CR 0 2 205 84 0 0 0 0 0 0
EL 406 CR 0 2 206 85 0 0 0 0 0 0
EL 407 CR 0 2 207 86 0 0 0 0 0 0
EL 408 CR 0 2 208 87 0 0 0 0 0 0
EL 409 CR 0 2 209 88 0 0 0 0 0 0
EL 410 CR 0 2 210 89 0 0 0 0 0 0
EL 411 CR 0 2 211 90 0 0 0 0 0 0
EL 412 CR 0 2 212 91 0 0 0 0 0 0
EL 413 CR 0 2 213 92 0 0 0 0 0 0
EL 414 CR 0 2 214 93 0 0 0 0 0 0
EL 415 CR 0 2 215 94 0 0 0 0 0 0
EL 416 CR 0 2 216 95 0 0 0 0 0 0
EL 417 CR 0 2 217 96 0 0 0 0 0 0
EL 418 CR 0 2 218 97 0 0 0 0 0 0
EL 419 CR 0 2 219 98 0 0 0 0 0 0
EL 420 CR 0 2 220 99 0 0 0 0 0 0
EL 421 CR 0 2 221 100 0 0 0 0 0 0
EL 422 CR 0 2 222 101 0 0 0 0 0 0
EL 423 CR 0 2 223 102 0 0 0 0 0 0
EL 424 CR 0 2 224 103 0 0 0 0 0 0
EL 425 CR 0 2 225 104 0 0 0 0 0 0
EL 426 CR 0 2 226 105 0 0 0 0 0 0
EL 427 CR 0 2 227 106 0 0 0 0 0 0
EL 428 CR 0 2 228 107 0 0 0 0 0 0
EL 429 CR 0 2 229 108 0 0 0 0 0 0
EL 430 CR 0 2 230 109 0 0 0 0 0 0
EL 431 CR 0 2 231 110 0 0 0 0 0 0
EL 432 CR 0 2 232 111 0 0 0 0 0 0
EL 433 CR 0 2 233 112 0 0 0 0 0 0
EL 434 CR 0 2 234 113 0 0 0 0 0 0
EL 435 CR 0 2 235 114 0 0 0 0 0 0
EL 436 CR 0 2 236 115 0 0 0 0 0 0
EL 437 CR 0 2 237 116 0 0 0 0 0 0
EL 438 CR 0 2 238 117 0 0 0 0 0 0
EL 439 CR 0 2 239 118 0 0 0 0 0 0
EL 440 CR 0 2 240 119 0 0 0 0 0 0
EL 441 CR 0 2 241 120 0 0 0 0 0 0
EL 442 CR 0 2 242 121 0 0 0 0 0 0

C* Constrainment of nodes
DCR 6 UX 0 6 1
DCR 2 UX 0 2 1
DND 256 UY 0 256 1

```
DND 1011 AL 0 1011 1
DND 144 UY 0 144 1
DND 23 UY 0 23 1
DSF 1 UZ 0 1 1
DSF 2 UZ 0 2 1

C* Loading times and load-time curve definition
TIMES 0 10 1
CURDEF TIME 1 1 0 0 10 1E+08
ACTSET TC 1

C* Application of force
FND 121 FY -1 121 1
FND 242 FY -1 242 1
DND 144 RZ 0 144 1
```

VITA

Nikhilesh Chawla was born in Rio de Janeiro, Brazil, on January 8, 1972. He attended elementary school at Colegio Andrews in Rio de Janeiro. In 1984, he and his family moved to Urbana-Champaign, Illinois, where he attended Urbana Junior High School for one year. Another move followed to Socorro, NM in 1985. He graduated from Socorro High School in May 1989 and attended New Mexico Tech, also in Socorro, from 1989 to May 1993, where he received his Bachelor's degree in Materials Engineering. While attending New Mexico Tech he had brief summer jobs at the Center for Explosives Technology Research at New Mexico Tech, University of Maryland-College Park, Oak Ridge National Laboratory, and Argonne National Laboratory. In the Fall of 1993 he enrolled at the University of Tennessee-Knoxville, while conducting his research at the High Temperature Materials Laboratory at Oak Ridge National Laboratory, and received a Master of Science degree in Metallurgical Engineering in December 1994.